REVIEW

Check for updates

Recent developments in supercapacitor electrode materials: design, performance, and future perspectives

Amina Afreen,†[a] Mohamed Bechir Ben Hamida,[b] Muhammad Nasir Hussain, ![ID] †*[a] Muhammad Javaid,[a] Nashmi Alrasheedi,[c] Javed Iqbal, ![ID] [d] Ali Haider ![ID] [a] and Syed Mujtaba Shah*[a]

Supercapacitors have gained massive attention as next-generation energy storage devices because of their high power density, long cycle life, fast charge–discharge rate, and good environmental sustainability. Their role in energy storage and harvesting is crucial, specifically in advanced portable electronic devices. This review presents a comprehensive overview of the recent developments in supercapacitor research by covering the design of electrode materials and the advancements in developing novel materials. The recent developments in the fields of electric double-layer capacitors, hybrid supercapacitors, and pseudocapacitors, with a particular focus on their electrode materials, are also discussed. The major focus is on two-dimensional (2D) materials including carbon aerogels, carbon foams, carbide-derived carbons, graphenes, CNTs, activated carbons, TMDs, h-BN, MXenes, and carbon nitrides, which exhibit excellent electrochemical properties for supercapacitor applications. Transition metal oxides such as RuO_2, ZnO, NiO, Co_3O_4, MnO_2, Fe_2O_3/Fe_3O_4 and V_2O_5 are also enticing electrode materials for supercapacitors owing to their excellent redox behavior and high energy density. Finally, the challenges and future perspectives are discussed, along with providing potential strategies for electrode performance enhancements.

1. Introduction

Energy storage devices such as supercapacitors and batteries have numerous limitations in fulfilling the growing energy demands. Batteries deliver high energy density, while capacitors are ideal for high power output.[1] However, both devices are not compatible for applications requiring high energy and power density. This limitation has sparked the search for new energy storage systems, including electrochemical capacitors, supercapacitors, and ultracapacitors. The primary reason behind the fabrication of such devices is to find an alternative to fossil fuels to meet the energy demands. However, batteries excel in delivering high energy densities and capacitors are well-suited for high power output scenarios. Supercapacitors

have demonstrated significant potential across various industrial and automotive applications due to their high specific capacitance, rapid charge–discharge capability, and promising energy storage performance. Recent advancements in supercapacitors have enhanced their energy density values, making them a promising substitute for batteries.[2–6] The use of hybrid materials as electrodes enables both high energy storage and high power output.

The performance of sustainable energy storage systems including batteries and electrochemical capacitors is governed by the physical and chemical properties of their electrodes. In supercapacitors, capacitance arises from electric double layers formed at the electrode–electrolyte interface and is highly influenced by the available surface area. Capacitance is a result of reversible oxidation and reduction reactions in the electrochemical double layer capacitor (EDLC). The working principle of EDLCs is based on electrochemical processes, and they are made up of two electrodes submerged in an electrolyte and divided by a permeable membrane that acts as a separator. The electrodes of EDLCs are made up of activated carbon materials having high surface area and the electrolyte will be either aqueous or organic in nature. Capacitance is directly related to the dielectric constant of the material and area of the

[a] Department of Chemistry, Quaid-i-Azam University, Islamabad, 45320, Pakistan.
 E-mail: nasirhussain@chem.qau.edu.pk, smschem69@yahoo.com

[b] Deanship of Scientific Research, Imam Mohammad Ibn Saud Islamic University (IMSIU), Riyadh, Saudi Arabia

[c] College of Engineering, Imam Mohammad Ibn Saud Islamic University (IMSIU), Riyadh, Saudi Arabia

[d] Department of Botany, Bacha Khan University, Charsadda, Khyber Pakhtunkhwa, 24420, Pakistan

† AF and MNH contributed equally to this work.

electrodes while inversely related to the distance between electrodes. Increasing the surface area and dielectric constant and placing the electrodes closer will lead to an increase in capacitance. The electrochemical performance of the material can be further enhanced by improving the capacitor design. For example, reducing the material size to the sub-nanometer scale, where quantum confinement effects become significant. Another way of improving the electrochemical performance is the doping of metal ions, *e.g.*, Mn, Fe, Cr, and Co into electrode materials, which may enhance their electrical conductivity, resulting in an increase in capacitance.

A supercapacitor can exhibit an improved electrochemical performance if it consists of symmetric electrodes or operates on a faradaic process. A faradaic process involves the charge transfer at the electrode/electrolyte interface following Faraday's law, whereas in the non-faradaic process no charge transfer occurs. The adsorption and desorption occurring at the electrode/electrolyte interface and the solvent dipole reorientation are non-faradaic processes. EDLCs have numerous advantages and disadvantages, and we will discuss the key elements here. For example, their non-faradaic electrical mechanisms enable highly reversible charging and discharging cycles, which, in turn, increases their rates, ensuring stable cycling ability up to 10^6 cycles as well as minimal degradation. The primary disadvantage of EDLCs is restricted to the choice of electrode materials. The electrode materials with high conductivity are more effective in the EDLC operation. This problem can be addressed by the invention of solid ionic conductive electrolytes.[7–10] EDLC's can be classified into three types depending on the presence of carbon content within the device. Additionally, the characteristics of morphology, hybridization and structural defects are useful for differentiating between carbon-containing materials. Furthermore, pseudocapacitors undergo redox reactions which involve charge transfer between the electrolyte and the electrode. These faradaic reactions occur at the interface between the electrode and the electrolyte where charge storage also occurs. The transfer of ions and electrons between the electrolyte and the electrode is necessary for this process to occur.[11] During charging, the oxidation state of the electrode material changes due to the absorption of electrolyte ions onto the electrode surface. In this process, the charge storage arises from the incorporation of ions into the lattice structure of materials or generation of surface-bonded species. During discharging, the reversed redox process and conversion of electrode materials into its initial stage occur and the stored charge is released.

Furthermore, in comparison to activated carbon materials, the oxide materials have high specific capacitance, gravimetric capacitance, and higher density. It also has significant volumetric capacitance that is beneficial for device fabrication. A variety of techniques including electrospinning, redox and intercalation are employed for their production. Pseudocapacitors that operate on a faradaic process have high energy density values compared to EDLCs. These types of capacitors mostly use conductive polymers, metal oxides, and metal-doped carbon as electrode materials. However, redox reactions occurring in pseudocapacitors lead to their low power density and shorter life cycle.[12]

Another important type of supercapacitor is a hybrid which is made up of non-polarizable electrodes (made of metal or conducting polymers) and polarizable electrodes (made of carbon). The hybrid supercapacitor stores charge utilizing both non-faradaic processes and faradaic processes.[13] This approach exploits both battery-type and supercapacitor-type electrodes[14,15] for high energy storage, resulting in improved cycling stability and reduced price as compared to EDLCs. It is classified into asymmetric, composite, and battery-type supercapacitors. Asymmetric hybrid supercapacitors consist of two different electrodes, which makes this type of supercapacitor noticeable among others. In an asymmetric device, one electrode is made of capacitive material and one of faradaic to meet the energy and power density requirements.[16,17] The anode is a metal or metal oxide, whereas the negative electrode is made of compounds derived from carbon. Metal electrodes exhibit a large intrinsic volumetric capacity, which results in enhanced energy densities.[18,19] In comparison to symmetric electrodes, these capacitors possess the ability to show larger cycling stability with higher energy density, as observed in the case of carbon and MnO_2 on an electrode made up of a nickel-foam.[20,21]

All capacitors face the challenge of self-discharge; this problem can be overcome by introducing a rocking-chair mechanism in an asymmetric supercapacitor. This is the point where zero current is guaranteed at maximum potential.[18] It is observed that electrolytes cause a decrease in ionic conductivity and increase in resistance due to the depletion of ions over time. This problem can be alleviated by designing and using novel electrolytes. Another problem that needs attention is the enhancement of the supercapacitor's working potential window. Better voltage range and a rocking-chair mechanism can be obtained by using activated carbons or carbon-derived samples with efficient P doping as negative electrodes. The optimization of carbon microporous layer plays a key role in facile ion transport and enhanced capacitance.[18] Furthermore, the composite hybrid supercapacitors aim to achieve a combination of enhanced cycling stability, specific capacitance, and high conductivity. Carbon-based materials used in EDLCs exhibit outstanding mechanical strength, low resistance, and a large surface area. However, metal oxides, except RuO_2, possess poor conductivity and undergo Joule heating with small surface area and poor structural stability. Despite these shortcomings, they can store charge and energy efficiently. Composite supercapacitors intend to deliver desired characteristics such as high specific capacitance, high conductivity, and cycling stability by integrating the properties of carbon and metal oxides.[22] The combined effect of carbon and metal oxide facilitates the efficient charge transport and storage with carbon providing conducting channels and metal oxides undergoing redox reactions to store charge, leading to enhanced energy density with greater specific capacitance. The structure of the carbon used (microporous, mesoporous, or microporous) has a significant impact on the conductivity of carbon-based

materials.[23] The size of the pores plays a vital role in determining the adsorption of ions onto the surface of the electrode, indicating the properties of EDLCs and their ability to charge/discharge. Despite the numerous advantages of composites, they have shortcomings as observed in the case of layered vanadium oxide on carbon nanofibers, where increasing thickness (18 nm) caused a decrease in efficiency.[24] This is the outcome of the disparity between the conductivity of the composite and redox sites.

Another challenge is the growth of nanowhiskers onto carbon nanosheets, which hinders the diffusion of ions.[25] This highlights the relationship between the limitations and the advantages of composites that are impacted by the components and their coordination with the electrolyte. Another important category is rechargeable hybrid battery-type supercapacitors, where efforts are focused on improving Ragone plot performance by achieving a better balance between energy and power density. Ragone plots show the features of high specific capacitance, energy, and power density that need to be elevated yet, in comparison to a present class of supercapacitors. The storage capacity of battery type can be improved by surface modifications, developing new synthetic strategies for the synthesis of nanocomposite materials and micro-structures. The development of electroactive nanoparticles is essential to promote quicker reactions with electrolytes.

The metal oxide-based nanocomposites face various challenges, for instance, the coating of a carbon layer on $LiMnPO_4$ that has more promising potential than its Fe equivalent. An innovative solution was found to deal with this issue where a multi-layered structure was designed by the coating of carbon layered over Fe and Mn. The study revealed that this approach was highly effective at higher rates and without any interaction between Mn-based metal oxides and electrolytes.[26] Electroactive species are highly regarded for their outstanding ability to speed up the electrode reactions. Their impact can be enhanced by generating granules with varied proportions on the surface of the electrode, causing the electrolyte–electrode interface to experience a fractal-granularity effect. This remarkable approach enhances the surface area and increases the capacitor's overall energy output. A major improvement in supercapacitor technology was made through using the double layer concept where it leads to the formation of Helmholtz double layer at the interface between the carbon electrode and the electrolyte, facilitating charge storage through a physical process governed by the contact of polar ions. This results in an outstanding increase in energy density over several orders of magnitude.

The primary aim of this review is to provide a systematic and up-to-date overview of the recent advancements in supercapacitor electrode materials, with a particular emphasis on two-dimensional (2D) materials and transition metal oxides (TMOs). The review critically analyses the structure–property–performance relationships that govern EDLCs, pseudocapacitors, and hybrid supercapacitors. Special attention is devoted to emerging materials including carbon aerogels, graphenes, carbon nanotubes (CNTs), MXenes, transition metal dichalcogenides (TMDs), carbon nitrides, and metal oxides such as RuO_2, MnO_2, Co_3O_4, NiO, iron oxide, and V_2O_5, and a detailed discussion of their electrochemical mechanisms and key performance metrics are presented. Furthermore, the review aims to bridge the gap between material design strategies and practical device-level performance by highlighting critical challenges such as electrical conductivity, structural stability, and scalability. Finally, we outline the future research directions and rational material engineering strategies to enhance the energy density while maintaining high power density and long-term cycling stability. The graphical representation of electrode materials is presented in Fig. 1(a). Wang *et al.*[27] has demonstrated the number of related studies published in the last few years, as shown in Fig. 1(b).
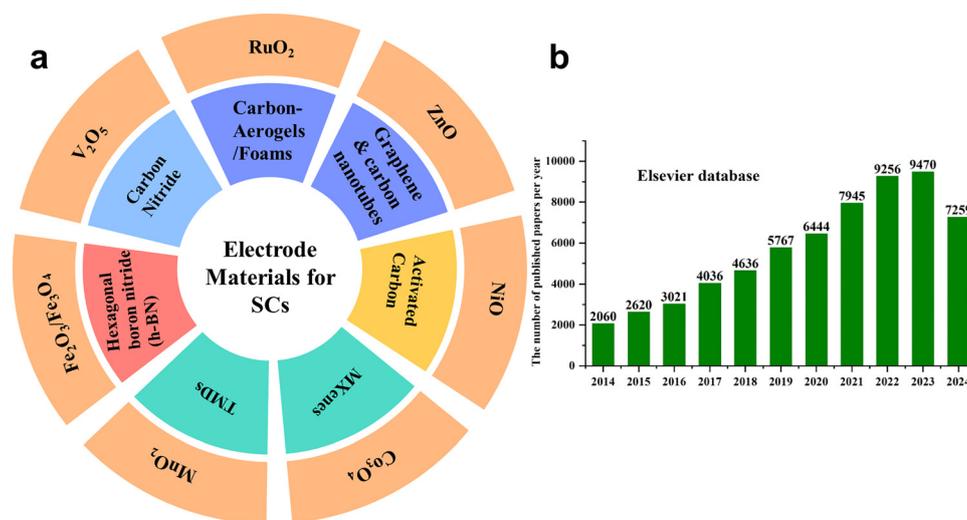

Fig. 1 (a) Schematic of the type of electrode materials. (b) Number of published papers on SCs; reproduced from ref. 27 with permission from Elsevier, Copyright 2024.

2. Properties of the electrode materials for supercapacitors

The performance of supercapacitors is fundamentally governed by the properties of the electrode materials, which dictate charge storage capability, energy and power density, and long-term cycling stability. The essential properties of electrode materials include specific capacitance, energy density, power density, electrical conductivity, surface area, pore structure, and chemical stability, all of which directly influence the device performance. An in-depth understanding of these properties and tailoring them are critical for designing high-performance supercapacitors. Electrochemical energy storage in supercapacitors occurs primarily through two mechanisms: EDLC and pseudocapacitance.[28] EDLC arises from the electrostatic accumulation of ions at the electrode–electrolyte interface, and is typically observed in carbon-based 2D materials such as graphenes, CNTs, carbon aerogels, carbon foams, carbide-derived carbons, activated carbons, h-BN, MXenes, and carbon nitrides. The high surface area of these materials provides abundant sites for ion adsorption, resulting in high specific capacitance values, typically depending on surface functionalization, porosity, and electrode preparation methods.[29,30]

Furthermore, TMOs (*e.g.*, RuO_2, ZnO, NiO, Co_3O_4, MnO_2, Fe_2O_3/Fe_3O_4 and V_2O_5) exhibit pseudocapacitance arising from fast and reversible redox reactions at or near the electrode surface.[31–35] These materials can achieve higher energy density than purely carbon-based EDLCs because they store charge not only through physical adsorption but also *via* faradaic processes. For example, MnO_2 exhibits multiple oxidation states, enabling multivalent redox transitions and thus enhancing the overall capacitance. RuO_2 is considered the benchmark due to its excellent pseudocapacitive performance, though its high-cost limits large-scale applications. Electrical conductivity is a critical property that governs the rate of charge–discharge and the efficiency of electron transport within the electrode. Carbon-based 2D materials generally exhibit excellent conductivity due to their sp^2 hybridized carbon networks, which allow electrons to move freely. MXenes, with their metallic conductivity, also provide outstanding electron transport, making them ideal for high-rate supercapacitors.[36] However, TMOs often suffer from lower conductivity, which can limit their rate performance. Various strategies such as compositing with conductive carbon materials or creating nanostructured morphologies have been widely employed to overcome these limitations and enhance the electrochemical performance. Moreover, high surface area and appropriate pore size distribution are crucial for maximizing ion accessibility and ensuring fast ion diffusion within the electrode material.[37] In EDLC supercapacitors, the specific surface area directly correlates with the achievable capacitance, as it determines the number of active sites available for ion adsorption. Materials like graphenes and activated carbons often exhibit surface areas exceeding 1000 m^2 g^{-1}, whereas MXenes and TMDs can be engineered to expose more active sites *via* exfoliation or defect creation. The pore structure, comprising micropores (<2 nm),

mesopores (2–50 nm), and macropores (>50 nm), plays a vital role in facilitating ion transport and reducing diffusion resistance. Micropores contribute significantly to capacitance due to their high surface area, while mesopores and macropores improve electrolyte accessibility and rate capability. Hierarchical pore structures, combining micro/meso and macropores, are particularly effective for balancing high capacitance with fast charge–discharge characteristics.[38] Additionally, the morphology of electrode materials has a strong influence on electrochemical behavior. The nanostructured materials including nanoparticles, nanosheets, nanorods, and hollow structures provide small ion diffusion paths and a large surface-to-volume ratio, enhancing both capacitance and rate capability. For instance, nanomaterials synthesized using templates or ultrasonic-assisted methods often exhibit porous or hollow structures that improve electrolyte penetration and increase the number of electroactive sites. Similarly, MXenes and graphene sheets can be stacked or functionalized to create interconnected networks, which facilitate rapid electron and ion transport.[39]

Another parameter is the chemical composition, and the surface functionalities of electrode materials significantly affect their electrochemical performance. Oxygen-containing groups (–OH, and –COOH) on carbon-based materials enhance wettability and facilitate pseudocapacitive reactions. In MXenes, surface terminations such as –OH, –F, and –O play a similar role, improving ion adsorption and interfacial charge transfer.[40] For TMOs, mixed oxidation states allow multiple redox reactions, directly influencing specific capacitance and energy density. The control of stoichiometry can further optimize the electrochemical properties. Moreover, a high-performance supercapacitor requires long-term cycling stability and excellent rate capability.[41] The carbon-based materials, due to their chemical stability and mechanical robustness, often show minimal degradation over thousands of charge–discharge cycles, while TMOs offering higher pseudocapacitance may suffer from structural changes or dissolution during prolonged cycling. Many approaches such as compositing with flexible carbon matrices, forming hybrid nanostructures, or using 2D layered materials like MXenes and TMDs have been shown to enhance the cycle life while maintaining high capacitance. Typically, the interaction between electrode materials and electrolytes also impacts supercapacitor properties. A wide operating voltage window is desirable for higher energy density, and this is influenced by the chemical stability of the electrode in the chosen electrolyte. For example, MnO_2 electrodes perform well in aqueous electrolytes but may require surface modification or hybridization for stable operation in organic or ionic liquid electrolytes. MXenes and COFs can be tuned chemically to optimize their electrolyte compatibility and interfacial charge transfer kinetics.[42–44]

In summary, the properties of supercapacitor electrode materials are interconnected, and collectively determine the device performance. The 2D materials offer high surface area, excellent conductivity, and tunable chemistry, making them suitable for EDLCs and hybrid devices. TMOs contribute high

pseudocapacitance through redox activity, but their conductivity and stability often need enhancement. The optimizing morphology, porosity, surface chemistry, and composite formation is essential to achieve high specific capacitance, energy density, power density, and long-term stability. Understanding these properties provides a foundation for designing next-generation electrode materials for advanced supercapacitors.

3. Choice of high-performance electrode materials for supercapacitors

Nanostructured materials have gained substantial interest for supercapacitor applications as they exhibit improved capacitance behaviour compared to their bulk counterparts. These materials possess a higher surface area, which leads to the availability of a high number of active sites for electrochemical reactions. The high number of active sites contributes to the fast chemical kinetics and smaller ionic diffusion path length. The configuration of supercapacitors includes electrodes, electrolytes, separators, and current collectors, and each component impacts the overall efficiency of the device. The selection of suitable electrode material is crucial to ensure the optimal performance of supercapacitors. The electrode material should possess a great surface area, excellent stability, great electrical conductivity, and remarkable mechanical characteristics. These materials should be economically feasible, resistant to corrosion, and highly safe. The pore size distribution is also highly influencing the performance of the device. The materials having pore sizes under 2 nm can deliver greater energy density with higher specific capacitance, while the materials of the electrode with large pore size offered low energy density and high equivalent series resistance (ESR). Therefore, the judicious choice of the electrode materials is paramount, which can deliver high storage performance. This section comprehensively explains the potential of various 2D materials for supercapacitor applications.

3.1. Carbon aerogels, carbon foams and carbide-derived carbons

Carbon aerogels are considered to be the world's lightest material with high surface area and a density of 200 μg cm^{-3}.[45] There are ongoing efforts to enhance the compressibility and adsorption level to enhance the excellent thermal, electrical and mechanical properties of the carbon materials.[46] Their adsorption capacity of liquid oil is 900 times their mass, which makes it a promising alternative in the cleaning of hazardous solutions and oil spillage.[45] Additionally, adding a polymer binder can strengthen the delicate structure of carbon aerogels, which significantly decreases their conductivity. Amorphous carbon aerogels were produced using conventional methods including sol–gel procedure and freeze-drying carbon solution method. Carbon aerogels, consisting of interconnected 3D carbon nanotube networks, exhibit high Young's modulus and excellent elasticity and compressibility.[47] The van der Waals forces present between adjacent CNTs hold their

lightweight structure and endow enhanced mechanical and transport properties. This makes them appealing candidates for energy storage devices and sensors, which can respond to small fluctuations in pressure.[48] Frequent cyclic compressions may create cracks in carbon aerogels, resulting in their reduced flexibility. The pore size concentration can be controlled by employing various synthetic methods. However, including metal precursors can lead to changes in pH, pyrolysis, and activation, which can challenge the consistent pore structure.[49] Choi et al.[50] used porous carbon aerogels with a coral-like hierarchical structure, which were synthesized via spinodal decomposition, and they exhibit high mechanical strength (1.67 GPa), electrical conductivity (55 S m^{-1}), and specific capacitance (339.2 F g^{-1} at 0.5 A g^{-1}). A symmetric supercapacitor achieved 22.9 Wh kg^{-1} at 1000 W kg^{-1} with excellent cycling stability ($\sim$98% retention over 100 000 cycles). Haj et al.[51] have developed a rational design to prepare carbon aerogels for supercapacitors. They have investigated the surface wettability through electro-assisted (EA) adaptation and demonstrated the impact on the electrolyte accessible surface area portion. The EA is a technique in which the electrode is wetted for multiple cyclic treatments to obtain constant and adaptive wettability in the absence of applied potential. The main aim is to modify the electrode material properties without any external electric field, as shown in Fig. 2(a). Therefore, the supercapacitor performance and reliability are enhanced. The fabricated device based on carbon aerogels dispersed in calcium nitrate showed a capacity retention of 120.29% and 134.42% when tested for 5000 and 10 000 cycles, respectively, at 10 A g^{-1}, as presented in Fig. 2(b). A linear relationship between contact angle and specific capacitance suggests that maximum capacitance is achieved under superhydrophilic wetting conditions, as displayed in Fig. 2(c). The electrode's improved wettability results in the high performance of the electrode with excellent storage cyclic voltammetry (CV) profiles, as seen in Fig. 2(d). The device showed improved specific capacitances of 128 F g^{-1}, 149.8 F g^{-1}, and 172.8 F g^{-1} under dry, wet and EA wet conditions at 10 A g^{-1}, respectively. The Nyquist plots for EA wet, wet and dry electrodes with the fitted model circuit are presented in Fig. 2(e).

3.2. Graphenes and carbon nanotubes

Recently, graphene has been considered as an appealing material with excellent storage properties compared to other carbon-derived materials.[52,53] The structure of graphene is like honeycomb with sp^2 hybridization in a hexagonal lattice. It has a surface area of 2630 m^2 g^{-1}, which is greater than that of the single-walled carbon nanotubes (SWCNTs). The large surface area of EDLCs makes them promising materials.[54–57] Graphene has unique properties as an electrode material such as high electrical conductivity (10^6 S cm^{-1}), long cycle life, high Young's modulus ($\sim$1 TPa), thermal conductivity (5000 W m^{-1} K^{-1}), carrier mobility (2 $\times$ 10^5 cm^2 V^{-1} s^{-1}), optical transmittance (97.7%), and resistance against corrosion in aqueous electrolytes. These combined exceptional properties make it an enticing electrode material in supercapacitors.[55,58] The modified
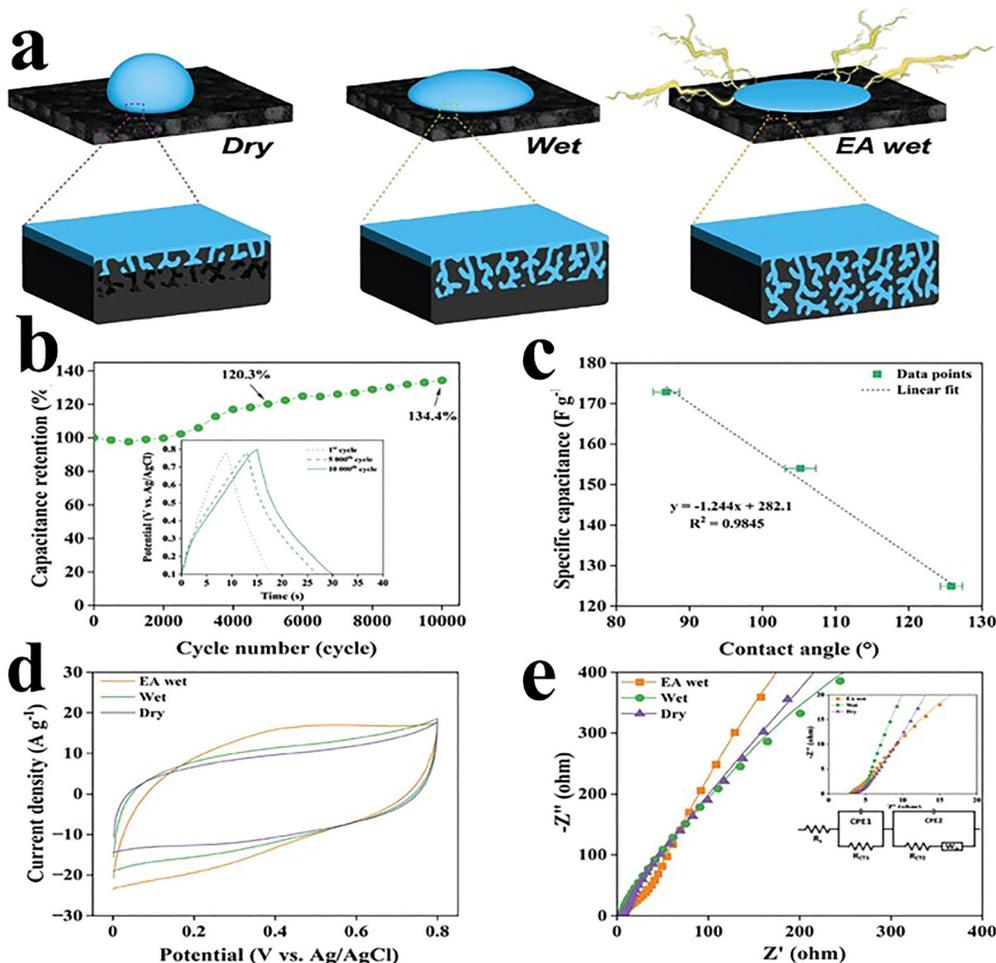
Fig. 2 (a) Schematic of the fabricated electrode under different conditions such as dry, wet, and EA. (b) Cycling stability at 1 A g^{-1}. (c) Linear fit against the contact angle. (d) CV profiles under all applied conditions at 100 mV s^{-1}. (e) Nyquist plots. Reproduced from ref. 51 with permission from Wiley-VCH, Copyright 2024.

Hummers' method is employed for the synthesis of graphene using graphite as a precursor. The exceptional carrier mobility of the graphene support for the fast charging–discharging plays an important role in enhancing the performance of supercapacitors. A major challenge is the aggregation and restacking of graphene sheets caused by π–π interactions and van der Waals forces.[59,60] As a result, the surface area of the graphene plate was reduced and the diffusion of electrolyte ions was disrupted, which compromise the supercapacitor's performance.[60,61] The high surface area facilitates efficient mass transport during the electrochemical investigation, while the loss of connectivity in graphene sheets affects the electrical conductivity negatively. Heteroatom doping into graphene can be applied to overcome this issue. A combined EDLC and pseudocapacitor behaviour was obtained by making the composites of graphene with polypyrrole (PPy) materials. A graphene-PPy composite demonstrates a specific capacitance of 400 F g^{-1} at 0.3 A g^{-1} that is higher than the already fabricated composites. A graphene-based film made of shape-memory polyurethane (SMPU) was synthesized as another promising electrode material. The fabricated

graphene/SMPU-based electrode exhibited a specific capacitance of 218 F g^{-1} at 0.75 A g^{-1}.[62] Akhter et al. have synthesized nitrogen and sulfur co-doped graphene in a flexible 3D configuration using one-pot thermal treatment. The material showed an excellent specific capacitance of 305 F g^{-1}. The binder-free and lightweight N/S co-doped graphene architecture makes it a potential material for energy storage applications and electronics. A 3D graphene network-based composite with MnCo$_2$O$_4$ was prepared by a hydrothermal method. The composite has high specific capacitance with exceptional cycle life. The integration of MnCo$_2$O$_4$ with 3D graphene endows a capacity retention of 97.4% over 5000 cycles. The high stability of the material makes an effective material for energy storage systems.[63] Rajeevan et al.[64] have combined silane-functionalized rGO with 20 wt% acid-treated CNTs to form a binary electrode exhibiting high pseudocapacitance of 82.6% and a specific capacitance of 225.8 F g^{-1}. The aqueous symmetric supercapacitor achieved 31.4 Wh kg^{-1} energy density, 1714 W kg^{-1} power density, and 95% capacitance retention over 2000 cycles. Athira et al. have designed a polyaniline (PANI)–rGO composite to study the effect of anionic surfactants

of sodium lauryl sulfate (SLS). The PANI–rGO composite exhibits a specific capacitance of 531 F g^{-1} at a current density of 0.2 A g^{-1} in an H$_2$SO$_4$ electrolyte. Moreover, the composite has retained 98% coulombic efficiency after 5000 cycles. The faradaic and EDLC behaviours have been observed because of the synergistic effect of PANI, SLS and rGO, making it a promising candidate for supercapacitors.[65] PPy is another material that has a larger particle size with low porosity than that of the PANI/graphene composite. Therefore, PPy-based materials have less stability than the other composites. The poor electrical conductivity, low cycling stability, and storage capacity are the limitations of metal oxides and other conducting polymers. Therefore, the combination of these materials with carbon-based materials enhanced the electrochemical performance compared to the individual materials. Graphene can easily be transformed into different dimensions such as 0D, 1D, 2D, and 3D with high surface area.[66] It has a combination of excellent properties, which makes it an appealing material for supercapacitors. The combination of graphene with other elements and functional groups can form a variety of nanocomposites including graphene hydroxides, graphene-metal oxide composites, and graphene conductive polymers. The pristine and additive materials collectively introduce a synergistic effect, which helps to overcome the limitation of lower ion transport and inhibit the accumulation of graphene nanosheets.[58,67] An increased surface area, high power density, electrical conductivity, and controllable pore size are offered by the composite's materials. These composites possess unique properties with a few drawbacks such as low capacitance or slow ion diffusion.[68] The framework of CNTs has been composed of graphene sheets which are rolled up with each other. The CNTs show conduction through ballistic transport and charge carriers have large

mean free path and no scattering, which eliminates the Joule heating phenomenon. The phenomenon of Joule heating is a main issue in conductors while CNTs have an advantage regarding this aspect. There are two types of CNTs, such as SWNTs and multi-walled nanotubes (MWNTs). SWNTs exhibit a higher surface area, flexibility, and a size of about 5 nm. CNTs get entangled to form bundles even with high sought-after properties. MWNTs have a high number of defects compared to SWNTs, which may deviate from the intrinsic properties leading to their high resistance. They are utilized as the perfect filler material since they are larger than SWNTs, with an average length of 20 nm and a higher capacity. The composite forms of CNTs can be chemically altered and show increased strengths. The chemical vapour deposition, compression moulding, and solution processing methods have been employed to produce the modified versions of CNTs.[69] Zheng *et al.*[70] prepared a three-dimensional porous PPy/phytic acid (PA)/graphene composite aerogel (PPGA) *via* a one-step hydrothermal reduction method, where PA served as both the dopant and the cross-linker. The electrochemical performance of asymmetric flexible supercapacitors (ASCs) assembled using PPGA@AC electrodes was systematically evaluated. As shown in Fig. 3(a), the CV curves recorded at 10 mV s^{-1} under different voltage windows retain distinct redox peaks that slightly intensify with the increase in voltage, demonstrating a strong pseudocapacitive behavior. The CV curves at different scan rates clearly display redox peaks, and the device delivers a high specific capacitance of 220 F g^{-1} at 40 mV s^{-1}, as shown in Fig. 3(b). The galvanostatic charge–discharge (GCD) profiles at different current densities show stable and nearly ideal charge–discharge characteristics up to 1.7 V, indicating suitability for rapid charge–discharge applications, as displayed in Fig. 3(c).
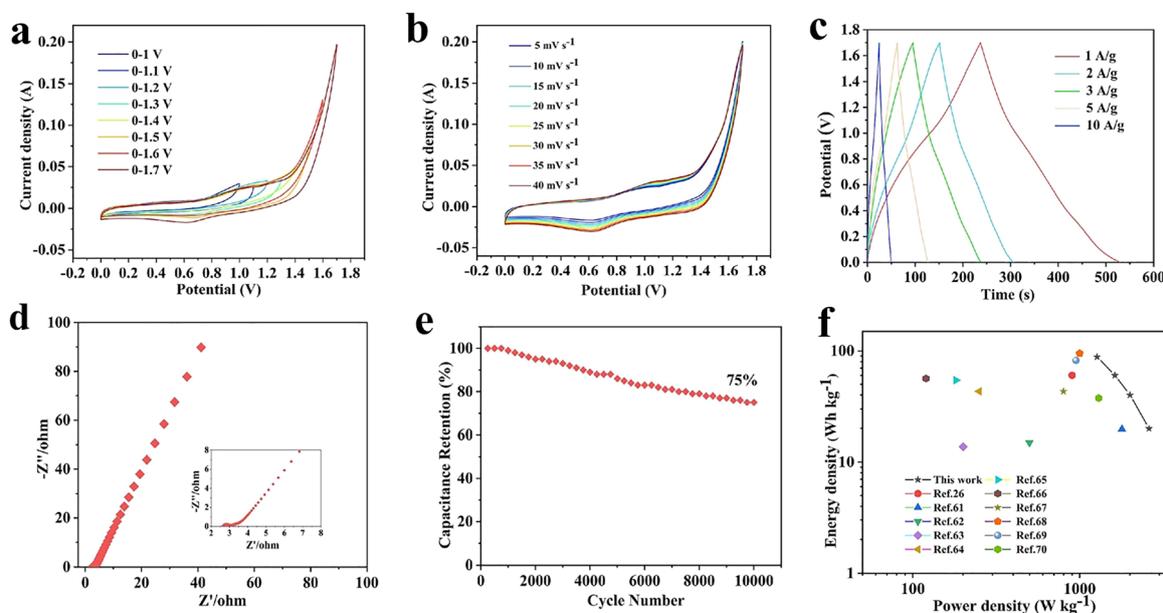

Fig. 3 (a) CV curves of the PPGA@AC device in different potential intervals. (b) CV curves of the PPGA@AC device at different scan rates. (c) GCD curves of the PPGA@AC device at different current densities. (d) Nyquist plots of the PPGA@AC device. (e) Cycling stability of the PPGA@AC device. (f) Ragone plots of the PPGA@AC device. Reproduced from ref. 70 with permission from Elsevier, Copyright 2025.

The Nyquist plot reveals a low equivalent series resistance of 2.5 Ω, confirming efficient charge transfer and favourable electrolyte conductivity, as shown in Fig. 3(d). Furthermore, the ASC device retains 75% of its capacitance after 10 000 charge–discharge cycles, demonstrating good long-term stability despite slight attenuation, as shown in Fig. 3(e). The device achieves a high energy density of 88.2 Wh kg^{-1} at a power density of 1271.52 W kg^{-1}, highlighting its excellent electrochemical performance, as shown in Fig. 3(f).

3.3. Activated carbons

The excellent electrochemical performance of activated carbon-based EDLC devices is due to the high surface area and oxidizing nature. The oxidation of carbon materials is accompanied by a spectral overlap of D and G bands of the Raman spectrum, implying a change in phonon density of states which leads to a red shift in the Raman line. Pore size and defect engineering like dangling carbon bonds and C–C bond structures can help to explain this behavior. Compared to graphene, the activated carbon is a low-cost material. Moreover, activated carbons offer precise tuning of pore sizes spanning a wide range from less than 5 nm to above 50 nm. The excellent electrochemical performance of the capacitor depends on the interaction between the ion size and the pore size of electrolytes. However, a mismatch of the ion and pore sizes of an electrolyte can decrease the capacitance, which is a major drawback of activated carbon (AC).[71] Additionally, the defect structure of the electrode determines the device performance.[72–75] Therefore, to increase the charge storage capacity of the capacitor, a suitable match of the ion and pore sizes of electrolytes is essential.[13,76] Kattainen *et al.*[77] prepared solvothermal-treated AC electrodes, which showed enhanced surface area (2471 m^2 g^{-1}) and pore volume (1.83 cm^3 g^{-1}),

leading to specific capacitance increases of $\sim$140% (28 F g^{-1}, aqueous) and $\sim$80% (33 F g^{-1}, deep eutectic solvent). The electrodes also exhibited excellent cycling stability ($\sim$95% retention over 10 000 cycles, aqueous) and reduced leakage currents. Jain *et al.*[78] have used European deciduous trees to fabricate cost-effective and sustainable AC base electrode materials. For the synthesis of AC, a mixture of European deciduous trees including birch, *Carpinus betulus*, and Fagaceae was carbonized in air at a high temperature of 500–700 °C for 10 min. Then, the mixture was activated using nitric and sulfuric acid in a ratio of 1 : 3. The synthetic procedure is depicted as a schematic in Fig. 4(a). The cavitation method causes pores in the sample (CKP1) as compared to the non-cavitated sample, which was confirmed by the morphological studies, as displayed in Fig. 4(b) and (c). This porous structure supports the electrode–electrolyte interaction, improving the specific surface area (SSA) and providing large active sites for the ion interface. Therefore, the storage performance has been enhanced. The CKP1 sample has more pores with an SSA of 614 m^2 g^{-1}. The material showed an enhanced specific capacitance of 74 F g^{-1} in 1 M H$_2$SO$_4$ at 0.25 A g^{-1}. The CV and GCD profiles showed very good stable shapes at higher scan rates and current densities with excellent cycling stability up to 10 000 cycles, as presented in Fig. 4(d)–(f).

3.4. MXenes

MXenes have gained interest in storage technologies due to their excellent conductivity, hardness, elevated melting point, high stability, high surface area, and hydrophilic nature. MXenes are based on transition metal (TM) carbides and nitrides with the formula of M$_{n+1}$X$_n$T$_x$, where M represents a TM (V, Cr, Mo, Ti, Nb or W), X denotes carbon or nitrogen, and T denotes surface termination groups such as –OH, –F or –O.[79,80]
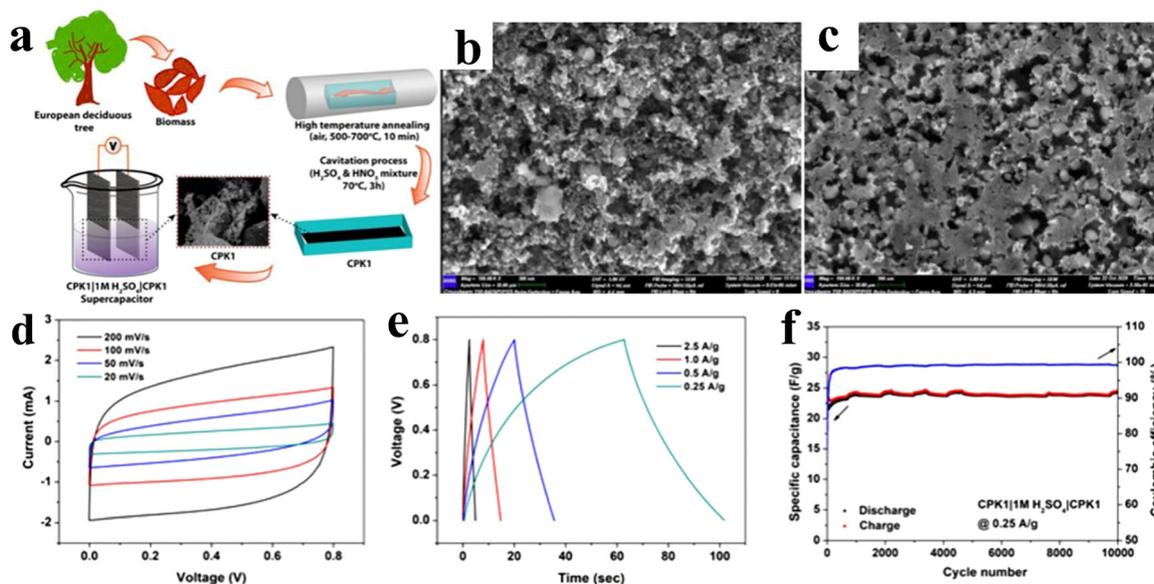

Fig. 4 (a) Microscopic representation of the GBPC of CPKI preparation, (b) and (c) FE-SEM micrographs of CPKI, and (d)–(f) CV and GCD profiles indicating the stability of the symmetric device. Reproduced from ref. 78 with permission from Elsevier, Copyright 2021.

The synthesis of MXenes is carried out by the etching of the 'A' layer from the MAX phase. Here, "A" represents elements from groups 13 or 14, while the suffix "-ene" indicates structural similarity to graphene. The first MXene was published $Ti_3C_2T_x$ with high volumetric capacitance.[79–81] The 2D layer structure offers a large number of electrochemical reaction active sites with a pseudocapacitive mechanism for energy storage.[82,83] The termination groups and conductive properties of TMs make MXenes appealing electrode materials for supercapacitor applications.[79,84–87] Tian *et al.* synthesized $Ti_3C_2T_x$, which exhibits a distinct voltage distribution between the negative and positive electrodes when H_2SO_4 is used as the electrolyte. They demonstrated that the rise in the capacitance of the negative electrode is caused by the partial oxidation of the positive electrode. To increase the positive electrode's capacity to store energy, a redox-active electrolyte was added to H_2SO_4. By adding the redox electrolyte, we convert the capacitive energy storage mechanism to a battery type, achieving a high energy density. Moreover, the use of mixed electrolytes improves the cycling stability to 113.5% over 10 000 cycles.[81]

Ghidiu *et al.* have prepared a clay-like material and used it for the fabrication of flexible electrode films. The films demonstrated a high capacitance of 245 F g^{-1} at 10 A g^{-1} in a 1 M H_2SO_4 electrolyte.[88] Dall'Agnese has designed chemically modified $Ti_3C_2T_x$ to investigate the impact of delamination and intercalation on supercapacitive devices. The delamination phenomenon enhances the surface area and alters the surface chemistry of $Ti_3C_2T_x$ with an excellent capacitance of 325 F g^{-1} at 5 A g^{-1} in a 1 M H_2SO_4 electrolyte.[89] Li *et al.* have fabricated a $Ti_3C_2T_x$ MXene through surface modification that resulted in a threefold increase in the capacitance as compared to the pure MXene. The $Ti_3C_2T_x$ electrode demonstrated a capacitance of 517 F g^{-1} at 1 A g^{-1} when tested in a 1 M H_2SO_4 electrolyte. The material exhibited 99% capacity retention over 10 000 cycles.[90] Aymen *et al.* have designed a MXene/cobalt ferrite composite that exhibited excellent electrochemical performance compared to the individual CoF and MXene. The composite has shown a higher specific capacitance of 1268.25 F g^{-1} at 1 A g^{-1} in 0.1 M KOH with 97% capacity retention over 5000 cycles.[91] Guo *et al.*[92] designed aramid nanofibers (ANFs) and MXene

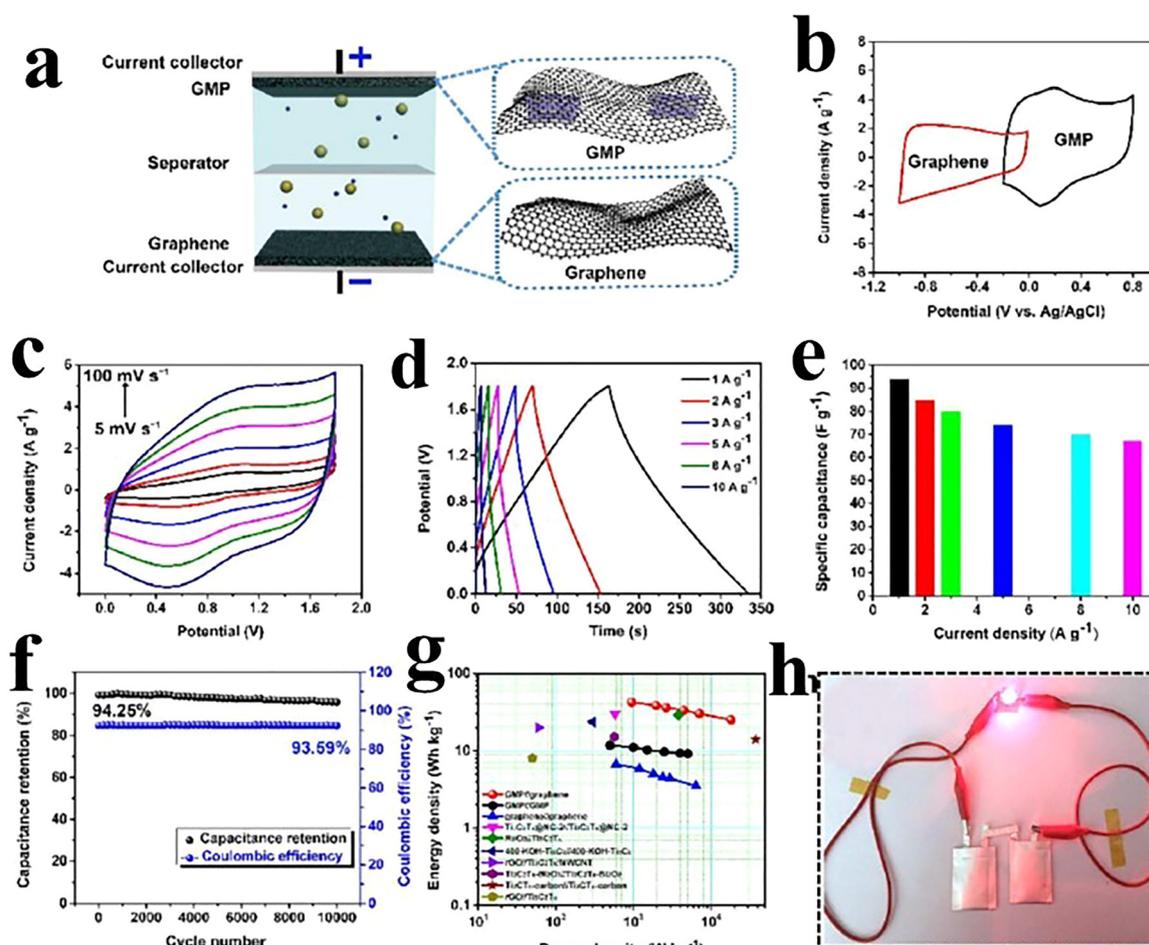**Fig. 5** (a) Schematic of a GMP/graphene ASC. (b) CV profiles of GMP and graphene at 5 mV s^{-1}. (c) CV profiles conducted at various scan rates ranging from 5 to 100 mV s^{-1}. (d) GCD profiles at various current densities ranging from 1 to 10 A g^{-1}. (e) Specific capacitance at 10 A g^{-1}. (f) Cyclic stability and Coulombic efficiency. (g) Ragone plot compared with previously reported literature data. (h) Visual representation when a red LED is illuminated by a series of two ASCs. Reproduced from ref. 93 with permission from the American Chemical Society, Copyright 2018.

composites, which achieved high conductivity (2247 S m^{-1}), tensile strength (61.53 MPa), and specific capacitance (246 F g^{-1} at 0.05 A g^{-1}). The assembled stretchable supercapacitor exhibited 32.6 F g^{-1} capacitance and excellent cycling stability (112.7% retention over 2000 cycles), and maintained performance under repeated crumpling and stretching, demonstrating strong flexibility and mechanical robustness. Fu and colleagues.[93] have fabricated a novel graphene-encapsulated MXene Ti$_2$CT$_x$@polyaniline (GMP) composite and investigated it as a supercapacitor electrode. As shown in Fig. 5(a). the pouch-type GMP/graphene asymmetric supercapacitor (p-ASC) was constructed utilizing GMP and an electrolyte of 1 M H$_2$SO$_4$. The ASC device demonstrated promising results without the polarization effect in the potential window of 0 to 1.8 V and CV profiles of GMP and graphene presented in Fig. 5(b). The CV profiles conducted at various scan rates within in the range of 5 to 100 mV s^{-1} are displayed in Fig. 5(c). The profiles of GCD exhibited quasi-linear as well as symmetric behaviour with IR drop and low internal resistance, as shown in Fig. 5(d) and (e). The device showed a specific capacitance of 94.5 F g^{-1} at a current density of 1 A g^{-1}. The p-ASC device exhibited an excellent cyclic stability of 94.25% over 10 000 cycles at 10 A g^{-1} with a coulombic efficiency of 93.59%, as shown in Fig. 5(f). The Ragone plot showed power densities of 950 and 18 000 W kg^{-1} at energy densities of 42.3 and 25 Wh kg^{-1}. Moreover, the symmetric devices of graphene//graphene and GMP//GMP were fabricated, and the Ragone plot is displayed in Fig. 5(g). Graphene//graphene has energy densities of 6.5 and 2.3 Wh kg^{-1} at power densities of 600 and 7250 W kg^{-1}, while the symmetric device has energy densities of 11.7 and 9 Wh kg^{-1} at power densities of 500 and 4985 W kg^{-1}. The practical viability of two p-ASCs connected in series is shown by a glowing LED in Fig. 5(h).

3.5. Transition metal dichalcogenides

TMDs are 2D materials based on TMs belonging to group IV to VI. TMDs are characterized by the general formula of MX$_2$, where M denotes a transition metal (Ti, Zr, V, Hf, W, Mo, Rh, Ir, Co, Re, Tc, Ni, Pd, Nb, Ta, and Pt) and X represents a chalcogen (Se, S, or Te). TMDs are comprised of a diverse range of materials.[94] These materials exhibit a broad spectrum of electronic properties including semiconducting, metallic, and superconducting characteristics.[95] The TMDs are sandwiched between the chalcogen atoms that are covalently bonded sheets. These sheets stacked on each other exhibit van der Waals interactions.[96] However, the TMs are surrounded by six chalcogen atoms which can be of octahedral or trigonal prismatic arrangement of MX$_6$ polyhedrons. These MX$_6$ polyhedrons are connected by shared edges creating a monolayer of TMDs.[59,97] Approximately 60 TMDs have been discovered to date. Among them, molybdenum disulfide (MoS$_2$), and tungsten disulfide (WS$_2$) are the most promising. TMDs consist of a wide range of materials such as semiconducting (MoS$_2$, WS$_2$, MoSe$_2$, and WSe$_2$), metallic (TaTe$_2$ and NbTe$_2$), semimetallic (MoTe$_2$), magnetic (VSe$_2$, VS$_2$, and CrSe$_2$), superconducting (NbSe$_2$), and topological insulating (WTe$_2$). Furthermore, TMDs

show a combination of properties like transparency, flexibility, and strength similar to graphenes.[98] TMDs are regarded as possible electrode materials for applications involving energy storage due to the distinctive combination of high surface areas with van der Waals interactions. Recently, researchers have concentrated on constructing TMD-based electrodes for supercapacitors to obtain a remarkable electrochemical performance. The synthesis of TMDs and their composites has led to various morphologies with high surface area and high porosity. This enhancement in surface area generates additional reaction sites and improves the supercapacitor performance. MoS$_2$ has gained attention due to the cost-effectiveness, natural abundance, chemical stability, broad range of negative potentials, and high specific capacitance. Alam et al.[99] have prepared two-dimensional TMD-based supercapacitors that exhibit high specific capacitance (up to 774 F g^{-1}), excellent rate capability (up to 10 A g^{-1}), and long cycle life (up to 10 000 cycles). Hybrid TMD nanomaterials enhance conductivity, reduce agglomeration, and optimize electrochemical sites, enabling high energy and power density with excellent cycling stability for advanced energy storage applications. Mishre et al. have designed a flower-like 2H-MoS$_2$ composite with a specific capacitance of 382 F g^{-1} at 1 A g^{-1} and a capacity retention of 97.5% over 4000 cycles. This excellent performance is attributed to the 3D structure of the composite with exposed surface in various petals.[100] The electrochemical performance of MoS$_2$-based materials was investigated by Gupta et al. A simple hydrothermal method was used to synthesize MoS$_2$ particles having a spherical flower-like structure. The materials showed a specific capacitance of 255 F g^{-1} at 0.25 A g^{-1} maintaining 70% of initial capacitance after 1000 cycles. In a different study, Fu et al. used electrospinning to synthesize MoS$_2$/graphene nanosheets embedded in activated carbon nanofibers (MoS$_2$@G/AC). A specific capacitance of 334 F g^{-1} at 0.5 A g^{-1} and 246.3 F g^{-1} at 10 A g^{-1} with 83.8% capacity retention after 5000 cycles at 0.5 A g^{-1} was observed for this material. MoS$_2$@G/AC has high active surface area and porosity with a synergistic effect induced by each component resulting in enhanced specific capacitance and stability. Wang et al. have prepared a MoS$_2$/PANI composite by incorporating 2H-MoS$_2$ using the in situ polymerization of aniline. The composite demonstrates a capacitance of 390 F g^{-1} at 0.8 A g^{-1} and exhibits great stability because of the hybridization of MoS$_2$ and PANI.[101] Ratha et al. have studied the electrochemical performance of WS$_2$/rGO hybrid electrodes, which demonstrate enhanced storage capacity than an individual component of WS$_2$ and rGO electrodes. This hybrid composite exhibiting a specific capacitance of 350 F g^{-1} in a 1 M Na$_2$SO$_4$ electrolyte was prepared by a simple hydrothermal approach. A large number of reaction sites are offered by the sheet-like structure of WS$_2$ for electrochemical reactions.[102] Tu et al. have used a molten–salt process to prepare WS$_2$/reduced graphene oxide nanosheets. A layered morphology was observed for the WS$_2$/rGO hybrid composite, resulting in a large number of reaction sites, which increased the conductivity. The WS$_2$/rGO hybrid composite shows a capacitance of 1355.67 F g^{-1} as compared to
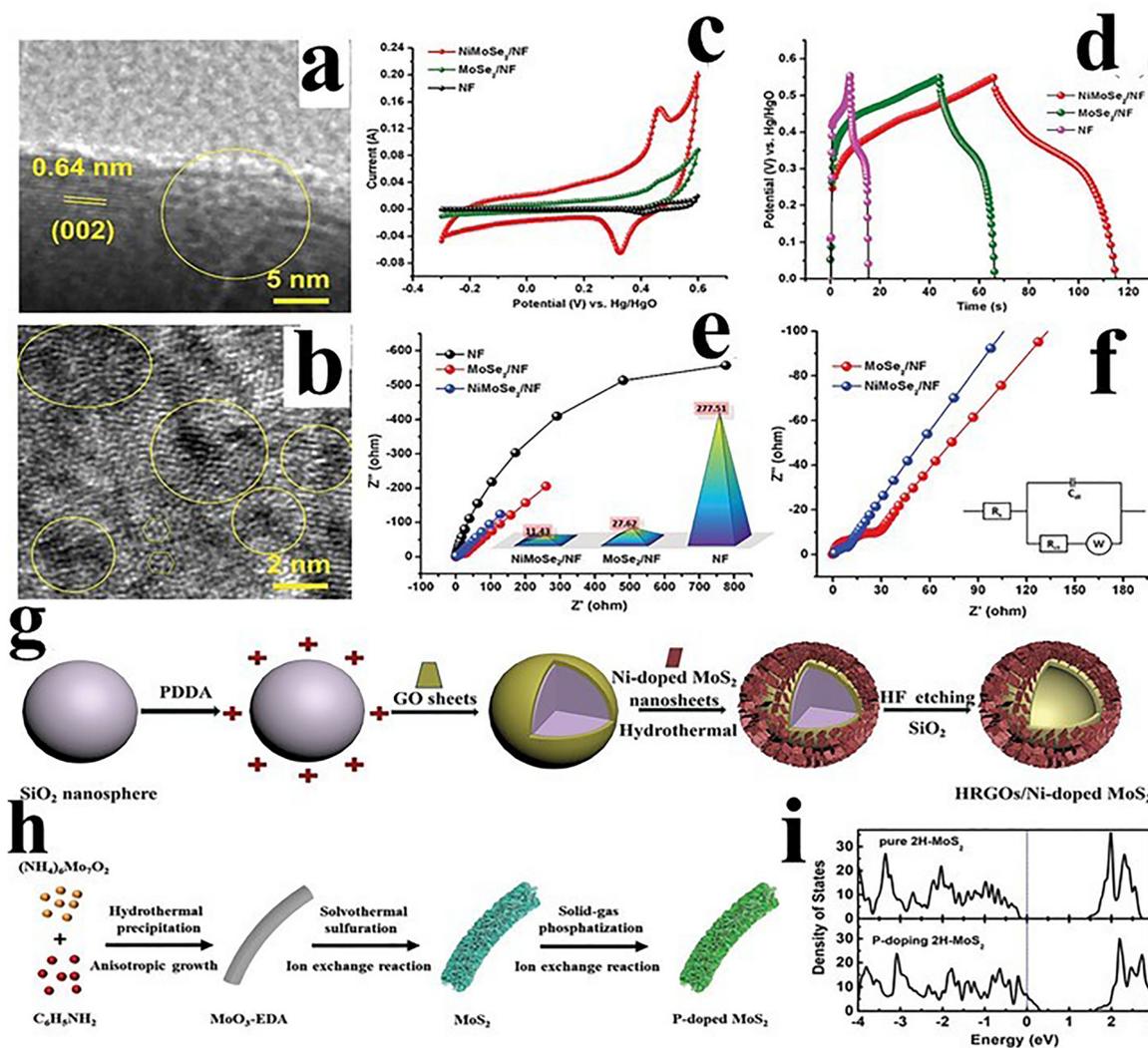
Fig. 6 (a) and (b) HR-TEM images, (c) CV profiles, (d) GCD profiles, (e) Nyquist plots, and (f) EIS profiles with Randle's model circuit fitting (inset) of $NiMoSe_2$ nanoplates. Reproduced from ref. 105 with permission from the American Chemical Society, Copyright 2019. (g) Representation of the synthesis of the HRGO/Ni-doped MoS_2 nanocomposite. Reproduced from ref. 106 with permission from Elsevier, Copyright 2020. (h) Schematic of the synthesis of P-doped MoS_2 nanowires. (i) Density of states of 2H-MoS_2 and P-doped MoS_2. Reproduced from ref. 107 with permission from Wiley-VCH, Copyright 2018.

their individual components with 98.6% capacity retention over 5000 cycles.[103] Lin *et al.* have investigated a ternary composite of MoS_2, WS_2, and rGO, which demonstrated a specific capacitance of about 365 F g^{-1} and a specific retention of 70% after 3000 cycles.[104] The semiconducting nature of TMDs results in poor electrical conductivity and reduced electron mobility as well as redox activities, which restrict the charging and discharging rate and compromise the cycling stability. The hybridization effect improves interfacial contact for facile electron transport that enables the easy intercalation of redox sites and causes high surface area for better electrochemical performance. Sakthivel *et al.*[105] have prepared Ni-doped $MoSe_2$ nanoplates by employing a hydrothermal method. The Ni doping created surface defects as can be seen from the high-resolution transmission electron micrographs (HR-TEM) displayed in Fig. 6(a) and (b). $MoSe_2$ demonstrates high specific capacitance

as evaluated from the CV and GCD techniques, as presented in Fig. 6(c) and (d). Nyquist plots were constructed, which showed a lower charge-transfer resistance that can be imagined from the behaviour of the profiles, as shown in Fig. 6(e) and (f). Chang *et al.*[106] have prepared novel hollow reduced graphene oxide sphere/Ni-doped MoS_2 (HRGO/Ni-doped MoS_2) nanocomposites, as shown in Fig. 6(g). The doped material demonstrates a specific capacitance of 544 F g^{-1} at 1 A g^{-1}, which is higher than that of the pristine material. On the other hand, the charge-transfer resistance reduced from 40.7 to 1.49 Ω. This indicates that the doping of transition metals including the Mn, Co, and Ni can improve the electron transport at the electrode interface, which ultimately enhances the storage performance of the 2D TMDs. Liu *et al.*[107] have prepared P-doped MoS_2, which exhibited excellent conductivity and faster redox kinetics, as shown in Fig. 6(h). The P-doped MoS_2 has a

larger bandgap than that of the pristine MoS_2, which demonstrates the metallic nature, as shown in Fig. 6(i). Therefore, a maximum energy density of 67.4 Wh kg^{-1} and a power density of 850 W kg^{-1} were achieved by the quasi-solid-state ACS device.

3.6. Hexagonal boron nitride

Hexagonal boron nitride (h-BN) has similar properties to graphenes with a honeycomb structure having sp^2 hybridization. In h-BN, boron and nitrogen are bonded with each other through strong covalent bonding. h-BN has weak van der Waals forces of interaction that connect the various layers.[108,109] h-BN has both crystalline and amorphous forms. The crystalline form has various allotropes such as h-BN, wurtzite (γ-BN), and sphalerite (β-BN). h-BN stands out due to its excellent stability and properties similar to graphite.[110] The h-BN has space groups of $P6_3/mmc$ with a hexagonal structure.[109] Its two-dimensional form has gained significant attention for applications in electronics, field emitters, ultra-violet visible (UV) emitters, and thermal radiators. It has remarkable thermal, mechanical, and electronic properties. Despite having a close structural similarity to graphene, h-BN has a wide bandgap of 5.9 eV and limited practical usage because of its weak electronic conductivity.[109,111] Research is ongoing to study the methods to enhance the conductivity of h-BN. With the enhancement in conductivity, it can stand out as a potential candidate in energy storage devices, both supercapacitors and batteries. Recently, scientists have focused on the development of graphene-based h-BN nanocomposites by taking advantage of graphene's exceptional conductivity.[111,112] Jiao et al. have investigated the h-BN-based nanocomposite with a specific capacitance of 250 F g^{-1} at 0.5 A g^{-1} in a 2 M KOH electrolyte.[111] Saha et al. have

prepared h-BN/rGO and studied the effect of rGO concentration on the composite, which plays a key role in enhancing the electrochemical performance. The composite showed a capacitance of 960 F g^{-1} with 80% capacity retention over 10 000 cycles.[113] Patil et al. have designed 2D/3D hybrid material of h-BN and rGO, which demonstrated high specific capacitance in both acidic and basic electrolytes. The van der Waals interactions are significant in the hybrid component. In both electrolytes, the hybrid exhibits specific capacitances of 304 and 226 F g^{-1} at 1 A g^{-1}, respectively. Over 10 000 cycles, the hybrid's capacity retention remained at 98%.[114] Zheng and colleagues have prepared h-BN/graphene composite by solution process method. The composite delivered a capacitance of 134 F g^{-1} at 10 A g^{-1} with 96% capacity retention over 10 000 cycles.[115] The π–π conjugation and narrow bandgap of h-BN due to the presence of carbon atoms within the composite are responsible for the high performance of the composite. Furthermore, the present additives and various h-BN phases change the band structure, improving the electrode's work function. Additionally, doping increases porosity, which improves the composite's stability and specific capacitance. Chikkatti et al.[116] designed a graphene-NH$_2$/hBN nanocomposite electrode that exhibited high specific capacitance (203.68 F g^{-1} at 0.75 A g^{-1}), excellent cycling stability (86% retention over 10 000 cycles), and superior energy density (102.12 Wh kg^{-1} at 2850 W kg^{-1}). The synergistic integration of hBN with G-NH$_2$ enhanced the charge transport and surface interactions, making it a promising material for high-performance supercapacitors. Krishnamoorthy et al.[117] developed an exfoliated h-BN/Bi$_2$S$_3$ nanocomposite through an ultrasonic approach that supports stacked layer formation with enhanced surface area and high conductivity. The
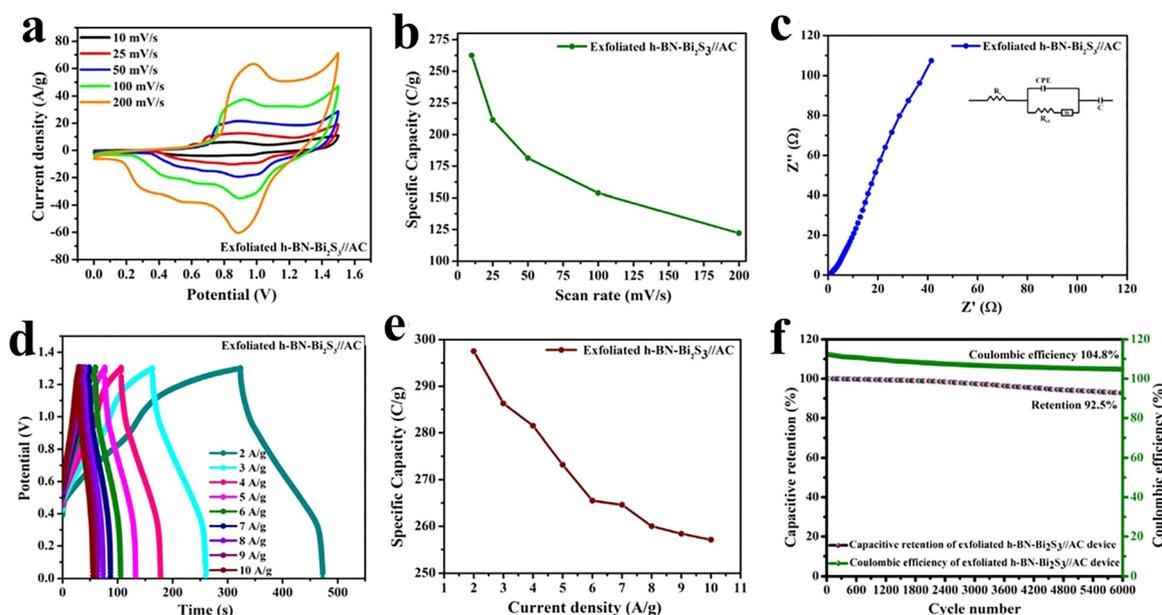

Fig. 7 (a) CV profiles, (b) scan rate against specific capacity plot, (c) EIS profiles, (d) GCD profiles, (e) current density against specific capacity of the h-BN–Bi$_2$S$_3$//AC hybrid device. (f) Cycling stability profiles of the h-BN–Bi$_2$S$_3$//AC hybrid device. Reproduced from ref. 117 with permission from the American Chemical Society, Copyright 2024.

h-BN-Bi$_2$S$_3$ nanocomposite was used to fabricate a hybrid supercapacitor (HSC) device with an AC counter electrode. The CV profiles were conducted in the potential window of 0 to 1.5 V at different scan rates ranging from 10 to 200 mV s^{-1}, indicating battery-type characteristics, as shown in Fig. 7(a). The specific capacity calculated is 262.5 C g^{-1} at a scan rate of 10 mV s^{-1}. The specific capacity as a function of scan rate is demonstrated in Fig. 7(b). The Nyquist plot was constructed, and the R_{ct} and R_s values evaluated are 1.12 Ω and 0.77 Ω, as seen from Fig. 7(c). The GCD analysis was performed in the potential window of 0 to 1.3 V at different current densities ranging from 1 to 10 A g^{-1}, as presented in Fig. 7(d). The maximum specific capacity value calculated was 297.5 C g^{-1} at 2 A g^{-1}. The specific capacity against the current density plot has been drawn, which indicates that the capacity values decreased with the increase in current density, as presented in Fig. 7(e). This trend might be of electrode polarization, ion diffusion, and sluggish kinetics. Moreover, the cyclic stability of the h-BN-Bi$_2$S$_3$//AC HSC device demonstrates an excellent capacity retention of 92.5% over 6000 cycles with a higher coulombic efficiency of 104.8%, as presented in Fig. 7(f).

3.7. Carbon nitrides

Carbon nitrides have gained huge attention in energy storage and catalysis due their 2D structure and properties like graphene.[118,119] Primarily, the seven distinct phases of carbon nitrides are α-C$_3$N$_4$, β-C$_3$N$_4$, cubic-C$_3$N$_4$, pseudocubic-C$_3$N$_4$, g-h-triazine, g-o-triazine, and g-h-heptazine. The graphitic carbon nitride (g-C$_3$N$_4$) phase demonstrates excellent stability under ambient conditions.[120,121] The g-C$_3$N$_4$ has sp^2 hybridization in carbon and nitrogen atoms, which are responsible for a π-conjugated electronic structure.[119,120] g-C$_3$N$_4$ is abundant, cost-effective, sustainable, and simple to prepare, with remarkable

chemical and thermal stability, exceptional optical characteristics, appealing electronic properties, and metal-free materials. These properties make g-C$_3$N$_4$ a potential applicant for the conversion of solar energy, photocatalysis, and identification of harmful molecules.[118–120,122] The 2D g-C$_3$N$_4$ is highly desirable for supercapacitors, and supports graphene sheets due to a large number of active sites. However, its low conductivity limits the applications at some points, but can be improved through composite formation with other materials.[120] The carbon nitride has been studied for various applications, but few investigations are reported for supercapacitors.[123–131] Shen et al. have reported the single-step fabrication of the activated carbon nitride using melamine and citric acid through pyrolysis. The variation in the temperature during the synthesis can alter the nitrogen/oxygen concentration that improves the surface area and specific capacitance. The capacitance observed was 185 F g^{-1} at 0.5 A g^{-1} which showed great potential of the material for supercapacitors.[124] Tahir and colleagues have designed tubular g-C$_3$N$_4$ for supercapacitors and delivered 233 F g^{-1} at 0.2 A g^{-1} with 90% capacitance retention after 1000 cycles. The excellent performance is due to the high surface area which offers by the unique architecture and presence of nitrogen/oxygen content. Moreover, the tubular g-C$_3$N$_4$ also exhibited remarkable photocatalytic performance. The promising results for supercapacitors and photocatalysts indicated the potential for energy storage and hydrogen production.[125] Tahir et al. also investigated the nanofiber (NF)-like g-C$_3$N$_4$ (GCNNF) for supercapacitor. The high amount of nitrogen in GCNNF and surface area improved the electrical conductivity. The GCNNF delivered a specific capacitance of 263.75 F g^{-1} at 1 A g^{-1} maintaining 96.3% capacity retention after 2000 cycles.[126] Manisha et al.[132] synthesized a magnesium oxide/graphitic carbon nitride/polpyrrole (MGP) composite
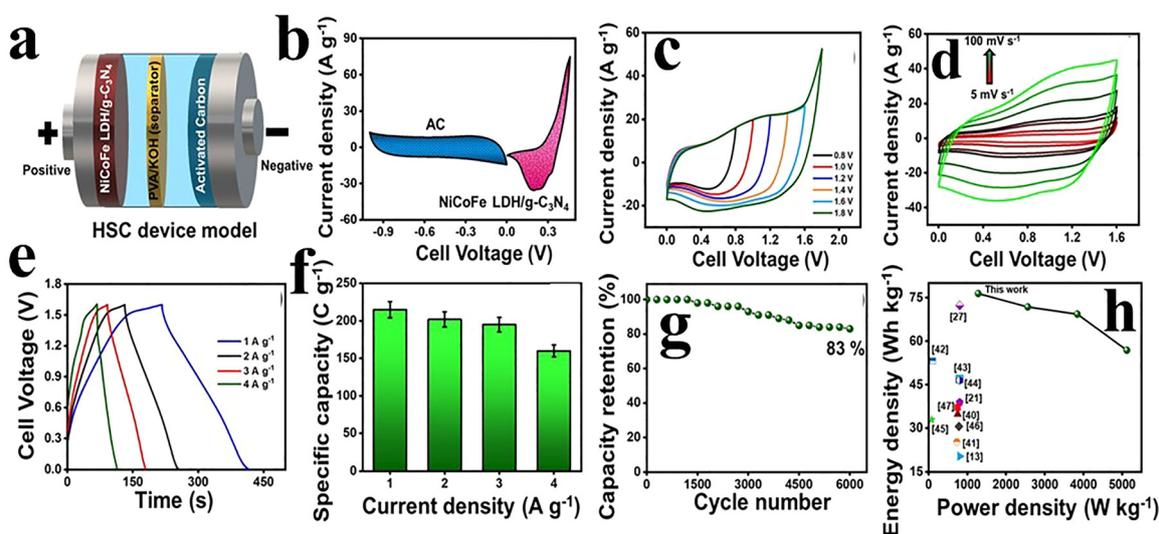
Fig. 8 (a) Schematic of the NiCoFe LDH/g-C$_3$N$_4$//AC HSC. (b) CV profiles of NiCoFe LDH/g-C$_3$N$_4$ and AC at 50 mV s^{-1}. (c) CV profiles of the NiCoFe LDH/g-C$_3$N$_4$//AC HSC in a different potential window. (d) CV profiles of the HSC at different scan rates. (e) GCD profiles of the NiCoFe LDH/g-C$_3$N$_4$//AC HSC at different current densities. (f) Bar plots of current density against specific capacity. (g) Cycling stability. (h) Ragone plot. Reproduced from ref. 133 with permission from Wiley-VCH, Copyright 2025.

Table 1 Performance of various 2D electrode materials for supercapacitors

Electrode material	Synthesis method	Electrolyte	Specific capacitance ($F\ g^{-1}$)	Energy density ($Wh\ kg^{-1}$)	Power density ($W\ kg^{-1}$)	Capacitance retention (%)	Ref.
NiFe$_2$O$_4$/CNT//AC	Thermal method	2 M KOH	118.36	23.39	466.66	87.2	134
PANI@HPCNFs@CNT	Electrospinning	1 M H$_2$SO$_4$	629.1	23.3	202.7	88.5	135
CoMoO$_4$@rGO	Hydrothermal	1 M KOH	1425	51.2	4500	92	136
AC//rGO	Hummers' method	1 M HCl	94.3	25.7	700.1	99	137
CNF/rGO composites	Electrospinning	3 M KCl	305	47.6	—	86.2	138
rGO/MXene-PPy	In situ polymerization	1 M aqueous H$_2$SO$_4$	408.2	11.3	500	88	139
PANI/GO/h-BN	Polymerization method.	1 M Na$_2$SO$_4$	351	—	4500	—	140
PANI/GO-Azo nanocomposite	Polymerization method	1 M H$_2$SO$_4$	426	12.45	274.9	98.5	141
AC	Pyrolysis process	1 M KOH	128	11.4	200	87	142
AC-CNS-750	Chemical activation	1 M Na$_2$SO$_4$	106	2.43	1002	87	143
CGO/PDAAQ@MXene	Etching method	1 M H$_2$SO$_4$	346	41	404	83	144
A-BP/Ti$_3$C$_2$T$_x$	Microfluidic spinning method	—	369	6.39	—	88.5	145
E$_3$/MnSe@Ti$_3$C$_2$T$_x$-45	Solvothermal	1 M KOH	721.4	28.68	308.23	83.4	146
Ti$_3$C$_2$T$_x$/MoS$_2$ heterostructure	Ultrasonic method	3 M H$_2$SO$_4$	169	6.3	30 000	91	147
2D WS$_2$ nanoflower	Hydrothermal	KOH	204	14	800	100	148
WS$_2$@MXene/GO nanocomposites	Hydrothermal	1 M KOH	320	114	—	—	149
MoTe$_2$/rGO	Hydrothermal	2 M KOH	1196.4	83.06	353.5	94.3	150
MoSe$_2$–PANI	Hydrothermal method	1 M KOH	146.5	22.16	198	54.5	151
3D MoS$_x$-PANI@RGO nanohybrid	Hydrothermal	3 M KOH	1365	29.5	8700	94	152
PANI/MoO$_3$/h-BN	In situ polymerization	6 M KOH	518	10.34	—	88.6	153
V$_2$O$_5$/h-BN	Hydrothermal	1 M KCl	408	25	2373	84.2	154
h-BN/G/MoS$_2$	Ball milling method	—	392	16.4	501	96.4	155
PANI/h-BN	Polymerization method	Na$_2$SO$_4$	927	26	921	97.6	156
AlN/g-CN	Plasma arc discharge process	1 M KOH	434.1	6.52	269.7	93.2	157
O-doped g-C$_3$N$_4$	Microwave irradiation	0.5 M Na$_2$SO$_4$	262.5	36.45	2500	73.1	158
PPy/g-C$_3$N$_4$/La$_2$O$_3$	In situ polymerization	1 M H$_2$SO$_4$	1763.56	198.18	450.01	—	159

electrode that exhibited high specific capacitance (1132.12 F g^{-1} at 5 mV s^{-1}), enhanced surface area (109.45 m^2 g^{-1}), and excellent cycling stability (94.03% retention over 10 000 cycles). The asymmetric supercapacitor device achieved an energy density of 9.25 Wh kg^{-1} at a power density of 302.72 W kg^{-1}, demonstrating strong potential for practical energy storage applications. Goncalves et al. further investigated pure C$_3$N$_4$ for supercapacitors prepared by the pyrolysis of urea followed by exfoliation. The material retained 89.2% of initial capacitance (113.7 F g^{-1}) over 5000 cycles.[127] Elanthamilan et al.[133] have designed a NiCoFe LDH/g-C$_3$N$_4$ composite using a hydrothermal method and investigated its supercapacitor applications. The composite-based hybrid supercapacitor (HSC) has been fabricated, as shown in Fig. 8(a). NiCoFe LDH/g-C$_3$N$_4$ was used as the positive electrode while AC was used as the negative electrode. The CV profiles of positive and negative electrodes are presented in Fig. 8(b). The positive electrode showed battery-type behaviour at a potential in the range of 0 to 0.46 V and the negative electrode had EDLC behaviour at a potential in the range of −1 to 0 V. Therefore, the theoretical evaluation of the potential window for HSCs is 0 to 1.46 V. Moreover, CV profiles were conducted at a potential in the range of 0 to 1.8 V at 50 mV s^{-1} to determine the perfect voltage range, as shown in Fig. 8(c). The CV profiles for HSCs were displayed at different scan rates with a battery-type nature, as shown in Fig. 8(d). Moreover, the GCD profiles at different current densities are displayed in Fig. 8(e). The specific capacity was calculated for NiCoFe LDH/g-C$_3$N$_4$//AC HSCs as 215 C g^{-1} at 1 A g^{-1}. The plot for specific capacity against the current density is displayed in Fig. 8(f). The HSC device's cyclic

performance is shown over 6000 cycles at 6 A g^{-1} in Fig. 8(g). The device retains 83% capacity performance, suggesting its excellent durability. The Ragone plot of the NiCoFe LDH/g-C$_3$N$_4$//AC HSC device was compared with the literature, as can be seen in Fig. 8(h).

3.8. Summary statement of 2D materials

Two-dimensional materials have emerged as transformative electrode platforms for supercapacitors due to their atomic-scale thickness, high surface-to-volume ratio, excellent electrical conductivity, and tunable surface chemistry. Carbon-based 2D materials such as graphenes, carbon aerogels, carbon foams, carbide-derived carbons, graphenes, CNTs, activated carbons, TMDs, h-BN, MXenes, and carbon nitrides provide large accessible surface areas and rapid electron transport pathways, making them highly effective for electric double-layer capacitance. Their porous and interconnected architecture facilitates efficient ion diffusion and high-rate capability, while the structural tunability enables the optimization of pore size and surface functionalities for enhanced charge storage.

Beyond carbon systems, layered materials such as TMDs, MXenes, and h-BN introduce additional pseudocapacitive behaviour through fast and reversible redox reactions. Their adjustable interlayer spacing, surface terminations, and electronic structures enable synergistic combinations of double-layer and faradaic charge storage. Through functionalization, heterostructure engineering, and composite design, 2D materials can achieve high specific capacitance, excellent cycling stability, and mechanical flexibility, positioning them as key

components for next-generation flexible, wearable, and high-performance supercapacitors (Table 1).

4. Choice of metal oxide-based pseudocapacitor electrode materials for supercapacitors

Metal oxide-based pseudocapacitor electrode materials have attracted significant attention for supercapacitor applications due to their fast and reversible surface or near-surface redox reactions, which enable high specific capacitance and enhanced energy density. TMOs exhibit multiple oxidation states that facilitate efficient charge storage through faradaic processes. However, the major challenge is poor cycling stability caused by volumetric expansion and structural degradation during repeated redox reactions. Many metal oxides also exhibit limited rate capability due to sluggish ion diffusion within the bulk structure. Additionally, low surface area and limited active sites can restrict effective charge storage, while dissolution or structural instability in aqueous electrolytes may further reduce long-term durability. To overcome these limitations, recent strategies focus on nanostructuring, defect engineering, and forming composites with conductive carbon materials or 2D substrates to enhance electron transport, ion diffusion, and structural stability. Various methods including intercalation, sol–gel, insertion, oxidative synthesis, hydrothermal synthesis, anodic deposition, and spray deposition are employed for their production.[14] Despite their high capacitance, metal oxides often suffer from poor stability due to electrode cracking caused by limited porosity.[160] To overcome this issue, they can be integrated with carbon materials to form composites. Mostly electrode materials used for making pseudocapacitors are based on carbon materials. Combining these carbon-based electrodes with nano-sized TMs like Co_3O_4, Fe_3O_4, MnO_2, and ZnO has shown extremely high values of specific capacitance. However, it is reported that metal oxides exhibit higher capacitive performance than the carbon materials.[13,161]

4.1. RuO_2

RuO_2 has been used as an electrode material since the discovery of pseudocapacitors in 1971, which store charge through the faradaic process. The TM ruthenium belongs to the platinum group where RuO_2 has both crystalline and amorphous structures that make it an appealing electrode material for supercapacitors.[162,163] Globally, ruthenium metal has 5000 tonnes of global reserves from which 12 tonnes are extracted annually.[75] Furthermore, RuO_2 has many advantages including a high theoretical specific capacitance of 750–2000 F g^{-1}, a wide potential window of 1.4 V, long life cycle, and enhanced thermal and chemical stability but generally suffer from lower conductivity and structural degradation during cycling. Consequently, while RuO_2 provides superior performance, its cost and scarcity limit its practical use, whereas other TMOs require strategies like nanostructuring or compositing with conductive materials to enhance their electrochemical performance. The

exchange of the electron and proton in hydrous RuO_2 causes charge storage. The two main factors involved are the selection of an appropriate electrode potential and the adjustment of the pH of the medium.[164] Moreover, in Li-ion batteries, RuO_2 has been broadly used as a positive electrode. Generally, the specific capacitance of RuO_2 fails to reach the theoretical values, which can be improved by making composites with other materials. Chandrasekhar et al. have synthesized rutile-structured RuO_2 using a spray deposition method, which resulted in a specific capacitance of 1158 F g^{-1}. Some factors including crystallinity, mixed water concentration, particle size, and annealing temperature influence the electrochemical performance of RuO_2-based electrode materials. The large-scale production of RuO_2-based electrode materials is restricted due to the high cost of ruthenium.[165] Despite the greater potential of RuO_2 for energy storage devices, the high cost restricts its practical use. The researchers have developed two methods to reduce the use of ruthenium and maximize the efficiency. The first method is to incorporate base metal oxides into RuO_2 via doping and the second one is to construct a composite material based on ruthenium where hydrous RuO_2 particles deposited on inexpensive materials such as conductive polymers, carbons, and other metal oxides.[166] In this regard, Korkmaz and colleagues have synthesized aerogel nanocomposites of rGO/RuO_2, which give a specific capacitance of 328.6 F g^{-1} at a scan rate of 5 mV s^{-1}. The fabricated supercapacitor devices based on rGO/RuO_2 delivered a high energy density of 31.1 Wh kg^{-1} at a power density of 8.365 kW kg^{-1}. The excellent performance of the rGO/RuO_2 aerogel nanocomposite is assigned to its high energy density, high rate capability, and high power density. Moreover, incorporating conductive materials endowed the rGO/RuO_2 aerogel nanocomposite with high capacitance.[167] Su-Hyeon Ji et al. have synthesized hydrous RuO_2 and hexagonal WO_3 and deposited them on 3D carbon cloth (CC) via a binder-free hydrothermal method. The fabricated hexagonal-WO_3/CC electrode exhibited a significant specific capacitance of 970.26 F g^{-1} at 5 mV s^{-1}. Furthermore, an ASC having hydrous RuO_2/CC as the positive electrode and WO_3/CC as the negative electrode in a H_2SO_4 aqueous electrolyte demonstrated a specific energy of 16.92 Wh kg^{-1} and a high stability of 171.75% after 6500 cycles. It also exhibited a high-rate stability of about 198.18% after 3000 cycles.[168] Vijayabala et al. synthesized RuO_2 nanosheets through a hydrothermal process with a PEG surfactant with controlled morphology. The electrochemical studies of RuO_2 nanosheets exhibited a high specific capacitance of 600 F g^{-1} and reversible redox reactions, which further prove that these sheets are the potential electrode materials for supercapacitors.[169] Jeon et al. have prepared RuO_2 nanorods on carbon nanofibers (CNFs). The fabricated electrode material in the KOH electrolyte solution exhibited a high specific capacitance of 188 F g^{-1} at 1 mA cm^{-2} with an energy density of 22–15 Wh kg^{-1}. It also retained a specific capacitance of 93% after 3000 cycles at 1 mA cm^{-2}. Xu et al.[170] prepared a Ru@RuO_2/graphene composite that exhibited an exceptionally high specific capacitance of 3189 F g^{-1} at 1 A g^{-1} with 85% retention at 50 A g^{-1}, demonstrating excellent rate

capability. The symmetric supercapacitor delivered a power density of 25 kW kg^{-1}, an energy density of 12.2 Wh kg^{-1} and 86% capacitance retention after 20 000 cycles, highlighting its superior electrochemical performance. Ramesh *et al.* fabricated hybrid electrodes based on a composite of Co_3O_4–RuO_2/nitrogen-doped graphene oxide through a hydrothermal process. The resulting specific capacitance values were 472, 395, 224, and 133 F g^{-1} at 0.5, 1, 2, and 3 A g^{-1}, respectively.[171] In addition, Chung *et al.* have reported the synthesis of RuO_2/carbon fibers through a wet impregnation method, where a wrinkle-like structure of the composites was formed after thermal treatment. The obtained composite showed high performance at 12.23% RuO_2 content with rapid electron and proton transfer. The maximum specific capacitance of 544 F g^{-1} has been obtained for RuO_2/carbon fiber. The increase in the concentration of RuO_2 has adversely affected the performance because of the hindrance proton transfer. Furthermore, increases in RuO_2 content in the composite affected the proton transfer due to the decrease in hydrous RuO_2, which resulted in a loss in the capacitive performance of the composite.[172] Zhao *et al.* have synthesized RuO_2/Ti_3C_2 *via* a chemical solution method. The addition of Ti_3C_2 increased the stability of the composite with a long-life cycle. Furthermore, the layered structure and high conductivity of Ti_3C_2 assist in rapid ion diffusion and electron transfer, leading to exceptional rate performance. The incorporation of phosphate ions into RuO_2 enhances the chemical reactivity, resulting in exceptional specific capacitance. This synthesized composite shows a remarkable specific capacitance of 612.72 F g^{-1} at a current density of 2 A g^{-1} in a H_2SO_4 electrolyte with a capacitance retention of 97.95% after 10 000 cycles.[173] Jiang *et al.*[174] investigated the CV curves of RuO_2 and $Ti_3C_2T_x$ at 50 mV s^{-1} for potential window optimization, indicating nearly equal charge storage. The asymmetric device was fabricated using plastic bags to seal the positive and negative electrodes with a polymer membrane as the separator. The working potential window for the asymmetric device was 1.6 V. However, the chosen window was 1.5 V to enhance the cycle life. The CV profiles at various scan rates with prominent redox peaks demonstrated the faradaic nature of the asymmetric device, as shown in Fig. 9(b). The GCD profiles at different current densities in the same potential window show the pseudocapacitive behavior of the electrode in Fig. 9(c). The device delivered a maximum capacitance of 93 F g^{-1} and retained 78 F g^{-1} even at 1000 mV s^{-1}, as displayed
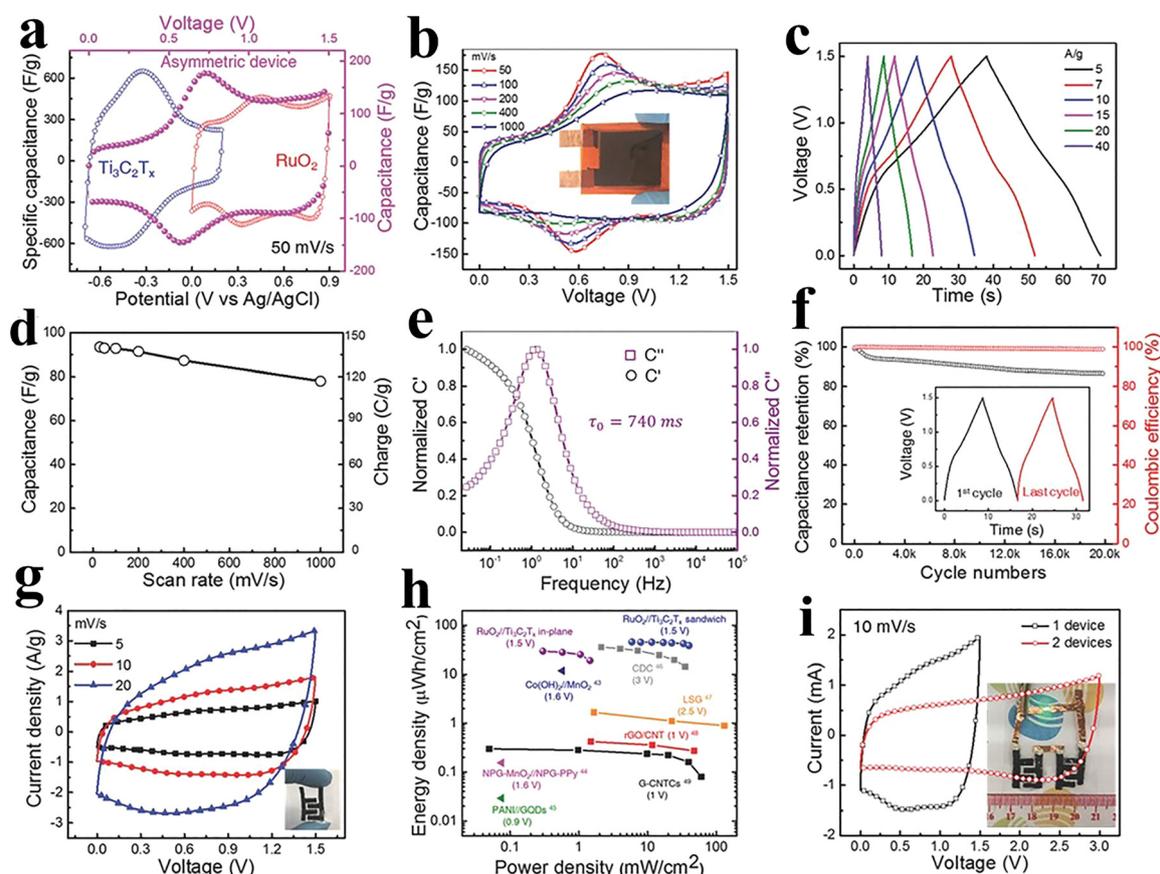

Fig. 9 Electrochemical investigations on the RuO_2//$Ti_3C_2T_x$ full-cell device: (a) CV profiles at 50 mV s^{-1}, (b) CV profiles at different scan rates, (c) GCD profiles at different current densities, (d) plot of specific capacitance against scan rate, (e) plot of normalized real/imaginary capacitance *versus* frequency of the device, (f) cycling stability and coulombic efficiency, (g) CV profiles of the polypropylene substrate, (h) Ragone plot of RuO_2/$Ti_3C_2T_x$ device compared with previously reported literature data. (i) CV profiles of RuO_2//$Ti_3C_2T_x$ tandem in-plane devices; inset: two devices connected in series to illuminate a green LED. Reproduced from ref. 174 with permission from Wiley-VCH, Copyright 2025.

in Fig. 9(d). The small relaxation time constant τ_0 of 740 ms confirmed the high-rate performance of the device, as can be seen in Fig. 9(e). The asymmetric device showed excellent capacitance retention of 86% with a coulombic efficiency of 100% over 20 000 cycles, as shown in Fig. 9(f). The CV profiles of the in-plane device were recorded at different scan rates within a 1.5 V potential window. The areal capacitance was measured to be 60 60 mF cm^{-2} at 5 mV s^{-1}, and even a high value of 50 mF cm^{-2} was achieved at 20 mV s^{-1}. The Ragone plot shows the areal energy and power density with various in-plane devices, as shown in Fig. 9(h). For real-world applications, tandem in-plane devices were assembled by connecting two asymmetric devices in series to deliver 3 V, as displayed in Fig. 9(i).

4.2. ZnO

ZnO is an attractive electrode material for supercapacitors due to its high theoretical capacitance, low cost, non-toxicity, and environmental friendliness. However, like many metal oxides, ZnO suffers from poor electrical conductivity and limited cycling stability, which can restrict its rate capability and long-term performance. Compared to RuO$_2$, which offers superior conductivity and capacitance, ZnO and other abundant oxides provide more sustainable and economical options but often require nanostructuring or hybridization with conductive carbon materials to achieve practical electrochemical performance. Metal oxides such as RuO$_2$, Fe$_3$O$_4$, ZnO, and MnO evolve as potential pseudoactive materials. Yafei et al. have designed zinc–cobalt and sulphide hybrid (ZCOSH) using the hydrothermal method. The ZCOSH has been compared with a binary zinc–cobalt oxide (ZCO) to investigate the capacitive performance. The evaluated capacitance is 2176.7 F g^{-1} for ZCOSH and 387.2 F g^{-1} for ZCO.[175] Subramani et al. have prepared a ZnO/rGO nanocomposite that delivered a specific capacitance of 203 F g^{-1} in a KOH electrolyte having a particle size of 1–2 μm.[176] Liu et al. have fabricated polyaniline/ZnO/ zeolitic imidazolate framework/graphene/polyester (PANI/ZnO/ ZIF-8/G/P) via a chemical bath technique. PANI/ZnO/ZIF-8/G/P demonstrates a capacitance of 40 F g^{-1} with a particle size of 500 nm to 500 μm.[177] Pant et al. have prepared a ZnO composite with ZnO/CNFs.[178] The composite showed 260 F g^{-1} in a KOH electrolyte with a size ranging from 300 nm to micrometres. Yadav and colleagues have examined a nanocomposite based on ZnO and activated charcoal. The nanocomposite delivered a specific capacitance of 341.6 F g^{-1} in NaOH and KOH electrolytes, with a particle size of approximately 30 nm.[179] Chee et al. prepared a PPy/GO/ZnO composite using an electrochemical deposition technique. PPy/GO/ZnO has delivered 123.8 F g^{-1} specific capacitance with a particle size of 50 μm.[180] Haldorai et al. prepared a ZnO/rGO composite employing ultrasonication and achieved a capacitance of 314 F g^{-1} in KOH with particle sizes within 5–10 nm.[181] Guo et al. have fabricated rGO/ZnO and sandwiched polyethylene terephthalate (PET) by chemical vapor deposition. The material showed 51.6 F g^{-1} in KCl.[182] Xiao et al. designed ZnO/carbon spheres by a hydrothermal method and demonstrated 630 F g^{-1} using a KOH

electrolyte.[183] Saranya et al. synthesized a graphene-ZnO nanocomposite via a solvothermal method. The composite delivered 122.4 F g^{-1} in KOH with a particle size 30 to 70 nm.[184] Ammar et al. prepared Li-doped ZnO nanorods (0.5% Li) that exhibited a high specific capacitance of 700 F g^{-1} at 1 mV s^{-1} and an impressive energy density of 56 Wh kg^{-1}. The material also demonstrated excellent cycling stability, highlighting the beneficial role of Li-induced defect engineering in enhancing the electrochemical performance.[185] Raj et al. designed a ZnO/ MnO$_2$ composite using the successive ionic layer adsorption and reaction (SILAR) technique, which showed an areal capacitance of 14 mF cm^{-2} in a Na$_2$SO$_4$ electrolyte.[186] Lee et al. constructed a ZnO/AC composite by a co-precipitation method with a capacitance of 155 F g^{-1} in Na$_2$SO$_4$ as an electrolyte.[187] Kim et al. designed a ZnO/AC nanofiber-based material through an electrospinning method. The material delivered a capacitance of 178.2 F g^{-1} in a KOH electrolyte.[188] Ramli et al. prepared carbon nanotube/graphite nanofiber/ZnO using a hydrothermal method. The composite showed a capacitance of 306 F g^{-1} in a H$_2$SO$_4$ electrolyte.[189] Yang et al. prepared a ZnFe$_2$O$_4$/rGO composite through a hydrothermal method. The composite showed a capacitance of 352.9 F g^{-1}.[190] Wang et al.[191] designed an asymmetric supercapacitor (ASC) device by the combination of graphitic carbon nitride (GCN) and ZnO nanofibers (NFs), which showed fast redox reactions, as depicted in Fig. 10(a). The ZnO NFs which are exposed to ultrasonic cavitation display a fluffy morphology due to their strong interaction with the nitrogen active sites available on the surface of GCN nanosheets. This structure introduces gaps within the ZnO NFs that facilitate rapid inclusion and removal of larger K$^+$ ions, leading to enhanced pseudocapacitive performance. The device for the ASC was made utilizing GCN/ZnONFs as positive electrodes, AC as the negative electrode, and a piece of fibre filter paper acting as the diaphragm (GN/ZnONFs//AC-ASC) with 3 mol KOH as an electrolyte. Fig. 10(b) shows the reaction mechanism displayed by positive and negative electrodes during CV tests, which shows that the negative electrode of AC offers a smaller double-layer capacitance due to ion adsorption and the pseudo-capacitance of the positive electrode material primarily contributes to the overall capacitance characteristic. CV and GCD tests were performed on GCD/ZnONFs// AC-ASC to identify the optimal voltage window for capacitive charge storage. CV profiles were obtained in a potential window ranging from −1 V to 0.6 V at a scan rate ranging from 10 to 100 mV s^{-1}, as shown in Fig. 10(c). The asymmetric supercapacitor device maintains a stable curve even at a high scan rate of 100 mV s^{-1}, demonstrating potential for a high-multiplier power device having rapid charging and discharging rate. GCD profiles are obtained at current densities ranging from 1 to 6 A g^{-1}, as shown in Fig. 10(d). The resulting charge/ discharge plateau at 1.5 V displays promising pseudocapacitive properties of the device. The GCD results revealed that the GCN/ZnONFs//AC-ASC device offers a maximum specific capacitance of 64 F g^{-1} at a current density of 1 A g^{-1}, maintaining the coulombic efficiency of 80%. The device also displays a specific capacitance of 26.6 F g^{-1} at a scan rate of 10 mV s^{-1}, as
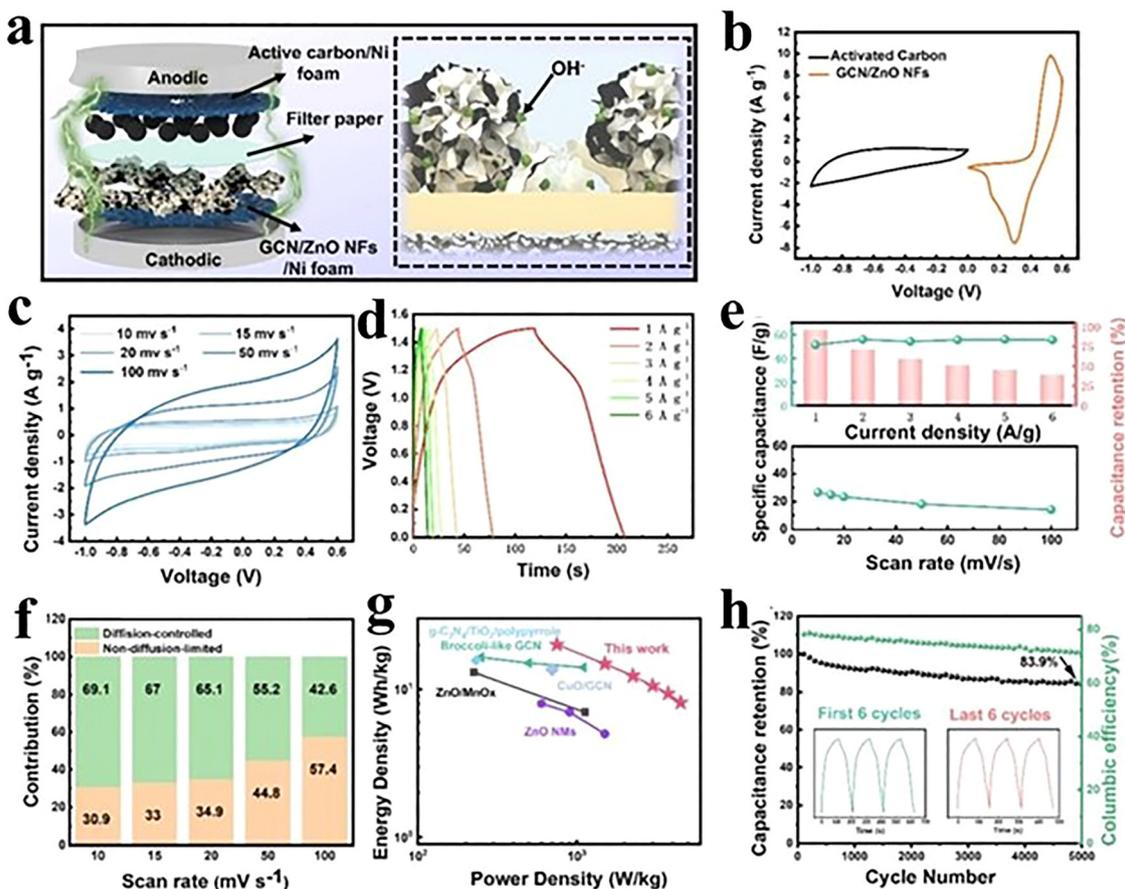
Fig. 10 (a) Schematic of the ASC assembly. (b) CV profiles at 10 mV s^{-1}. (c) and (d) CV and GCD profiles at different scan rates and current densities. (e) Specific capacity of the fabricated device. (f) Quantitative contribution from capacitive and diffusive capacitance for the device. (g) Ragone plot. (h) Cycling stability tested at 1 A g^{-1}. Reproduced from ref. 191 with permission from Elsevier, Copyright 2024.

shown in Fig. 10(e). Fig. 10(f) displays the capacitance control contribution of the GCN/ZnONFs//AC-ASC material, which indicates that the material exhibits a large value of pseudo-capacitance contribution. Fig. 10(g) shows the relationship between the energy density and the power density of the GCN/ZnO NFs//AC-ASC device. The maximum energy density of 20 Wh kg^{-1} with a power density of 750 W kg^{-1} and an energy density of 8.125 Wh kg^{-1} at a high value of power density of 4500 W kg^{-1} were calculated. This GCN/ZnONFs//AC-ASC device performance is excellent in comparison to that exhibited by a two-electrode system composed of GCN and ZnO. The cycling stability of the GCN/ZnO NFs//AC-ASC device is shown in Fig. 10(h). These results reveal that the device exhibited good capacitance retention at 86.6% over 5000 cycles at a current density of 1 A g^{-1}. This value of capacitance retention is superior to that displayed by ZnO NFs//AC over 5000 cycles (69.5%).

4.3. NiO

NiO is a widely studied pseudocapacitor material due to its high theoretical capacitance, chemical stability, and relatively low cost. It allows fast surface redox reactions, making it suitable for energy storage applications. However, NiO suffers from poor intrinsic electrical conductivity and limited rate capability, which can reduce its practical performance.[192–194] Luo *et al.* have investigated the ion adsorption/desorption of NiO during the intercalation of Li-ions. The presence of the (111) plane in NiO is responsible for the formation of Li$_{0.296}$NiO on its surface. Moreover, surface changes occurred during the electrochemical reaction.[195] However, the electrochemical performance of NiO was affected due to the low conductivity and availability of limited active sites. To overcome these problems, novel strategies should be employed like the fabrication of NiO electrodes at a nanoscale level, which will improve the effective surface area. Another way to improve the storage performance is to fabricate hybrids with conductive materials.[196] These hybridized nanostructures result in enhanced electrical conductivity and facilitate efficient charge transfer.[197] Balaji *et al.* designed a NiO–CeO$_2$/rGO nanocomposite that exhibited a high specific capacitance of 212 F g^{-1} at 1 A g^{-1}, low resistances (R_s = 0.669 Ω, R_{ct} = 0.07 Ω), and excellent cycling stability with 96.7% retention over 15 000 cycles. The assembled hybrid device (NiO–CeO$_2$/rGO//AC) delivered 129 F g^{-1} at 1 A g^{-1}, 40 Wh kg^{-1} at 746 W kg^{-1}, and 88.84% retention after 15 000 cycles, demonstrating strong potential for high-performance supercapacitors.[198] Zhang *et al.* prepared a composite of ZnO/NiO

on 3D graphene doped with nitrogen. The composite delivered 1839.4 F g^{-1} which is attributed to the higher conductivity of ZnO. The 3D nitrogen-doped graphene framework serves as a buffer layer, suppressing ZnO expansion during charge–discharge processes at higher current densities.[199] Navale and colleagues have fabricated a composite of NiO/PANI that has a specific capacitance of 936.36 F g^{-1} in a Na$_2$SO$_4$ electrolyte.[200] Huang et al. prepared PANI/NiO/sulphonated GO to investigate the supercapacitance performance. The composite showed excellent performance due to efficient ionic and electronic conductivity.[201] Feng et al. prepared a NiCo$_2$O$_4$/NiO/Co$_3$O$_4$ nanocomposite, which delivered a specific capacitance of

1693 F g^{-1} at 1 A g^{-1}.[202] Chime et al. have reported that the NiO-based electrode materials demonstrate excellent performances.[203] Zhao et al. have designed a CeO$_2$/NiO composite that demonstrated 1250.44 F g^{-1}.[204] Mashkoor et al.[205] fabricated a symmetric supercapacitor device of rGO@Cu–NiO to investigate the energy storage capacity. The CV profiles of rGO@Cu–NiO obtained at different scan rates ranging from 10 to 100 mV s^{-1} in a potential window of 0 to 1.2 V are presented in Fig. 11(a). It was observed that the CV curves maintained their symmetry exceptionally even at higher scan rates, signifying that the fabricated device exhibited good capacitive performance. The capacitive properties of the fabricated device are
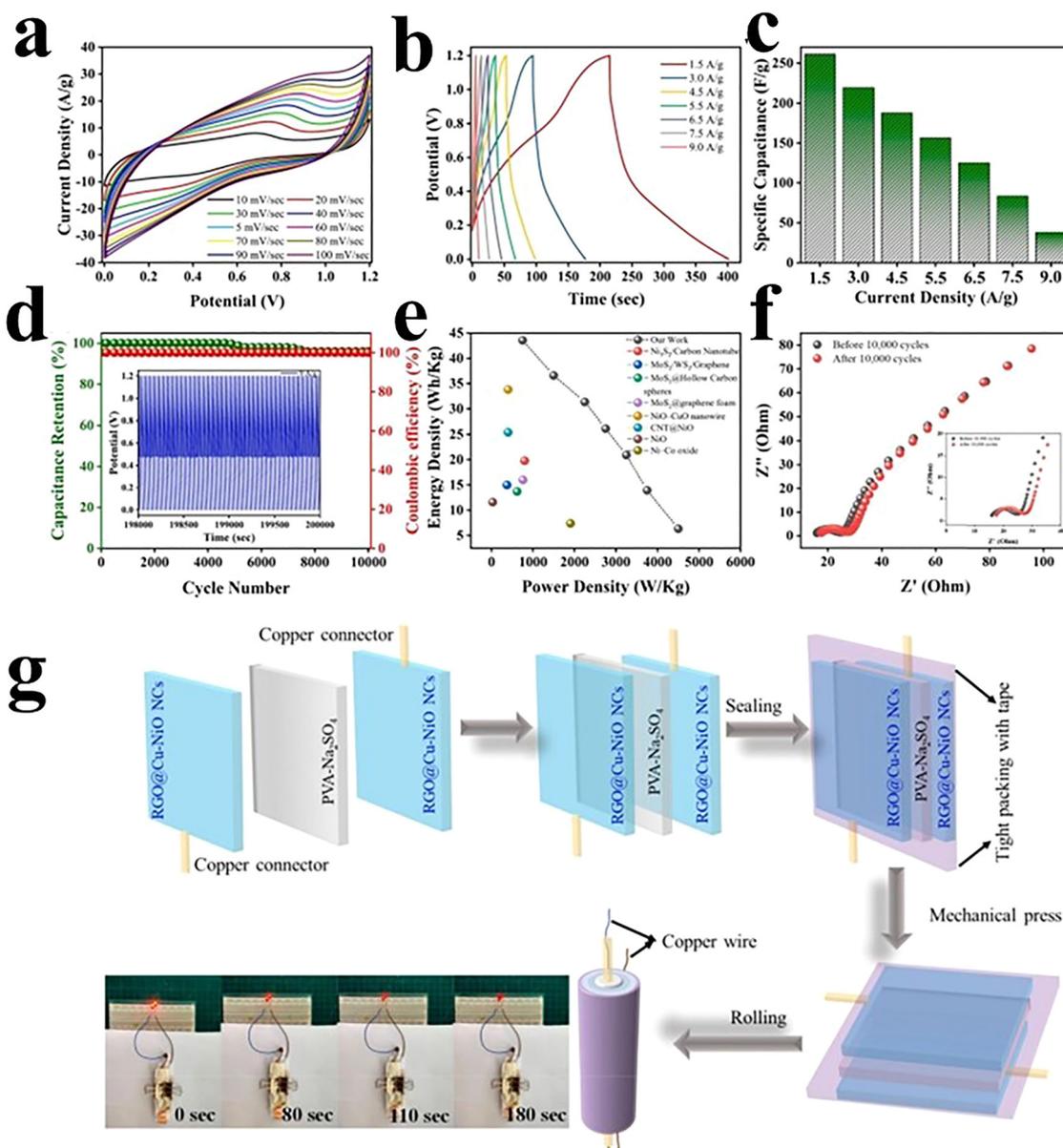
Fig. 11 Electrochemical investigations on rGO@Cu–NiO NC-based SSD. (a) CV profiles at different scan rates ranging from 10 to 100 mV s^{-1}. (b) GCD profiles at different current densities ranging from 1.5 to 9 A g^{-1}. (c) Specific capacitance at different current densities. (d) Capacity retention for 10 000 cycles at 9 A g^{-1}. (e) Ragone plot values compared with previously reported literature data. (f) Nyquist plots before and after the stability test. (g) Schematic of the fabricated device. Reproduced from ref. 205 with permission from Elsevier, Copyright 2024.

confirmed by the absence of any evident redox peaks in CV profiles. The GCD profiles of the rGO@Cu–NiO device conducted at different current densities – 1.5, 3, 4.5, 6.5, 7.5, and 9 A g^{-1} – are presented in Fig. 11(b). The specific capacitance values calculated are 261.25, 219.45, 188.1, 156.75, 125.4, 83.6, and 38 F g^{-1}, respectively. This indicates that 52% of capacitance was maintained with the increase in current densities from 1 to 6.5 A g^{-1}, as illustrated in Fig. 11(c). The device shows 96% of capacity retention even after 10 000 cycles, demonstrating high stability with a coulombic efficiency of 100%, as shown in Fig. 11(d). The Ragone plot showed the high energy density values, as displayed in Fig. 11(e). The energy densities exhibited by the device are 43.54, 36.58, 31.35, 26.13, 20.90, 13.93, and 6.33 Wh kg^{-1} at 750, 1500, 2250, 2750, 3250, 3750, and 4500 W kg^{-1}, respectively. The EIS plots of the device before and after 10 000 cycles are presented in Fig. 11(f). The device exhibits admirably low values of internal and charge transfer resistance, which highlight the consistent performance. The interactions between rGO and Cu–NiO components are responsible for the excellent performance of the device. The practical effectiveness of the device was checked by performing tests on the rGO@Cu–NiO-based device by powering an LED. The device was able to keep LED lit for 180 s, as shown in the inset of Fig. 11(g). These results confirm the potential of rGO@Cu–NiO for energy storage applications.

4.4. Co₃O₄

Co$_3$O$_4$-based electrode materials have gained significant interest due to low cost, high theoretical specific capacitance, and environmental friendliness. Additionally, the capacitive behaviour can be enhanced by tuning the configuration of Co$_3$O$_4$. Despite having the potential for energy storage applications, Co$_3$O$_4$ alone is not able to attain the optimal performance. Various studies have been carried out, such as making composites with other materials to enhance the energy density and the power density.[206,207] For instance, a composite of Co$_3$O$_4$ and graphene displayed excellent properties for supercapacitors.[208] Currently, efficient methods were applied to produce core–shell Co$_3$O$_4$ mesoporous nanospheres,[209] Co$_3$O$_4$ nanorod arrays,[210] hollow coral-shaped Co$_3$O$_4$ nanostructures,[211] and porous Co$_3$O$_4$ nanowires.[212] These materials exhibited distinctive electrochemical storage properties. The Co$_3$O$_4$ nanowires offer improved ion diffusion kinetics during charging/discharging cycles in comparison to 2D oxide nanosheets and nanoparticles.[213] The performance of Co$_3$O$_4$ is influenced by its shape and microstructure. Furthermore, the capacitance of Co$_3$O$_4$ has been enhanced by using ZIF-67 MOFs to prepare the composites. The MOF-based composite delivered a specific capacitance up to 770 F g^{-1} at 1 A g^{-1} retaining good cycling stability.[214] Moreover, Co$_3$O$_4$ can be combined with binary metal oxides to elevate the electrochemical performance.[215] Salethraj et al. synthesized RGO-decorated Co$_3$O$_4$ nanorods that exhibited enhanced electrochemical performance with a specific capacitance of 710 F g^{-1} at 10 mV s^{-1} and 681 F g^{-1} at 2 A g^{-1}. The improved behavior is attributed to the synergistic interaction between pseudocapacitive Co$_3$O$_4$ and conductive

RGO, which enhances electron transport and electrolyte accessibility.[216] Lv et al. have fabricated the ASC device based on the Co$_3$O$_4$/COV$_x$O$_y$ core–shell NS arrays. A further study examined the effect of varying current densities on the electrochemical performance of Co$_3$O$_4$@Ni foam (NF), Co$_3$O$_4$/CVO@NF-80 and Co$_3$O$_4$/CVO@NF-100. The comparison of specific capacitance of these electrodes demonstrated that Co$_3$O4/CVO@NF-80 has greater specific capacitance than the other two electrodes and is a promising candidate for supercapacitor applications. The composite exhibited a specific capacitance of 1162.2 F g^{-1} at 1 A g^{-1} with a remarkable rate capability and good cycling stability.[217] Zhu et al. have used a direct hydrothermal approach to produce two-dimensional porous ZnCo$_2$O$_4$ thin sheets.[218] The prepared ZnCo$_2$O$_4$ displayed an energy density of 36.31 Wh kg^{-1} at 850 W kg^{-1}. Zhang et al.[219] have prepared a composite of Co$_3$O$_4$/NiO (CNO) derived from boron carbonitrides (BCN) to enhance the capacitive performance. The BCN-N1//BCN/CNOs ASC was fabricated to test the practical performance of the material. The CV analysis was conducted at different scan rates in a potential window of 1.3 V with excellent current–voltage responses, as presented in Fig. 12(a). Fig. 12(b) shows the GCD curves obtained in a range of current densities such as 1, 2, 3, 5 and 8 mA cm^{-2} with specific capacitance values of 379.6, 273.8, 264.2, 253.8 and 233.8 mF cm^{-2}, respectively. EIS demonstrates the excellent electrical conductivity, fast charge and ion transfer efficiency, as presented in Fig. 12(c). The device showed good stability over 10 000 cycles at 10 mA cm^{-2} and the capacity retention of ASC was 89.09%, as shown in Fig. 12(d). The device exhibit an energy density of 0.089 mWh cm^{-2} at a power density of 0.65 mW cm^{-2}, indicating the excellent high-discharge power performance. The obtained results confirm that exceptional behaviour of the BCN/CNO material for energy storage applications.

4.5. MnO₂

MnO$_2$ has evolved as a progressive supercapacitive material due to various aspects such as abundance, non-toxicity, stability, and a high theoretical capacitance of 1370 F g^{-1}.[220] Moreover, the performance of MnO$_2$ is significantly influenced by its crystal structure, which exists in five different forms, e.g., α-, β-, γ-, λ-, and δ-MnO$_2$, which are interconnected by MnO$_2$ octahedrons in different ways.[221,222] MnO$_2$ exists in several crystallographic forms, including α, β, and γ phases with one-dimensional tunnel structures, δ phase with a two-dimensional layered structure, and λ phase with a three-dimensional spinel structure.[223] Additionally, all forms have different electrical conductivities that impact the pseudocapacitive nature of the material. Extensive research focused on combining 1D and 2D materials with MnO$_2$ to produce composites. Moreover, the morphologies of MnO$_2$ on nanoscale-like nanowires, nanorods, nanofibers, and nanotubes largely influence the charge storage capacity,[224] for instance, GO/MnO$_2$ and graphene/AC film-type electrodes.[225] MnO$_2$/MnCo/rGO hybrids[226] and MnO$_2$–GO nanocomposites were prepared by using a hydrothermal approach.[227] These nanocomposites exhibit improved electrochemical performance.[228] Xu et al. fabricated a hierarchically
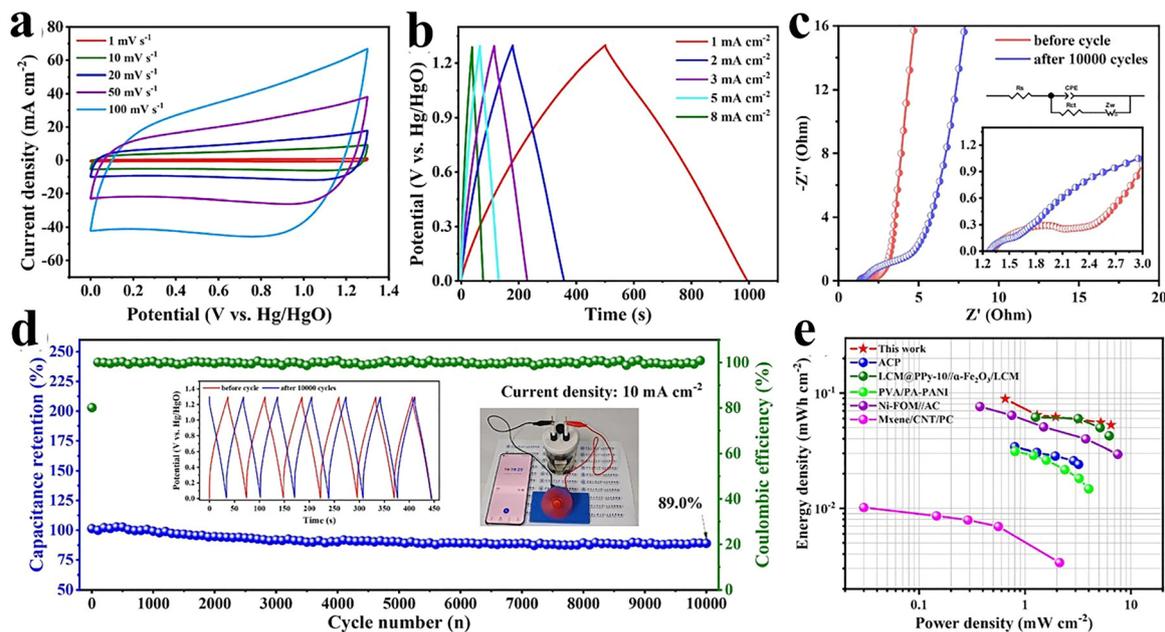
Fig. 12 Electrochemical investigations on the BCN-N1//BCN//CNO-based ASC: (a) CV profiles, (b) GCD Profiles, (c) Nyquist plots with fitted lines, (d) cycling stability tested for 10 000 cycles, and (e) Ragone plot values compared with previously reported literature data. Reproduced from ref. 219 with permission from Elsevier, Copyright 2025.

porous nanosheet of MnO_2 nanofibers used as the electrode material for supercapacitors. The material exhibited an aerial capacitance value of 3.30 F cm^{-2}.[229] Tholkappiyan et al.[230] have prepared spinel-type Mn_2O_3 nanoparticles via ultrasonic-assisted co-precipitation, forming a tetragonal hausmannite phase with spherical morphology. Electrochemical studies showed pseudocapacitive behavior with a specific capacitance of 296 F g^{-1} and low resistance, highlighting enhanced supercapacitor performance due to surfactant and ultrasonic-assisted synthesis. Xi et al. synthesized MnO_2-based electrodes in order to enhance the capacitive performance of the electrode. A hydrothermal technique was used to prepare 3D porous hybrid nanocomposites of MnO_2–$Ni(OH)_2$ wrapped on NF with the help of PVDF/acetylene black.[231] The hybrid nanocomposite electrode displayed an areal capacity of 4.86 CF cm^{-2} and an areal capacitance of 10.15 F cm^{-2} at 4 mA cm^{-2}. Tholkappiyan et al.[232] designed and synthesized novel Mn_2O_3 nanoparticles using an eggshell membrane as the template, forming a cubic structure with a porous morphology. Electrochemical studies revealed pseudocapacitive behavior with a high specific capacitance of 394 F g^{-1} and low transfer resistance, indicating excellent supercapacitor performance. Additionally, 86% capacity retention was observed after 10 000 cycles at 50 mA cm^{-2}. However, MnO_2 has high theoretical capacitance but still needs a lot of effort to improve the performance of energy storage systems. Mondal et al.[233] fabricated an ASC having gadolinium-incorporated MnO_2 (GMO)-coated graphite and copper sheets as the anode and cathode. In this two-electrode system, a filter paper immersed in a 0.1 M KOH electrolyte is used as a charge separator. The device was constructed by sandwiching the filter paper dipped into an

electrolyte between the two electrodes. The CV profiles of the GMO-coated graphite anode and copper electrodes scanned at 100 mV s^{-1} are presented in Fig. 13(a). Fig. 13(b) presents the CV profiles which were recorded at different scan rates from 5 to 100 mV s^{-1}. The diffusion-controlled contribution towards total current is higher than the surface-capacitive contribution at 5 and 100 mV s^{-1} for the two-electrode system, as shown in Fig. 13(c)–(e). It is found that there is an increase in diffusion-controlled contribution with the decrease in scan rate because at lower scan rates, the K^+ ion has enough time for diffusion in the porous electrode. Therefore, it is evident that in a two-electrode setup, electrochemical performance is governed by diffusion kinetics. The GCD profiles were conducted at current densities in the range of 0.5 to 3 A g^{-1}, as presented in Fig. 13(f). The maximum specific capacitance is reported to be 392.5 F g^{-1} at 0.5 A g^{-1}. The change in specific capacitance with current densities is represented in Fig. 13(g). Ragone plot demonstrates the energy and power densities values at different current densities as in Fig. 13(h). The maximum energy density achieved by the ASC is 78.5 Wh kg^{-1} with a power density of 106.1 W kg^{-1} at a current density of 0.5 A g^{-1}. The device delivers a maximum power density of 498.1 W kg^{-1} and an energy density of 9.13 Wh kg^{-1} at 3 A g^{-1}. The device shows a capacitance retention of 85.3% over 5000 cycles as in Fig. 13(i).

4.6. Iron oxide

MFe_2O_4 (M represents a divalent metal ion) has emerged as a promising electrode for supercapacitor applications due to its cost effectiveness, environmental friendliness, remarkable electrochemical performance, and natural abundance.[234] Iron oxide has been employed in various applications such as
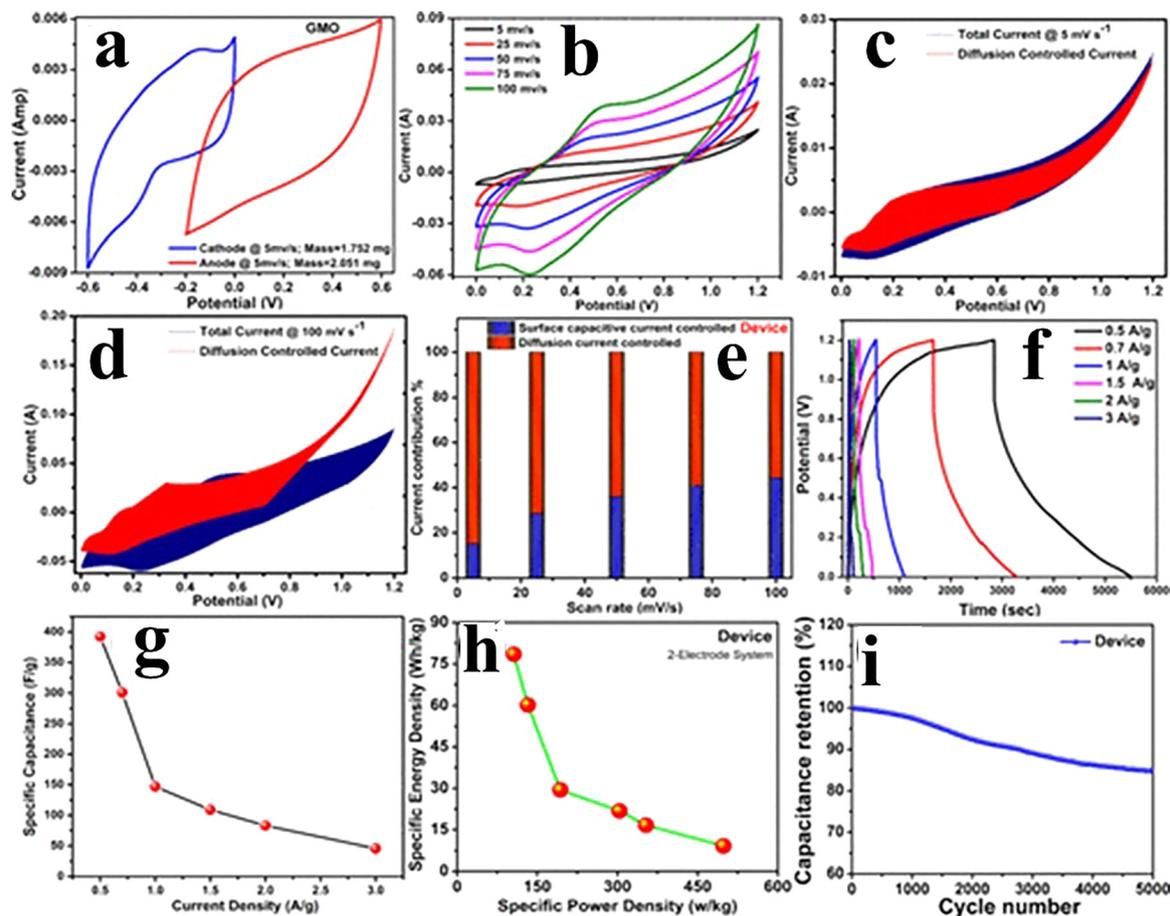
Fig. 13 (a) CV profiles of the cathode and anode of the GMO sample conducted at 100 mV s^{-1}. (b) CV profiles at different scan rates ranging from 5 to 100 MV s^{-1}. (c) and (d) Quantitative contribution from surface and diffusive capacitance at 5 mV s^{-1} and 100 mV s^{-1}. (e) Surface and diffusion contribution shown *via* bar plot. (f) GCD profiles at various current densities ranging from 0.5 to 3 A g^{-1}. (g) Plot of current densities against specific capacitance. (h) Ragone plot. (i) Cycling stability of ASD for 500 cycles. Reproduced from ref. 233 with permission from the American Chemical Society, Copyright 2024.

electrochemical energy storage, photoelectrochemical hydrolysis, and photo-catalysis. It exists in different oxidation states including Fe$_2$O$_3$, Fe$_3$O$_4$, and FeO.[235] Numerous synthetic approaches are used for the synthesis of iron oxide-based materials, such as the solvothermal method, hydrothermal process, sol–gel method, electrodeposition method, and thermal decomposition method.[236–238] The storage capacity of iron oxide can be elevated by making the composites with potential materials resulting in improved rate capability, cycling stability, and electrical conductivity.[239] Chen *et al.* synthesized iron-based derivatives using Fe$_3$O$_4$, FeOOH, and Fe$_2$O$_3$, exhibiting an increased theoretical specific capacitance value of 2299, 3625, and 2606 F g^{-1}, respectively. Furthermore, these can function in a broad potential window and are compatible with aqueous electrolytes. The operating potential window of these materials is −1.0 to 0.77 V.[240] It has been reported that a high value of theoretical specific capacitance is shown by all iron oxides. Fe$_2$O$_3$ stands out with much higher values among the others. Shivakumara *et al.* have synthesized porous α-Fe$_2$O$_3$ nanostructures by sol–gel techniques. It was reported that these nanostructures displayed a high surface area and remarkable

supercapacitance performance. A specific capacitance of 300 F g^{-1} was exhibited by a nano-Fe$_2$O$_3$ electrode, which is greater than the value of capacitance delivered by bulk Fe$_2$O$_3$ (40 F g^{-1}) at the same current density. The electrode showed a capacity retention of 73% even after 1000 cycles at 2 A g^{-1}, which revealed its excellent stability. The Nyquist plots of α-Fe$_2$O$_3$ and bulk Fe$_2$O$_3$ show that α-Fe$_2$O$_3$ exhibits a small resistance (4 Ω) than bulk Fe$_2$O$_3$ (9.5 Ω).[241] It is the outcome of the creation of an impurity band, which helps electrons jumping from the valence band to the conduction band, and less resistance facilitates the charge transfer, which results in enhanced supercapacitive performance. The specific capacitance of superconductors can be improved by combining with other conductive materials including carbons or polymers to form composites. A composite material featuring Fe$_2$O$_3$ nanotubes integrated with conductive polymer PANI was synthesized by Azimov *et al.* The synthetic scheme and SEM images clearly confirm the α-Fe$_2$O$_3$ nanotube (α-NT), PANI@α-NT-a, and PANI@α-NT-b. It is revealed by the SEM image that PANI completely covers the surface and the rod shape of α-NT is retained. GCD displayed that the composite PANI@α-NTs

exhibited a greater value of specific capacitance than the individual PANI or α-NT.[242] The increment in capacitance is attributed to the integration of conductive polymers, which enhances the conductivity and promotes charge transfer during electrochemical reactions. Another study was carried out to improve the conductivity of the core/shell structure of Fe_2O_3 with $NiCo_2O_4$. Zhang *et al.* designed a $NiCo_2O_4@Fe_2O_3$ composite without and using a binder and an additive, which demonstrated lower interface resistance and enhanced electron transfer.[243] Singh *et al.* prepared a waste banana stem–derived carbon/Fe_3O_4 composite that exhibited a high specific surface area of 1337.6 $m^2\ g^{-1}$ and delivered a specific capacitance of 787.8 $F\ g^{-1}$ at 0.5 $A\ g^{-1}$, with 64.3% retention at 12 $A\ g^{-1}$ and excellent cycling stability. The assembled solid-state ASC achieved an energy density of 63.58 $Wh\ kg^{-1}$ at 500 $W\ kg^{-1}$, demonstrating its potential as a cost-effective and sustainable supercapacitor electrode material.[244] A composite composed of Al_2O_3 nanoparticles on Fe_2O_3 integrated with CNTs was prepared by Chen *et al.* The composite displayed potential for excellent performance with specific capacitances of 2371 $F\ g^{-1}$

and 1277 $F\ g^{-1}$ with a capacity retention of 95.38% over 5000 cycles. The composites $Al_2O_3/Fe_2O_3@CNTS/Na_2SO_4$ and $Fe_2O_3@CNTS/Na_2SO_4$ exhibited a lower charge transfer resistance and faster kinetics.[245] Iron oxides exhibit high specific capacitance, high-rate ability, and excellent stability, which make them a potential candidate for electrode materials. Despite these benefits, there is still room for improvement in the performance of iron oxide-based electrode materials. This improvement can be achieved by fabricating composites that offer low resistance and efficient charge transfer.

Abbas *et al.*[246] have prepared a hematite α-Fe_2O_3 nanoparticle-supported rGO composite through a cost-effective co-precipitation method. The α-Fe_2O_3/rGO composite was used as a positive electrode and AC as a negative electrode with a hybrid electrolyte for the fabrication of a prototype asymmetric coin cell supercapacitor. The schematic of the assembled device α-Fe_2O_3/rGO//AC is presented in Fig. 14(a). The CV profiles conducted at various potentials are presented in Fig. 14(b). The GCD analysis performed in a potential range of 0 to 1.5 V is shown in Fig. 14(c). However, the CV curves conducted at scan
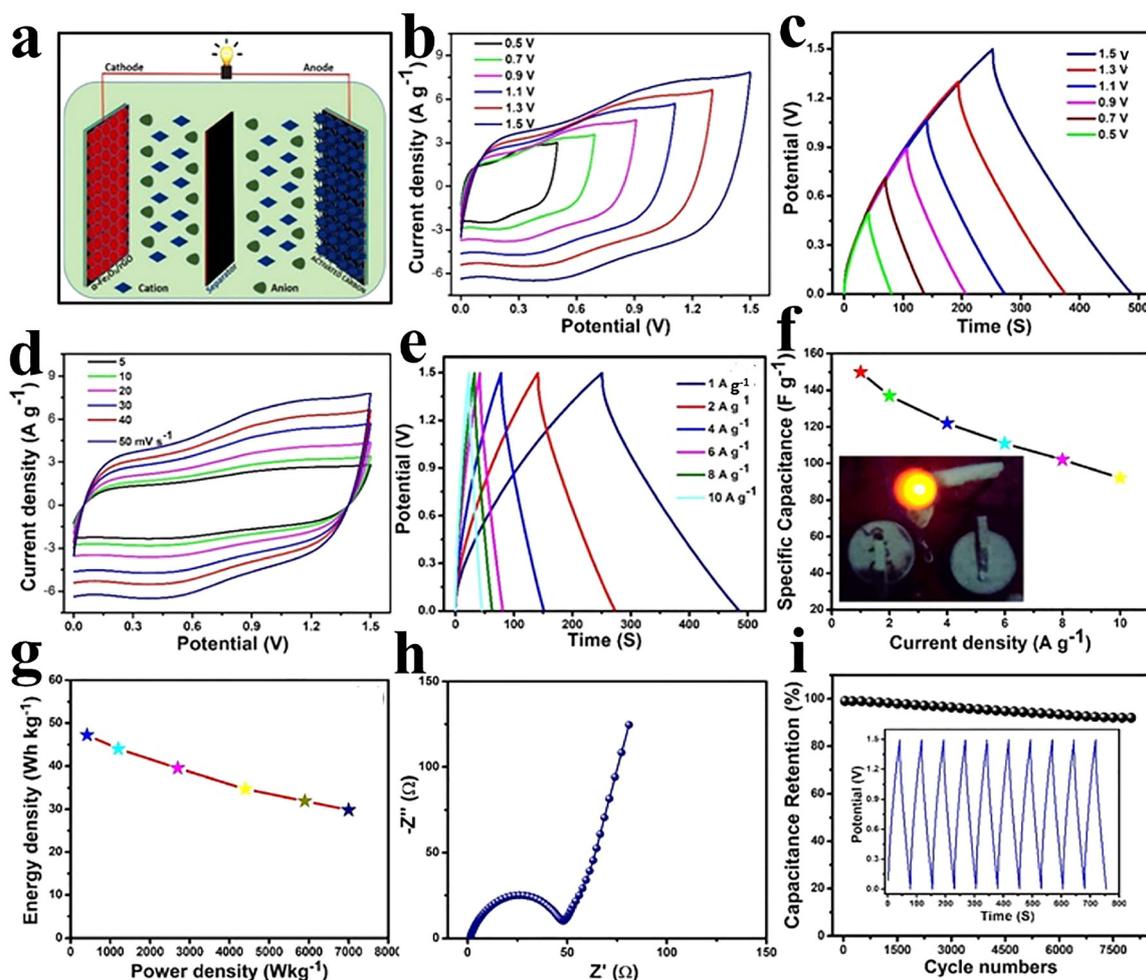
Fig. 14 Electrochemical investigations on the α-Fe_2O_3/rGO//AC-based device: (a) schematic of the device. (b) CV profile at 50 mV s^{-1}. (c) GCD profiles. (d) CV profiles at different scan rates ranging from 5 to 50 mV s^{-1}. (e) GCD profiles at different current densities. (f) Specific capacitance against different current densities. (g) Ragone plot. (h) Nyquist plot. (i) Cycling stability. Reproduced from ref. 246 with permission from Elsevier, Copyright 2025.

rates from 5 to 50 mV s^{-1} are displayed in Fig. 14(d). The CV curves demonstrate good capacitive behavior. The GCD profiles reveal excellent reversibility and coulombic efficiency, as shown in Fig. 14(e). The device delivers a highest specific capacitance of 150 F g^{-1} at 1 A g^{-1}, which remains at 91 F g^{-1} even at 10 A g^{-1}, demonstrating good rate capability; its practical applicability is further confirmed by powering a real-time LED as shown in Fig. 14(f). The Ragone plots shows a high energy of 47.1 Wh kg^{-1} and a power density of 245.5 W kg^{-1}, as depicted and compared with the reported values in Fig. 14(g). The Nyquist plots confirmed the improved kinetics of the assembled device, as shown in Fig. 14h. The device demonstrates an excellent capacity retention of 94% over 8000 cycles and the first 10 cycles show stability at 6 A g^{-1}, as shown in Fig. 14(i).

4.7. V_2O_5

V_2O_5 is applied as an electrode material in supercapacitors due to its physiochemical properties.[247,248] These properties include remarkable chemical stability, broad working potential window, and various oxidation states, which lead to improved energy storage performance.[249,250] However, V_2O_5 suffers from several disadvantages that limit its practical application. Its poor electrical conductivity reduces the charge–discharge efficiency and limits the rate performance. Additionally, it exhibits structural instability and significant volume changes during cycling, leading to poor long-term stability. The material also faces slow ion diffusion within its layered structure, which further restricts high-rate capability. To overcome these challenges, V_2O_5 is often nanostructured or combined with conductive carbon-based materials to enhance conductivity, ion transport, and cycling durability. Lee and colleagues have first described the potential of V_2O_5 to be used as an electrode material with a specific capacitance of 3505 F g^{-1} in a KCl electrolyte.[251] The fabrication of nanostructures of V_2O_5 has widened the scope for supercapacitor electrodes. Wee et al. used an electrospinning method to synthesize V_2O_5 NFs.[251] The V_2O_5 NFs delivered a specific capacitance of 190 F g^{-1} and an energy density of 5 Wh kg^{-1} in a 2 M KCl electrolyte. A Li-ion-containing organic electrolyte delivered even better performance where V_2O_5 NFs exhibited a specific capacitance of 250 F g^{-1} and an excellent energy density of 78 Wh kg^{-1}.[251]

It has a range of oxidation states from 0 to +5, resulting in a variety of compounds such as V_2O_3, VO_2, and V_2O_5.[252] Several environmental factors like temperature, pressure, and acidity/basicity influence the reduction of V_2O_5 to VO_2 [MT 89, 90]. Moreover, V_2O_5 has gained considerable attention in Li-ion, Mg-ion, and Na-ion battery electrodes.[253,254] The high specific capacitance and cost-effectiveness make it an attractive material for supercapacitors. Among other vanadium oxides, V_2O_5 exhibits enhanced conductivity and excellent stability having a melting temperature of 685 °C.[255] The intercalation process occurring in the crystal structure of V_2O_5 is due to pseudocapacitive behaviour. These processes include intercalation and de-intercalation of ions which effectively improve the morphology and surface chemistry of V_2O_5.[256] The combined effect of

2D layered structure and 3D morphology having interrelated channels promotes the effective electrolyte ion diffusion phenomenon on V_2O_5-based electrodes.[257] The optimization of ionic accessibility plays a key role in increasing the rate capability during charge/discharge cycling. Additionally, V_2O_5 displays excellent structural stability when exposed to different electrolytes which may be organic or aqueous in nature. This helps to optimize the wide operating potential window for V_2O_5 materials.[257] The broad range of potential window results in an improved energy density value for supercapacitor devices. A single V_2O_5 monolayer exhibits the highest theoretical capacitance of 883 F g^{-1} (ref. 258) in a potential window of 1.2 V.[259] Meanwhile, the experimental values of capacitance are low in comparison to theoretical values due to the less utilization of theoretical surface area of the electrode. The overall capacitance of V_2O_5 is influenced by the ion adsorption and intercalation process. However, these processes are driven by the porosity and morphology of the material. Three unique morphologies of V_2O_5 including bulk, stacked, and 3D architectures were compared by Zhu et al.[260] The complicated 3D morphology displayed better electrochemical performance owing to greater specific capacitance, energy density, and power density. In comparison to other structures, the 3D morphology exhibits greater surface area leading to better electrochemical performance. The greater surface area displayed by 3D morphology is attributed to the preferred orientation accompanied by the development of channels by interrelated 2D V_2O_5 sheets. The calibrated structure promotes effective ion diffusion, achieving an excellent specific capacitance of 451 F g^{-1} at 0.50 A g^{-1} in a 1 M Na_2SO_4 electrolyte. This value of specific capacitance exceeds the values exhibited by stacked V_2O_5 (314 F g^{-1}) and bulk V_2O_5 (108 F g^{-1}), demonstrating the benefits of 3D morphology for supercapacitor applications. The influence of crystal structure and morphology on the electrochemical performance of V_2O_5 is crucial. The amorphous oxides display less energy losses, attributed to the availability of channels that promote ionic diffusion.[261] The specific capacitance of V_2O_5 is influenced by the morphology. The fabrication of V_2O_5 in multiple crystalline morphologies including nanowires and flower-shaped flakes is investigated by Qian et al.[262] The 1D V_2O_5 nanowires exhibited a high value of initial capacitance (349 F g^{-1}) owing to their high surface area (123 m^{2}g^{-1}) but a noticeable drop of 27.6% in their capacitance was observed only after 200 charge/discharge cycles. However, an improved capacitance value (from 42 to 127 F g^{-1}) was displayed by hydrated V_2O_5 curly bundled nanowires due to the presence of nanopores within the structure. V_2O_5 microstructures with multiple unique morphologies including rhombohedral, flower-shaped, and butterfly-shaped were prepared by Zheng et al.[263] These morphologies exhibited excellent capacitances of 556, 641, and 609 F g^{-1} at 0.5 A g^{-1} in 1 mol L^{-1} LiClO$_4$ electrolyte. The performance of the rhombohedral structure is dependent on the morphology that facilitates the effective surface polarization even if the concentration of the electrolyte is very small. However, significant surface polarization of both the butterfly-shaped and flower-

shaped morphologies needs high amounts of electrolytes. Additionally, a decreased value of electrical resistivity for rhombohedral structure (0.76 Ω) in comparison to flower (1.17 Ω) and butterfly-shaped structures (1.22 Ω). This leads to rapid ionic diffusion within the rhombohedral morphology and results in an improved capacitance. These observations indicate that the crystal structure and morphology play a key role in fine-tuning the electrochemical performance of V_2O_5 for supercapacitor applications. Bai et al.[264] has prepared a composite of V_2O_5/PANI, which attained a high capacitance value and remarkable stability. They observed the outstanding values of power and energy density with a capacitance retention of 90% after multiple recharging and discharging cycles. A nanocomposite of V_2O_5/PPy/GO was studied by Asen et al.[265] The composite delivered excellent specific capacitance at high current density along with high energy density and power density values with remarkable cycling stability retention after thousands of cycles. The nanocable-based supercapacitor device based on G-V_2O_5/PEDOT was fabricated by Bi et al.[266] These devices displayed excellent specific capacitance with a higher energy density in a neutral electrolyte. Significantly,

these supercapacitors exhibited remarkable cycling stability, maintaining 120% of their initial capacitance over 50 000 cycles. These findings indicate the potential of V_2O_5 composites to be used as supercapacitors with greater capacitance, fast charging, and excellent stability. Rahman et al. designed a flexible, transparent V_2O_5/PVA supercapacitor that exhibited a specific capacitance of 178.7 F g^{-1} at 10 mV s^{-1}, an energy density of 7.8 Wh kg^{-1}, and a power density of 9.6 kW kg^{-1}, with excellent cycling stability (82% retention after 10 000 cycles) and mechanical flexibility. The device also demonstrated 70% optical transmittance and eco-friendly biodegradability, making it suitable for sustainable wearable electronics.[267] Karuppaiah et al.[268] deposited V_2O_5/ZnO on a flexible substrate using a magnetron sputtering technique. The fabricated thin films were used for a transparent symmetric supercapacitor (TSSC) device sandwiched by a LiCl/PVA gel electrolyte. The TSSC device showed 50% transparency, as shown in the inset of Fig. 15(a). The device was intensively investigated by electrochemical techniques such as CV, GCD, and EIS. The voltage window was optimized through CV at a fixed scan rate, as shown in Fig. 15(b). A sharp peak was
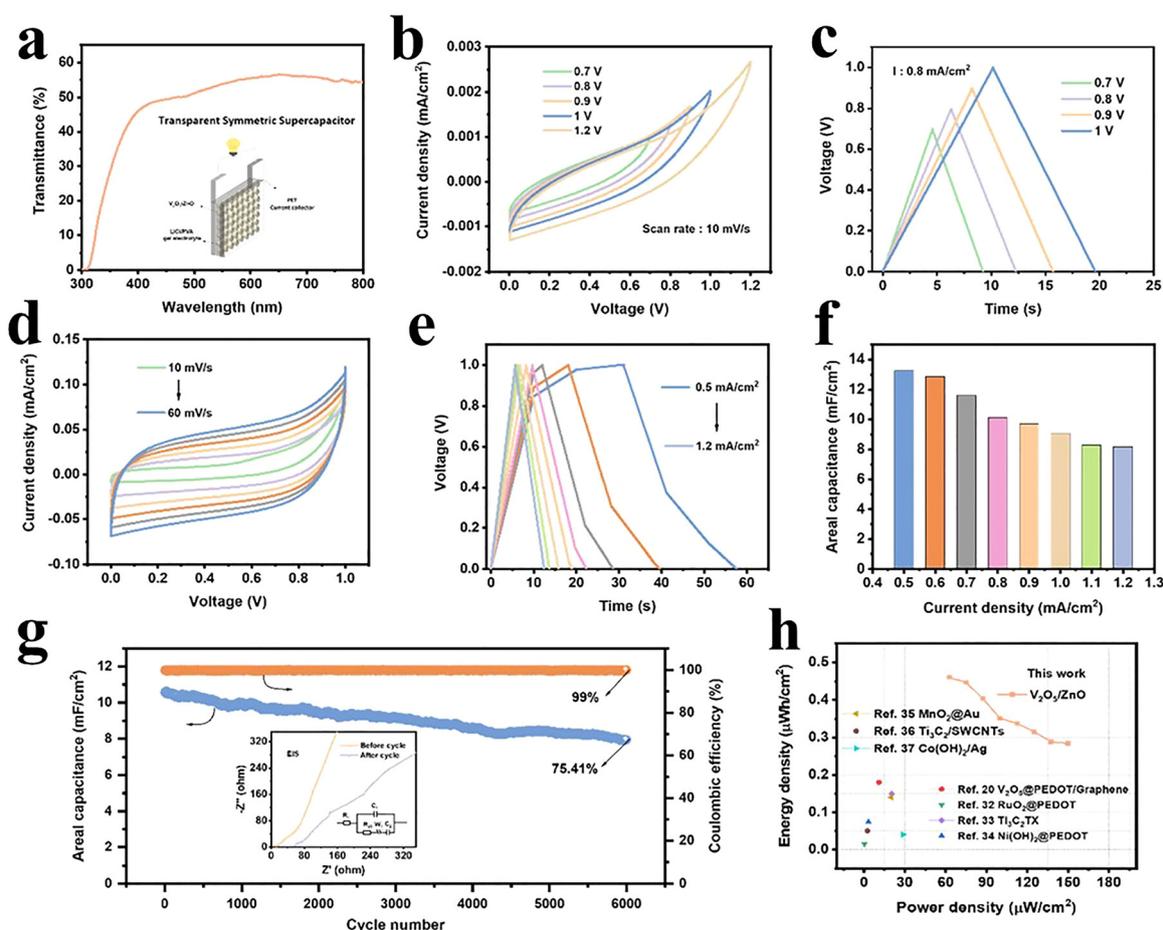
Fig. 15 (a) Representation of the transmittance spectrum of the TSSC device with schematic of the device in the inset. (b) and (c) CV and GCD profiles at 10 mV s^{-1} and 0.8 mA cm^{-2} at different voltages. (d) and (e) CV and GCD profile from 10 to 60 mV s^{-1} and 0.5 to 1.2 mA cm^{-2} at a fixed voltage. (f) Plot of areal capacitance against current density, (g) cyclic stability and inset EIS specta of TSSC device. (h) Ragone plot values compared with previously reported literature data. Reproduced from ref. 268 with permission from the American Chemical Society, Copyright 2024.

observed above 1 V, which can be attributed to the electrolyte decomposition. Therefore, the optimized voltage was 1 V for further studies. Moreover, the CV and GCD confirm a wider voltage window as in Fig. 15(c). The CV profiles conducted for TSSC at various scan rates from 10 to 60 mV s^{-1} are presented in Fig. 15(d). The CV profiles have a quasi-rectangular behavior, indicating the pseudocapacitive nature of the material. The stable shape of the CV profile demonstrates high reversibility of the device. The GCD analysis was carried out at various current densities from 0.5 to 1.2 mA cm^{-2} at 1 V, and the results are presented in Fig. 15(e). The GCD profiles indicate that at low current densities, Li$^+$ ions have sufficient time to diffuse into the active material, facilitating efficient ion transport. The areal capacitance values drawn at various current densities are presented in Fig. 15(f). The maximum areal capacitance was 13.25 mF cm^{-2} at 0.5 mA cm^{-2} with an excellent rate capability of 61.73% for the fabricated TSSC device. This high performance of the V$_2$O$_5$/ZnO film makes it an appealing material for high-rate TSSC applications. The device shows excellent cycling stability for 6000 cycles at 1 mA cm^{-2} and demonstrates a capacity retention of 75.41% with a coulombic efficiency of 99%, as shown in Fig. 15(g). The device exhibit highest energy density of 0.46 μWh cm^{-2} at a power density of 62 μW cm^{-2} at 0.5 mA cm^{-2} and compared Ragone plot compared with previously reported literature data as shown in Fig. 15(h).

4.8. Summary statement of transition metal oxides

TMOs have emerged as highly promising electrode materials for supercapacitors due to their high specific capacitance, multiple accessible oxidation states, and reversible faradaic redox reactions. Among them, RuO$_2$ remains a benchmark pseudocapacitive material because of its excellent conductivity and rapid charge transfer, though its high cost limits its large-scale applications. The cost-effective alternatives such as RuO$_2$, ZnO, NiO, Co$_3$O$_4$, MnO$_2$, Fe$_2$O$_3$/Fe$_3$O$_4$ and V$_2$O$_5$ offer rich redox chemistry and structural versatility. Their multivalent transitions enable high charge storage capacity, while layered or

Table 2 Performance of various metal oxide-based electrode materials for supercapacitors

Electrode material	Synthesis method	Electrolyte	Specific capacitance (F g^{-1})	Energy density (Wh kg^{-1})	Power density (W kg^{-1})	Ref.
ZnO@S-CNF	Electrospinning technique	6 M KOH	209	11.2	900	269
TiN–ZnO composite	Wet chemical method	3 M KOH	469	19.83	6298.2	270
SnO$_2$–ZnO heterostructure	Atomic layer deposition	1 M KOH	538.90	14.8	2512.35	271
ZnO-QDs@NF//AC@NF	Hydrothermal	3 M KOH	118	39.58	7431	272
ZnO/MnTe	Hydrothermal	2 M KOH	1461	54	267	273
Na-doped MoS$_2$@NiO/C nanocomposites	Solvothermal approach	2 M KOH	2540.63	36.93	—	274
Ag/NiO	WSLE-mediated		872	46	3501	275
NiO@C	One-pot hydrothermal	1 M KOH	1360	21.6	4574	276
Co$_3$O$_4$/NiO nanospherical composite	Co-precipitation	2 M KOH	2769.2	131.96	3629.76	277
NiO/ACNFs-600	Atomic layer deposition	6 M KOH	870	39.85	2000	278
rGO‖Co$_3$O$_4$/Ag/rGO	Hydrothermal	1 M KOH	438	38.9	640	279
Ag-doped Co$_3$O$_4$ NPs	Co-precipitation	0.1 M KOH	992	27.9	3816.1	280
Co$_3$O$_4$ NPs	Hydrothermal	3 M KOH	870.6	77.3	1997.7	281
MnTiO$_3$/Co$_3$O$_4$ nanocomposite	Ultrasonication technique	2 M KOH	1534.67	64.05	274.1	282
rGO@Co$_3$O$_4$	Liquid-phase plasma electrolysis	6 M KOH	72.3	23.6	0.4	283
Alpha-Fe$_2$O$_3$	Decomposition method	6 mol L^{-1} KOH	149.3	4.20	224.90	284
In$_2$O$_3$/Fe$_2$O$_3$ nanocomposite	Hydrothermal	—	1564.9	356.6	0.3375	285
Ru: Fe$_2$O$_3$ nanocomposite	Successive Ionic Layer Adsorption and Reaction (SILAR)	1 M KOH	854.1	82.6	800	286
Mn: α-Fe$_2$O$_3$ nanostructured thin films	Spray pyrolysis	1 M Na$_2$SO$_4$	688.6	6	12 000	287
3D/2D/2D-α-Fe$_2$O$_3$/r-GO/GCN composite	Sono-chemical techniques	6 M KOH	810	40	929	288
Au–V$_2$O$_5$–MnO$_2$	Hydrothermal	1 M KOH and 0.5 M Na$_2$SO$_4$	388	49	4000	289
PANi/V$_2$O$_5$	Polymerisation method	1 M H$_2$SO$_4$	260	36	1000	290
V$_2$O$_5$–PEG/FSSM	R-CBD method	1 M LiClO$_4$	81.7	16.3	—	291
V$_2$O$_5$/h-BN nanoparticles	Hydrothermal	1 M KCl	408	25	2373	154
V$_2$O$_5$//f-CNT	Hydrothermal	1 M Na$_2$SO$_4$	104.4	37.12	800	292
MnO$_2$ nanostructures	Hydrothermal	1 mol L^{-1} Na$_2$SO$_4$	348.2	43.3	—	293
PPy/PANI/MnO$_2$	Chemical oxidative polymerization	1 M Na$_2$SO$_4$	181.5	36.1	2000	294
MnO$_2$/CuO/ZrO$_2$	Hydrothermal	1 M KOH	869.76	213.09	3830	295
ZnS/MnO$_2$	Hydrothermal	2 M KOH	373	15.45	—	296
rGO/RuO$_2$/PVA-H$_2$SO$_4$/WO$_3$	SILAR	1 M H$_2$SO$_4$	114	23	613	297
RuO$_2$ thin films	Ultrasonic spray pyrolysis technique	0.5 M H$_2$SO$_4$	1889	65.27	99.66	298
1D-RuO$_2$/C//AC	Thermal method	2 M KOH	53	16.71	751.66	299
SnO$_2$–RuO$_2$//SnO$_2$–RuO$_2$	Pulse layer deposition (PLD)	1 M KOH	70	19.05	645	300

spinel structures further enhance ion intercalation and electrochemical activity.

The electrochemical performance of TMO-based electrodes can be significantly improved through nanostructuring, hierarchical design, and hybridization with conductive carbon matrices. These strategies increase the active surface area, reduce ion diffusion pathways, and enhance electrical conductivity, thereby improving the rate capability and cycling stability. Although challenges such as low intrinsic conductivity, structural degradation, and scalability persist, rational material design and composite engineering continue to advance TMO-based supercapacitors. By integrating the intrinsic pseudocapacitive behavior with advanced nano-architectures, TMOs remain central to the development of high-energy-density, high-power-density, and sustainable next-generation energy storage systems (Table 2).

5. Techno-economic analysis and application outlook

Supercapacitors have emerged as a promising energy storage technology due to their high power density, rapid charge–discharge capability, long cycle life, and environmental compatibility. Extensive research has focused on improving electrode materials, ranging from 2D materials such as graphenes, MXenes, and TMDs to TMOs like MnO_2, Co_3O_4, and RuO_2. However, translating these material-level advancements into commercially viable devices requires careful techno-economic evaluation, with a particular emphasis on material cost and scalability. Although RuO_2 delivers exceptional pseudocapacitive performance, its high cost and limited availability restrict large-scale industrial adoption. In contrast, MnO_2, Co_3O_4, and iron oxides are abundant, inexpensive, and more suitable for practical deployment. Similarly, carbon-based 2D materials such as graphenes and CNTs provide outstanding electrochemical properties but their relatively high production costs and complex synthesis routes remain significant barriers. Emerging materials like MXenes and TMDs show remarkable promises for high-rate applications; nevertheless, their etching and exfoliation-based synthesis processes are often energy- and time-intensive, raising concerns about scalability and economic feasibility.[301,302]

The device fabrication and manufacturing complexity further influences the techno-economic viability of supercapacitors. The hybrid and composite electrodes that integrate 2D materials with metal oxides frequently exhibit enhanced electrochemical performance due to synergistic effects, yet their preparation often involves multi-step synthesis, strict morphological control, and uniform material dispersion, all of which increase the production costs. To address these challenges, scalable fabrication techniques like template-assisted synthesis, spray coating, and 3D printing are being investigated to facilitate the transition from laboratory-scale prototypes to industrial manufacturing. A key techno-economic consideration is the performance *versus* cost trade-off; materials offering the highest specific capacitance or energy density are not always the most economical option.[303,304] In terms of application prospects, supercapacitors are highly versatile and suitable for electric and hybrid vehicles, regenerative braking systems, portable electronics, wearable devices, and flexible energy storage platforms. Moreover, grid-level energy storage and renewable energy integration create opportunities for hybrid supercapacitors with improved energy density. By tailoring composite electrodes that combine 2D materials with TMOs or conductive materials, it is possible to achieve both high power output and moderate energy storage, thereby advancing supercapacitors toward commercially competitive and application-specific energy solutions.[305,306]

6. Conclusion and future perspectives

Supercapacitors are high demanding energy storage devices that offer high power density, excellent stability, fast charge–discharge, and environmental friendliness. The choice of electrode materials has a crucial impact on their storage performance. This review presents a comprehensive overview on the recent developments in supercapacitor research by covering the design of electrode materials and advancements in novel materials. The recent developments in EDLCs, hybrid supercapacitors, and pseudocapacitors, with particular focus on electrode materials, are discussed. The recent progresses of 2D materials and TMOs including RuO_2, ZnO, NiO, Co_3O_4, MnO_2, Fe_2O_3, Fe_3O_4, and V_2O_5 which have both redox properties and high energy density, are presented. However, their low conductivity hampers their widespread applications. Despite the significant advancements in the energy storage field, many challenges like scalability, cost-effectiveness, and the need for excellent cycling stability persist. Therefore, future research should be directed towards the novel development of hybrid electrode architectures to improve the efficiency and practical application of supercapacitors. Overcoming these challenges will enable supercapacitors to significantly contribute to next-generation energy storage in portable electronics, hybrid vehicles, and renewable energy applications.

The recent developments in supercapacitor technology by the integration of various electrode materials have brought a revolution towards sustainable and scalable energy storage systems. However, considerable challenges need to be addressed for its practical applications.

● The key direction is the rational design of hybrid electrode materials that combine the merits of EDLC and pseudocapacitance. This can be achieved through the modification of the structural and surface chemistry of 2D materials.[307–309] These modifications facilitate efficient ion diffusion and improve interfacial conductivity.

● The development of scalable, high-performance electrode materials such as metal oxides and carbon-based materials remains a key challenge. Current lab-scale methods are often complex and environmentally unfriendly, limiting large-scale production. Future research should focus on cost-effective,

green, and efficient synthesis techniques with controlled morphology, high surface area, and high electrochemical performance for practical applications.

• Interface engineering is a key strategy for enhancing the performance of supercapacitors and batteries by improving the electron transport, ion diffusion, and reaction kinetics. Materials with tunable porosity and electroactive surfaces can boost ion transport and active site availability. Future research should focus on scalable strategies like surface functionalization, heterostructures, and core–shell designs to develop next-generation electrodes with high capacitance, fast charge–discharge rates, and long cycle life.

• The rise of flexible and wearable electronics demands energy storage materials with high capacity, mechanical flexibility, and durability. Future research should focus on flexible, nanostructured, composite, and polymer-based electrodes that maintain performance under stress, while offering high energy density, lightweight design, and fast charge–discharge.

• Lastly, an in-depth understanding of the charge storage mechanism is essential for future designs, which can be achieved by employing *in situ* and operando techniques. The combination of computational modelling with experimental insights can bring a huge difference in the development of new electrode materials.

Conflicts of interest

There are no conflicts to declare.

Data availability

This review article is based on previously published data that are publicly available and properly cited throughout the manuscript. No new datasets were generated or analyzed.

Acknowledgements

References

1 Y. A. Kumar, N. Roy, T. Ramachandran, M. A. Assiri, S. S. Rao, M. Moniruzzaman and S. W. Joo, *Dalton Trans.*, 2024, **53**, 12410–12433.

2 R. Genc, *Sci. Rep.*, 2017, **7**, 11222.

3 S. Repp, E. Harputlu, S. Gurgen, M. Castellano, N. Kremer, N. Pompe, J. Wörner, A. Hoffmann, R. Thomann and F. M. Emen, *Nanoscale*, 2018, **10**, 1877–1884.

4 F. S. Oztuna, O. Unal, E. Erdem, H. Y. Acar and U. Unal, *J. Phys. Chem. C*, 2019, **123**, 3393–3401.

5 S. Zaman, Y. Q. Su, C. L. Dong, R. Qi, L. Huang, Y. Qin, Y. C. Huang, F. M. Li, B. You and W. Guo, *Angew. Chem., Int. Ed.*, 2022, **61**, e202115835.

6 T. Ramachandran, R. M. N. Kalla, Y. A. Kumar, A. Ghosh, A. G. Al-Sehemi, R. Khan and J. Lee, *J. Alloys Compd.*, 2025, 182500.

7 N. J. De Klerk, E. Van Der Maas and M. Wagemaker, *ACS Appl. Energy Mater.*, 2018, **1**, 3230–3242.

8 S. J. Kwon, T. Kim, B. M. Jung, S. B. Lee and U. H. Choi, *ACS Appl. Mater. Interfaces*, 2018, **10**, 35108–35117.

9 B. Anothumakkool, A. Torris AT, S. Veeliyath, V. Vijayakumar, M. V. Badiger and S. Kurungot, *ACS Appl. Mater. Interfaces*, 2016, **8**, 1233–1241.

10 S. Zaman, M. Khalid and S. Shahgaldi, *ACS Energy Lett.*, 2024, **9**, 2922–2935.

11 A. M. Bogale, T. Ramachandran, L. T. Tufa, B. B. Badassa, M. E. Suk, R. Pitcheri, J. Lee, S. K. Jilcha, A. Y. Tiky and B. A. Zenebe, *Mater. Sci. Semicond. Process.*, 2025, **200**, 109958.

12 M. D. Stoller, S. Park, Y. Zhu, J. An and R. S. Ruoff, *Nano Lett.*, 2008, **8**, 3498–3502.

13 M. S. Halper and J. C. Ellenbogen, *The MITRE Corporation*, McLean, Virginia, USA, 2006, p. 1.

14 M. Ho, P. S. Khiew, D. Isa, T. Tan, W. S. Chiu and C. H. Chia, *Nano*, 2014, **9**, 1430002.

15 M. Ahmad, A. Inayat, M. N. Hussain, A. Khan, M. Alam, M. Sultan and S. M. Abbas, *Mater. Today Sustain.*, 2024, **25**, 100631.

16 Q. Li, *Small*, 2021, **17**, 2101617.

17 Q. Li, Q. Zhang, J. Sun, C. Liu, J. Guo, B. He, Z. Zhou, P. Man, C. Li and L. Xie, *Adv. Sci.*, 2019, **6**, 1801379.

18 H. D. Yoo, S.-D. Han, R. D. Bayliss, A. A. Gewirth, B. Genorio, N. N. Rajput, K. A. Persson, A. K. Burrell and J. Cabana, *ACS Appl. Mater. Interfaces*, 2016, **8**, 30853–30862.

19 Q. Li, Q. Zhang, C. Liu, W. Gong, Z. Zhou, P. Man, J. Guo, B. He, K. Zhang, W. Lu and Y. Yao, *Energy Storage Mater.*, 2020, **27**, 316–326.

20 H. Gao, F. Xiao, C. B. Ching and H. Duan, *ACS Appl. Mater. Interfaces*, 2012, **4**, 2801–2810.

21 A. M. Bogale, T. Ramachandran, M. E. Suk, B. B. Badassa, M. M. Solomon, J. He, A. Yusuf, R. K. Raji, B. A. Zenebe and N. K. Amare, *J. Phys. Chem. Solids*, 2025, 113079.

22 M. N. Hussain, S. G. Hickey and S. M. Shah, *Nanoscience*, 2025, 226–253.

23 M. Zhi, C. Xiang, J. Li, M. Li and N. Wu, *Nanoscale*, 2013, **5**, 72–88.

24 A. Ghosh, E. J. Ra, M. Jin, H. K. Jeong, T. H. Kim, C. Biswas and Y. H. Lee, *Adv. Funct. Mater.*, 2011, **21**, 2541–2547.

25 M. Zhi, A. Manivannan, F. Meng and N. Wu, *J. Power Sources*, 2012, **208**, 345–353.

26 D. P. Dubal, O. Ayyad, V. Ruiz and P. Gomez-Romero, *Chem. Soc. Rev.*, 2015, **44**, 1777–1790.

27 K. Wang, Z. Wang, C. Wang, X. Zhang and L. Wu, *J. Energy Storage*, 2024, **98**, 113129.

28 S. Reenu, L. Phor, A. Kumar and S. Chahal, *J. Energy Storage*, 2024, **84**, 110698.

29 E. Vessally, R. M. Rzayev, A. A. Niyazova, T. Aggarwal and K. E. Rahimova, *RSC Adv.*, 2024, **14**, 40141–40159.

30 S. Kota, B. Divya, N. S. Acharya, S. P. Kumar and R. Annapragada, *Discovery Electron.*, 2026, **3**, 12.

31 S. Jayakumar, P. C. Santhosh, M. M. Mohideen and A. V. Radhamani, *J. Alloys Compd.*, 2024, **976**, 173170.

32 A. Shen, Z. Shi, C. Zhao, W. Zhang, Y. Feng, W. Gong, C. Liu, P. Xue, P. Xu and Q. Li, *J. Colloid Interface Sci.*, 2025, **685**, 615–625.

33 J. Fu, A. Shen, W. Zhang, Y. Feng, W. Gong, H. Fu, Z. Yong and Q. Li, *Mater. Today Energy*, 2025, **48**, 101815.

34 M. N. Hussain, A. Naveed, M. Sohail, M. D. Khan, S. G. Hickey, N. Ullah, I. Ahmad, A. Haider and S. M. Shah, *ACS Appl. Eng. Mater.*, 2025, **3**, 1315–1326.

35 M. N. Hussain, A. Inayat, S. M. Shah, M. Ihsun, A. Haider, S. M. Abbas and S. G. Hickey, *Nanoscale*, 2025, **17**, 25846–25858.

36 L. Sun, Y. Dong, H. Li, H. Meng, J. Liu, Q. Cao and C. Pan, *Batteries*, 2024, **10**, 395.

37 C. V. V. M. Gopi, S. Alzahmi, M. Y. Al-Haik, Y. A. Kumar, F. Hamed, Y. Haik and I. M. Obaidat, *Mater. Today Sustainable*, 2024, **28**, 100981.

38 F. Ran, M. Hu, S. Deng, K. Wang, W. Sun, H. Peng and J. Liu, *RSC Adv.*, 2024, **14**, 11482–11512.

39 J. P. Das, V. Navakoteswara Rao and S.-J. Kim, *Prog. Mater. Sci.*, 2026, **157**, 101599.

40 Y. Wang, J. Wu, J. Dong, X. Xu, H. Song, L. Yuan, X. Li and Z. Lu, *Chem. Sci.*, 2025, **16**, 22565–22579.

41 Y.-M. Wei, K. D. Kumar, L. Zhang and J.-F. Li, *Front. Chem.*, 2025, **13**, 1636683.

42 S. J and U. R. M, *Results Eng.*, 2026, **29**, 108720.

43 S. Kong, Y. Li, X. Zhang, Z. Xu, X. Wang, Y. Feng, W. Gong, C. Liu, K. Tian and Q. Li, *Small*, 2023, **19**, 2304462.

44 Q. Li, S. Jing, Z. Yong, Q. Zhang, C. Liu, K. Zhu, Y. Feng, W. Gong and Y. Yao, *Energy Storage Mater.*, 2021, **42**, 815–825.

45 H. Sun, Z. Xu and C. Gao, *Adv. Mater.*, 2013, **25**, 2554–2560.

46 Y. A. Kumar, J. K. Alagarasan, T. Ramachandran, M. D. Rezeq, M. A. Bajaber, A. A. Alalwiat, M. Moniruzzaman and M. Lee, *J. Energy Storage*, 2024, **86**, 111119.

47 M. Worsley and T. Baumann, *Handbook of Sol-Gel Science and Technology*, Search PubMed, 2018, pp. 3339–3374.

48 Y. Hu, H. Zhuo, Z. Chen, K. Wu, Q. Luo, Q. Liu, S. Jing, C. Liu, L. Zhong and R. Sun, *ACS Appl. Mater. Interfaces*, 2018, **10**, 40641–40650.

49 C. Moreno-Castilla and F. Maldonado-Hódar, *Carbon*, 2005, **43**, 455–465.

50 H. Choi, V. G. Parale, T. Kim, J. Kim, S. Bhosale, S.-H. Kim, V. D. Phadtare, Y. Kim, W. Lee, M. G. Mali, S. S. Sutar, T. Dongale, S. E. Shim and H.-H. Park, *Energy*, 2026, **347**, 140404.

51 Y. Al Haj, A. B. Soliman, J. Vapaavuori and M. Elbahri, *Adv. Funct. Mater.*, 2024, **34**, 2313117.

52 M. Winter and R. J. Brodd, *Chem. Rev.*, 2004, **104**, 4245–4270.

53 A. Muzaffar, M. B. Ahamed, K. Deshmukh and J. Thirumalai, *Renewable Sustainable Energy Rev.*, 2019, **101**, 123–145.

54 X. Zhang, H. Zhang, C. Li, K. Wang, X. Sun and Y. Ma, *RSC Adv.*, 2014, **4**, 45862–45884.

55 A. Yu, I. Roes, A. Davies and Z. Chen, *Appl. Phys. Lett.*, 2010, **96**, 253105.

56 X. Cao, Y. Shi, W. Shi, G. Lu, X. Huang, Q. Yan, Q. Zhang and H. Zhang, *Small*, 2011, **7**, 3163–3168.

57 J. Wang, F. Ma and M. Sun, *RSC Adv.*, 2017, **7**, 16801–16822.

58 T. Palaniselvam and J.-B. Baek, *2D Mater.*, 2015, **2**, 032002.

59 Y. Han, Y. Ge, Y. Chao, C. Wang and G. G. Wallace, *J. Energy Chem.*, 2018, **27**, 57–72.

60 Y. Shao, M. F. El-Kady, L. J. Wang, Q. Zhang, Y. Li, H. Wang, M. F. Mousavi and R. B. Kaner, *Chem. Soc. Rev.*, 2015, **44**, 3639–3665.

61 M. N. Hussain, A. Inayat, R. Ansir, A. Naveed, S. M. Abbas, A. Haider and S. M. Shah, *Energy Technol.*, 2024, **12**, 2300854.

62 Z. Tai, X. Yan and Q. Xue, *J. Power Sources*, 2012, **213**, 350–357.

63 H. Wang, C. Shen, J. Liu, W. Zhang and S. Yao, *J. Alloys Compd.*, 2019, **792**, 122–129.

64 S. Rajeevan, S. John, D. Ponnamma and S. C. George, *J. Power Sources*, 2026, **661**, 238622.

65 T. Akhter, M. M. Islam, S. N. Faisal, E. Haque, A. I. Minett, H. K. Liu, K. Konstantinov and S. X. Dou, *ACS Appl. Mater. Interfaces*, 2016, **8**, 2078–2087.

66 K. V. C. Mouli, D. Mani, T. Ramachandran, Y. A. Kumar, A. Ghosh, P. Somu and R. Mangiri, *Mater. Chem. Phys.*, 2025, 131660.

67 Y. Shao, M. F. El-Kady, L. J. Wang, Q. Zhang, Y. Li, H. Wang, M. F. Mousavi and R. B. Kaner, *Chem. Soc. Rev.*, 2015, **44**, 3639–3665.

68 Q. Ke and J. Wang, *J. Materiomics*, 2016, **2**, 37–54.

69 J. N. Coleman, U. Khan, W. J. Blau and Y. K. Gun'ko, *Carbon*, 2006, **44**, 1624–1652.

70 A. Zheng, C. Tao, J. Guo, Z. Shi, X. Cao, Z. Zhang and X. Yang, *Chem. Eng. J.*, 2025, **516**, 164116.

71 Y. Anil Kumar, G. Koyyada, T. Ramachandran, J. H. Kim, S. Sajid, M. Moniruzzaman, S. Alzahmi and I. M. Obaidat, *Nanomaterials*, 2023, **13**, 1049.

72 Y. Jang, J. Jo, H. Jang, I. Kim, D. Kang and K.-Y. Kim, *Appl. Phys. Lett.*, 2014, **104**, 243901.

73 N. Shimodaira and A. Masui, *J. Appl. Phys.*, 2002, **92**, 902–909.

74 R. Heimböckel, F. Hoffmann and M. Fröba, *Phys. Chem. Chem. Phys.*, 2019, **21**, 3122–3133.

75 S. Zaman, M. Wang, H. Liu, F. Sun, Y. Yu, J. Shui, M. Chen and H. Wang, *Trends Chem.*, 2022, **4**, 886–906.

76 C. Masarapu, L. P. Wang, X. Li and B. Wei, *Adv. Energy Mater.*, 2012, **2**, 546–552.

77 A. Kattainen, C. Mevada, T. Punkari, V. S. Parihar, H. Pourkheirollah, J. Keskinen and M. Mäntysalo, *J. Power Sources*, 2026, **661**, 238663.

78 A. Jain, M. Ghosh, M. Krajewski, S. Kurungot and M. Michalska, *J. Energy Storage*, 2021, **34**, 102178.

79 M. Hu, H. Zhang, T. Hu, B. Fan, X. Wang and Z. Li, *Chem. Soc. Rev.*, 2020, **49**, 6666–6693.

80 S. Venkateshalu and A. N. Grace, *Appl. Mater. Today*, 2020, **18**, 100509.

81 Y. Tian, C. Yang, Y. Luo, H. Zhao, Y. Du, L. B. Kong and W. Que, *ACS Appl. Energy Mater.*, 2020, **3**, 5006–5014.

82 P. Forouzandeh and S. C. Pillai, *Mater. Today Proc.*, 2021, **41**, 498–505.

83 B. Kirubasankar, M. Narayanasamy, J. Yang, M. Han, W. Zhu, Y. Su, S. Angaiah and C. Yan, *Appl. Surf. Sci.*, 2020, **534**, 147644.

84 R. Garg, A. Agarwal and M. Agarwal, *Mater. Res. Express.*, 2020, **7**, 022001.

85 S. Venkateshalu and A. N. Grace, *Appl. Mater. Today*, 2020, **18**, 100509.

86 Y. Li, C. Pan, P. Kamdem and X.-J. Jin, *Energy Fuels*, 2020, **34**, 10120–10130.

87 M. Naguib, O. Mashtalir, J. Carle, V. Presser, J. Lu, L. Hultman, Y. Gogotsi and M. W. Barsoum, *ACS Nano*, 2012, **6**, 1322–1331.

88 M. Ghidiu, M. R. Lukatskaya, M.-Q. Zhao, Y. Gogotsi and M. W. Barsoum, *Nature*, 2014, **516**, 78–81.

89 Y. Dall'Agnese, M. R. Lukatskaya, K. M. Cook, P.-L. Taberna, Y. Gogotsi and P. Simon, *Electrochem. Commun.*, 2014, **48**, 118–122.

90 J. Li, X. Yuan, C. Lin, Y. Yang, L. Xu, X. Du, J. Xie, J. Lin and J. Sun, *Adv. Energy Mater.*, 2017, **7**, 1602725.

91 I. Ayman, A. Rasheed, S. Ajmal, A. Rehman, A. Ali, I. Shakir and M. F. Warsi, *Energy Fuels*, 2020, **34**, 7622–7630.

92 Y. Guo, L. Zhang, Y. Zhou and J. Sun, *ACS Appl. Energy Mater.*, 2026, **9**, 2110–2120.

93 J. Fu, J. Yun, S. Wu, L. Li, L. Yu and K. H. Kim, *ACS Appl. Mater. Interfaces*, 2018, **10**, 34212–34221.

94 R. Khan, R. M. N. Kalla, T. Ramachandran, A. G. Al-Sehemi, Y. A. Kumar, P. Somu and J. Lee, *J. Alloys Compd.*, 2025, 182874.

95 A. K. Geim and I. V. Grigorieva, *Nature*, 2013, **499**, 419–425.

96 K. S. Novoselov, A. Mishchenko, A. Carvalho and A. Castro Neto, *Science*, 2016, **353**, aac9439.

97 T. Cao, J. Feng, J. Shi, Q. Niu and E. Wang, *arXiv*, 2011, preprint, arXiv:1112.4013, DOI: 10.48550/arXiv.1112.4013.

98 B. Radisavljevic, A. Radenovic, J. Brivio, V. Giacometti and A. Kis, *Nat. Nanotechnol.*, 2011, **6**, 147–150.

99 S. Alam, A. Jan, M. Z. Iqbal, I. S. Yahia, H. H. Hegazy and M. I. Saleem, *Mater. Chem. Phys.*, 2025, **334**, 130444.

100 S. Mishra, P. K. Maurya and A. K. Mishra, *Mater. Chem. Phys.*, 2020, **255**, 123551.

101 J. Wang, Z. Wu, K. Hu, X. Chen and H. Yin, *J. Alloys Compd.*, 2015, **619**, 38–43.

102 S. Ratha and C. S. Rout, *ACS Appl. Mater. Interfaces*, 2013, **5**, 11427–11433.

103 C.-C. Tu, L.-Y. Lin, B.-C. Xiao and Y.-S. Chen, *J. Power Sources*, 2016, **320**, 78–85.

104 T. W. Lin, T. Sadhasivam, A. Y. Wang, T. Y. Chen, J. Y. Lin and L. D. Shao, *ChemElectroChem*, 2018, **5**, 1024–1031.

105 M. Sakthivel, S. Ramaraj, S.-M. Chen, T.-W. Chen and K.-C. Ho, *ACS Appl. Mater. Interfaces*, 2019, **11**, 18483–18493.

106 Z. Chang, X. Ju, P. Guo, X. Zhu, C. Liao, Y. Zong, X. Li and X. Zheng, *J. Alloys Compd.*, 2020, **824**, 153873.

107 S. Liu, Y. Yin, M. Wu, K. S. Hui, K. N. Hui, C. Y. Ouyang and S. C. Jun, *Small*, 2019, **15**, 1803984.

108 S. Saha, M. Jana, P. Samanta, N. C. Murmu, N. H. Kim, T. Kuila and J. H. Lee, *Mater. Chem. Phys.*, 2017, **190**, 153–165.

109 G. Bhimanapati, N. Glavin and J. A. Robinson, *Semiconductors and semimetals*, Elsevier, 2016, vol. 95, pp. 101–147.

110 S. S. Karade, D. P. Dubal and B. R. Sankapal, *RSC Adv.*, 2016, **6**, 39159–39165.

111 T. Li, X. Jiao, T. You, F. Dai, P. Zhang, F. Yu, L. Hu, L. Ding, L. Zhang and Z. Wen, *Ceram. Int.*, 2019, **45**, 4283–4289.

112 S. Zaman, L. Huang, A. I. Douka, H. Yang, B. You and B. Y. Xia, *Angew. Chem.*, 2021, **133**, 17976–17996.

113 S. Saha, M. Jana, P. Samanta, N. C. Murmu, N. H. Kim, T. Kuila and J. H. Lee, *Mater. Chem. Phys.*, 2017, **190**, 153–165.

114 I. M. Patil, S. Kapse, H. Parse, R. Thapa, G. Andersson and B. Kakade, *J. Power Sources*, 2020, **479**, 229092.

115 X. Zheng, G. Wang, F. Huang, H. Liu, C. Gong, S. Wen, Y. Hu, G. Zheng and D. Chen, *Front. Chem.*, 2019, **7**, 544.

116 B. S. Chikkatti, M. M. Momin, A. M. Sajjan, N. R. Banapurmath, T. M. Y. Khan and A. S. Shaik, *Diamond Relat. Mater.*, 2025, **159**, 112874.

117 D. Krishnamoorthy and A. K. Singh, *Energy Fuels*, 2024, **38**, 21468–21481.

118 G. Zhao, Y. Cheng, Y. Wu, X. Xu and X. Hao, *Small*, 2018, **14**, 1704138.

119 Y. Wang, L. Liu, T. Ma, Y. Zhang and H. Huang, *Adv. Funct. Mater.*, 2021, **31**, 2102540.

120 M. Ghaemmaghami and R. Mohammadi, *Sustainable Energy Fuels*, 2019, **3**, 2176–2204.

121 Y. Luo, Y. Yan, S. Zheng, H. Xue and H. Pang, *J. Mater. Chem.*, 2019, **7**, 901–924.

122 Y. Luo, Y. Yan, S. Zheng, H. Xue and H. Pang, *J. Mater. Chem. A*, 2019, **7**, 901–924.

123 R. R. Nallapureddy, M. R. Pallavolu and S. W. Joo, *Energy Fuels*, 2021, **35**, 1796–1809.

124 C. Shen, R. Li, L. Yan, Y. Shi, H. Guo, J. Zhang, Y. Lin, Z. Zhang, Y. Gong and L. Niu, *Appl. Surf. Sci.*, 2018, **455**, 841–848.

125 M. Tahir, C. Cao, F. K. Butt, F. Idrees, N. Mahmood, Z. Ali, I. Aslam, M. Tanveer, M. Rizwan and T. Mahmood, *J. Mater. Chem. A*, 2013, **1**, 13949–13955.

126 M. Tahir, C. Cao, N. Mahmood, F. K. Butt, A. Mahmood, F. Idrees, S. Hussain, M. Tanveer, Z. Ali and I. Aslam, *ACS Appl. Mater. Interfaces*, 2014, **6**, 1258–1265.

127 R. Gonçalves, T. M. Lima, M. W. Paixão and E. C. Pereira, *RSC Adv.*, 2018, **8**, 35327–35336.

128 M. Sharma and A. Gaur, *Sci. Rep.*, 2020, **10**, 2035.

129 Y. Xu, L. Wang, Y. Zhou, J. Guo, S. Zhang and Y. Lu, *J. Electroanal. Chem.*, 2019, **852**, 113507.

130 G. Dong, H. Fan, K. Fu, L. Ma, S. Zhang, M. Zhang, J. Ma and W. Wang, *Composites, Part B*, 2019, **162**, 369–377.

131 S. Zaman and S. Chen, *J. Catal.*, 2023, **421**, 221–227.

132 Manisha, M. Dhanda, V. Panwar, S. Lata, H. Kumar and A. Sharma, *J. Energy Storage*, 2025, **106**, 114698.

133 E. Elanthamilan and S.-F. Wang, *Batteries Supercaps*, 2025, e202400754.

134 M. Sivakumar, B. Muthukutty, G. Panomsuwan, V. Veeramani, Z. Jiang and T. Maiyalagan, *Colloids Surf., A*, 2022, **648**, 129188.

135 J. Zhu, Q. Zhang, Y. Zhao, R. Zhang, L. Liu and J. Yu, *Chem. Eng. J.*, 2022, **434**, 134662.

136 T. Nandagopal, G. Balaji and S. Vadivel, *J. Energy Storage*, 2023, **68**, 107710.

137 N. Dywili, A. Ntziouni, M. M. Ndipingwi, C. Ikpo, A. C. Nwanya, K. Kordatos and E. Iwuoha, *Mater. Today Commun.*, 2023, **35**, 105653.

138 O. Eksik, M. B. Arvas and R. Yavuz, *J. Mater. Sci.: Mater. Electron.*, 2023, **34**, 1831.

139 G. Wang, N. Jiang, Y. Xu, Z. Zhang, G. Wang and K. Cheng, *J. Colloid Interface Sci.*, 2023, **630**, 817–827.

140 M. M. Rahman, M. R. Shawon, M. H. Rahman, I. Alam, M. O. Faruk, M. M. R. Khan and O. Okoli, *J. Energy Storage*, 2023, **67**, 107615.

141 A. Baby, S. Sunny, J. Vigneshwaran, S. Abraham, S. P. Jose, W. S. Saeed, M. R. Pallavolu, J. Cherusseri and S. Puthenveetil Balakrishnan, *ACS Appl. Energy Mater.*, 2023, **6**, 10442–10456.

142 F. Niaz, S. S. Shah, K. Hayat, M. A. Aziz, G. Liu, Y. Iqbal and M. Oyama, *Ind. Crops Prod.*, 2024, **219**, 119161.

143 N. Chaiammart, V. Vignesh, M. M. Thu, A. Eiad-ua, T. Maiyalagan and G. Panomsuwan, *Carbon Resour. Convers.*, 2024, 100267.

144 N. An, W. Li, Z. Shao, L. Zhou, Y. He, D. Sun, X. Dong and Z. Hu, *J. Energy Storage*, 2023, **57**, 106180.

145 Q. Tang, Y. Zhang, X. Zhu, Y. Wang, Z. Man, C. Yang, J. Xu, G. Wu and W. Lu, *Adv. Funct. Mater.*, 2024, **34**, 2410005.

146 S. Li, Q. Song, C. Fang, Y. Lu, X. Ding, T. Liu, J. Zhang and F. J. Xu, *Small*, 2025, **21**, 2409130.

147 Z. Pan, X. Li, C. Yang and X. Ji, *J. Colloid Interface Sci.*, 2023, **634**, 460–468.

148 V. V. Mohan, M. Mohan and R. Rakhi, *Surf. Interfaces*, 2023, **42**, 103496.

149 S. Hussain, D. Vikraman, Z. A. Sheikh, M. T. Mehran, F. Shahzad, K. M. Batoo, H.-S. Kim, D.-K. Kim, M. Ali and J. Jung, *Chem. Eng. J.*, 2023, **452**, 139523.

150 M. Abdullah, S. Khan, K. Jabbour, M. Imran, M. F. Ashiq, P. John, S. Manzoor, T. Munawar and M. N. Ashiq, *Electrochim. Acta*, 2023, **466**, 143020.

151 D. Zheng, G. He, Y. Mi, H. Huang Fu, Y. Li, H. Zhang, M. Wu and H. Yuan, *J. Mater. Sci.: Mater. Electron.*, 2023, **34**, 1734.

152 S. P. Lonkar, V. Gupta, S. M. Alhassan and A. Schiffer, *Energy Storage*, 2023, **5**, e416.

153 M. Sakaray and S. C. Chidurala, *Synth. Met.*, 2023, **298**, 117448.

154 V. Mounasamy, M. Keerthana and N. Ponpandian, *ACS Appl. Electron. Mater.*, 2024, **6**, 5681–5693.

155 C. S. Bongu, M. Arsalan and E. H. Alsharaeh, *ACS Omega*, 2024, **9**, 15294–15303.

156 M. M. Rahman, M. R. Hossen, I. Alam, M. H. Rahman, O. Faruk, M. Nurbas, M. M. Rahman and M. M. R. Khan, *J. Alloys Compd.*, 2023, **947**, 169471.

157 K. Lakshmanan, S. Chidambaram and S. Gurusamy, *ACS Appl. Electron. Mater.*, 2024, **6**, 5101–5116.

158 M. Devi, S. Yesmin, B. Das, S. S. Dhar and R. Dasgupta, *Energy Fuels*, 2023, **37**, 3247–3259.

159 M. Dhanda, R. Arora, A. S. Reddy, S. Lata and A. Sharma, *J. Alloys Compd.*, 2023, **955**, 169738.

160 A. L. M. Reddy and S. Ramaprabhu, *J. Phys. Chem. C*, 2007, **111**, 7727–7734.

161 M. N. Hussain, A. Naveed, A. Inayat, M. Bilal, A. Haider and S. M. Shah, *ChemistrySelect*, 2023, **8**, e202303224.

162 C. Choi, D. S. Ashby, D. M. Butts, R. H. DeBlock, Q. Wei, J. Lau and B. Dunn, *Nat. Rev. Mater.*, 2020, **5**, 5–19.

163 D. Majumdar, *Mater. Sci. Res. India*, 2018, **15**, 30–40.

164 D. Majumdar, T. Maiyalagan and Z. Jiang, *ChemElectroChem*, 2019, **6**, 4343–4372.

165 R. Chandrashekhar and A. A. Yadav, *Electrochim. Acta*, 2023, **437**, 141521.

166 Y. Xie and C. Yao, *Mater. Res. Express.*, 2020, **6**, 125550.

167 S. Korkmaz, İ. A. Kariper, O. Karaman and C. Karaman, *Ceram. Int.*, 2021, **47**, 34514–34520.

168 C. Bathula, I. Rabani, S. Ramesh, S.-H. Lee, R. R. Palem, A. T. A. Ahmed, H. S. Kim, Y.-S. Seo and H.-S. Kim, *J. Alloys Compd.*, 2021, **887**, 161307.

169 V. Vijayabala, N. Senthilkumar, K. Nehru and R. Karvembu, *J. Mater. Sci.: Mater. Electron.*, 2018, **29**, 323–330.

170 G. Xu, H. Yin, J. Zhang, F. Wang, N. Fukata and J. Tang, *J. Alloys Compd.*, 2025, **1036**, 182082.

171 S. Ramesh, K. Karuppasamy, A. Sivasamy, H.-S. Kim, H. Yadav and H. S. Kim, *J. Alloys Compd.*, 2021, **877**, 160297.

172 M.-Y. Chung and C.-T. Lo, *Electrochim. Acta*, 2020, **364**, 137324.

173 J. Zhao, F. Liu and W. Li, *Nanomaterials*, 2019, **9**, 377.

174 Q. Jiang, N. Kurra, M. Alhabeb, Y. Gogotsi and H. N. Alshareef, *Adv. Energy Mater.*, 2018, **8**, 1703043.

175 Y. Li, H. Gao, Z. Sun, Q. Li, Y. Xu, C. Ge and Y. Cao, *J. Solid State Electrochem.*, 2018, **22**, 3197–3207.

176 K. Subramani and M. Sathish, *Mater. Lett.*, 2019, **236**, 424–427.

177 Y.-N. Liu, L.-N. Jin, H.-T. Wang, X.-H. Kang and S.-W. Bian, *J. Colloid Interface Sci.*, 2018, **530**, 29–36.

178 B. Pant, M. Park, G. P. Ojha, J. Park, Y.-S. Kuk, E.-J. Lee, H.-Y. Kim and S.-J. Park, *J. Colloid Interface Sci.*, 2018, **522**, 40–47.

179 M. S. Yadav, N. Singh and S. M. Bobade, *Ionics*, 2018, **24**, 3611–3630.

180 W. K. Chee, H. N. Lim and N. M. Huang, *Int. J. Energy Res.*, 2015, **39**, 111–119.

181 Y. Haldorai, W. Voit and J.-J. Shim, *Electrochim. Acta*, 2014, **120**, 65–72.

182 G. Guo, L. Huang, Q. Chang, L. Ji, Y. Liu, Y. Xie, W. Shi and N. Jia, *Appl. Phys. Lett.*, 2011, **99**, 083111.

183 X. Xiao, B. Han, G. Chen, L. Wang and Y. Wang, *Sci. Rep.*, 2017, **1**, 40167.

184 M. Saranya, R. Ramachandran and F. Wang, *J. Sci.: Adv. Mater. Devices*, 2016, **1**, 454–460.

185 A. U. Ammar, M. H. Aleinawi, M. Stefan, A. Gungor, A. Popa, D. Toloman, K. Maškarić, E. Saritas, L. Barbu-Tudoran, S. Macavei, M. Senila, E. Erdem and A. M. Rostas, *Electrochim. Acta*, 2025, **519**, 145806.

186 C. J. Raj, M. Rajesh, R. Manikandan, J. Y. Sim, K. H. Yu, S. Y. Park, J. H. Song and B. C. Kim, *Electrochim. Acta*, 2017, **247**, 949–957.

187 K. S. Lee, C. W. Park and J.-D. Kim, *Colloids Surf., A*, 2018, **555**, 482–490.

188 C. H. Kim and B.-H. Kim, *J. Power Sources*, 2015, **274**, 512–520.

189 N. I. T. Ramli, S. A. Rashid, M. S. Mamat, Y. Sulaiman, S. A. Zobir and S. Krishnan, *Electrochim. Acta*, 2017, **228**, 259–267.

190 S. Yang, Z. Han, J. Sun, X. Yang, X. Hu, C. Li and B. Cao, *Electrochim. Acta*, 2018, **268**, 20–26.

191 X. Wang, F. Sun, F. Jiang, B. Diao, R. Wang, H. Li, S. W. Joo, R. Li, S. H. Kim and C. Cong, *Chem. Eng. J.*, 2024, **500**, 157211.

192 X. Liu and F. Liu, *Eur. J. Inorg. Chem.*, 2018, 987–991.

193 R. S. Kate, S. A. Khalate and R. J. Deokate, *J. Alloys Compd.*, 2018, **734**, 89–111.

194 S. Bhise, D. Awale, M. Vadiyar, S. Patil, U. Ghorpade, B. Kokare, J. Kim and S. Kolekar, *Bull. Mater. Sci.*, 2019, **42**, 263.

195 Z. Luo, L. Liu, X. Yang, X. Luo, P. Bi, Z. Fu, A. Pang, W. Li and Y. Yi, *ACS Appl. Mater. Interfaces*, 2020, **12**, 39098–39107.

196 P. Vickraman and B. J. Reddy, *J. Electroanal. Chem.*, 2018, **823**, 342–349.

197 Y. Han, S. Zhang, N. Shen, D. Li and X. Li, *Mater. Lett.*, 2017, **188**, 1–4.

198 V. Balaji, A. K. Bojarajan, R. R. Sasikaran, K. M. Eswari, D. K. Ponelakkia, R. Yuvakkumar and G. Ravi, *J. Alloys Compd.*, 2026, **1057**, 186747.

199 M. Zhang, T. Ma, Y. Wang, D. Pan and J. Xie, *J. Mater. Sci.: Mater. Electron.*, 2018, **29**, 6991–7001.

200 Y. Navale, S. Navale, I. Dhole, F. Stadler and V. Patil, *Org. Electron.*, 2018, **57**, 110–117.

201 C. Huang, C. Hao, W. Zheng, S. Zhou, L. Yang, X. Wang, C. Jiang and L. Zhu, *Appl. Surf. Sci.*, 2020, **505**, 144589.

202 X. Feng, Y. Huang, C. Li, X. Chen, S. Zhou, X. Gao and C. Chen, *Chem. Eng. J.*, 2019, **368**, 51–60.

203 U. K. Chime, A. C. Nkele, S. Ezugwu, A. C. Nwanya, N. Shinde, M. Kebede, P. M. Ejikeme, M. Maaza and F. I. Ezema, *Curr. Opin. Electrochem.*, 2020, **21**, 175–181.

204 Y. Zhao, D. Sun, G. Xing, M. Wei, J. Yang, X. Wang and D. Wang, *J. Appl. Phys.*, 2019, **126**, 015103.

205 F. Mashkoor, M. Shoeb, J. A. Khan, M. A. Gondal and C. Jeong, *J. Energy Storage*, 2024, **104**, 114578.

206 Y. Wang, A. Pan, Q. Zhu, Z. Nie, Y. Zhang, Y. Tang, S. Liang and G. Cao, *J. Power Sources*, 2014, 107–112.

207 X. Zhao, L. Mao, Q. Cheng, J. Li, F. Liao, G. Yang, L. Xie, C. Zhao and L. Chen, *Chem. Eng. J.*, 2020, **387**, 124081.

208 Z. Gao, C. Chen, J. Chang, L. Chen, D. Wu, F. Xu and K. Jiang, *Electrochim. Acta*, 2018, **260**, 932–943.

209 Z. Liu, W. Zhou, S. Wang, W. Du, H. Zhang, C. Ding, Y. Du and L. Zhu, *J. Alloys Compd.*, 2019, **774**, 137–144.

210 M. Chen, Q. Ge, M. Qi, X. Liang, F. Wang and Q. Chen, *Surf. Coat. Technol.*, 2019, **360**, 73–77.

211 X. Wang, N. Zhang, X. Chen, J. Liu, F. Lu, L. Chen and G. Shao, *Colloids Surf., A*, 2019, **570**, 63–72.

212 Y. Xu, Q. Ding, L. Li, Z. Xie and G. Jiang, *New J. Chem.*, 2018, **42**, 20069–20073.

213 L. Xuan, L. Chen, Q. Yang, W. Chen, X. Hou, Y. Jiang, Q. Zhang and Y. Yuan, *J. Mater. Chem. A*, 2015, **3**, 17525–17533.

214 A. Rashti, X. Lu, A. Dobson, E. Hassani, F. Feyzbar-Khalkhali-Nejad, K. He and T.-S. Oh, *ACS Appl. Energy Mater.*, 2021, **4**, 1537–1547.

215 W. Zhang, J. Duchet and J.-F. Gérard, *J. Colloid Interface Sci.*, 2014, **430**, 61–68.

216 M. J. Salethraj, G. D. Jeyaleela, D. Govindarajan, L. Guganathan, M. Abbas, S. Kalathil and A. Raja, *J. Mater. Sci.: Mater. Electron.*, 2026, **37**, 119.

217 X. Lv, W. Huang, J. Tang, L. Tang and Q. Shi, *Electrochim. Acta*, 2021, **380**, 138248.

218 J. Zhu, D. Song, T. Pu, J. Li, B. Huang, W. Wang, C. Zhao, L. Xie and L. Chen, *Chem. Eng. J.*, 2018, **336**, 679–689.

219 H. Zhang, H. Xie, D. Wang, Y. Xu, M. Yang, Z. Ai, Y. Shao, D. Shi, Y. Wu and X. Hao, *J. Colloid Interface Sci.*, 2025, **680**, 572–580.

220 G. Liu, C. Kang, J. Fang, L. Fu, H. Zhou and Q. Liu, *J. Power Sources*, 2019, **431**, 48–54.

221 G. Wang, L. Zhang and J. Zhang, *Chem. Soc. Rev.*, 2012, **41**, 797–828.

222 A. Sarkar, A. K. Satpati, P. Rao and S. Kumar, *J. Power Sources*, 2015, **284**, 264–271.

223 S. Donne, A. Hollenkamp and B. Jones, *J. Power Sources*, 2010, **195**, 367–373.

224 P. Geng, S. Zheng, H. Tang, R. Zhu, L. Zhang, S. Cao, H. Xue and H. Pang, *Adv. Energy Mater.*, 2018, **8**, 1703259.

225 L. Xu, M. Jia, Y. Li, X. Jin and F. Zhang, *Sci. Rep.*, 2017, **7**, 12857.

226 Y. Liu, D. He, H. Wu, J. Duan and Y. Zhang, *Electrochim. Acta*, 2015, **164**, 154–162.

227 D. Shanbhag, K. Bindu, A. Aarathy, M. Ramesh, M. Sreejesh and H. Nagaraja, *Mater. Today Energy*, 2017, **4**, 66–74.

228 Z.-D. Huang, B. Zhang, S.-W. Oh, Q.-B. Zheng, X.-Y. Lin, N. Yousefi and J.-K. Kim, *J. Mater. Chem.*, 2012, **22**, 3591–3599.

229 B. Zhu, S. Tang, S. Vongehr, H. Xie and X. Meng, *ACS Appl. Mater. Interfaces*, 2016, **8**, 4762–4770.

230 R. Tholkappiyan, A. N. Naveen, K. Vishista and F. Hamed, *J. Taibah Univ. Sci.*, 2018, **12**, 669–677.

231 Y. Xi, G. Wei, J. Li, X. Liu, M. Pang, Y. Yang, Y. Ji, V. Y. Izotov, Q. Guo and W. Han, *Electrochim. Acta*, 2017, **233**, 26–35.

232 R. Tholkappiyan, A. N. Naveen and K. Vishista, *AIP Conf. Proc.*, AIP Publishing LLC, 2015, vol. 1665, p. 140011.

233 D. Mondal, M. Kundu, B. K. Paul, D. Bhattacharya, S. Sarkar, S. Sau, D. Senapati, T. K. Mandal and S. Das, *ACS Appl. Nano Mater.*, 2024, **7**, 4913–4926.

234 H. Kennaz, A. Harat, O. Guellati, D. Momodu, F. Barzegar, J. Dangbegnon, N. Manyala and M. Guerioune, *J. Solid State Electrochem.*, 2018, **22**, 835–847.

235 Q. Xia, M. Xu, H. Xia and J. Xie, *ChemNanoMat*, 2016, **2**, 588–600.

236 Y. Zeng, M. Yu, Y. Meng, P. Fang, X. Lu and Y. Tong, *Adv. Energy Mater.*, 2016, **6**, 1601053.

237 X. L. Liu, H. M. Fan, J. B. Yi, Y. Yang, E. S. G. Choo, J. M. Xue and J. Ding, *J. Mater. Chem.*, 2012, **22**, 8235–8244.

238 H.-B. Xia, J. Yi, P.-S. Foo and B. Liu, *Chem. Mater.*, 2007, **19**, 4087–4091.

239 M. Yu, Z. Wang, Y. Han, Y. Tong, X. Lu and S. Yang, *J. Mater. Chem. A*, 2016, **4**, 4634–4658.

240 X. Chen, K. Chen, H. Wang and D. Xue, *Mater. Focus*, 2015, **4**, 78–80.

241 S. Shivakumara, T. R. Penki and N. Munichandraiah, *Mater. Lett.*, 2014, **131**, 100–103.

242 F. Azimov, J. Kim, S. M. Choi and H. M. Jung, *Nanomaterials*, 2021, **11**, 1557.

243 K. Zhang, Z. Cen, F. Yang and K. Xu, *Prog. Nat. Sci.: Mater. Int.*, 2021, **31**, 19–24.

244 J. Singh, S. Anand, S. Khan, M. T. S. Chani, T. Kamal, S. B. Khan, M. W. Ahmad and A. Choudhury, *Solid State Sci.*, 2026, **176**, 108276.

245 S. Cheng, Y. Zhang, Y. Liu, Z. Sun, P. Cui, J. Zhang, X. Hua, Q. Su, J. Fu and E. Xie, *Chem. Eng. J.*, 2021, **406**, 126875.

246 S. Abbas, T. H. Bokhari, M. Abbas, Z. Abbas, A. Khalid, S. Javed, A. Zafar, N. Ahmad, S. Karim and A. Javed, *Electrochim. Acta*, 2025, 145761.

247 R. Taniki and I. Honma, *ECS Trans.*, 2017, **75**, 25.

248 X. T. Gao, X. D. Zhu, S. R. Le, D. J. Yan, C. Y. Qu, Y. J. Feng, K. N. Sun and Y. T. Liu, *ChemElectroChem*, 2016, **3**, 1727.

249 G. Wee, H. Z. Soh, Y. L. Cheah, S. G. Mhaisalkar and M. Srinivasan, *J. Mater. Chem.*, 2010, **20**, 6720–6725.

250 Y. Ningyi, L. Jinhua and L. Chenglu, *Appl. Surf. Sci.*, 2002, **191**, 176–180.

251 G. Wee, H. Z. Soh, Y. L. Cheah, S. G. Mhaisalkar and M. Srinivasan, *J. Mater. Chem.*, 2010, **20**, 6720–6725.

252 T. Wang, H. C. Chen, F. Yu, X. Zhao and H. Wang, *Energy Storage Mater.*, 2019, **16**, 545–573.

253 G. Yang and S.-J. Park, *J. Alloys Compd.*, 2018, **741**, 360–367.

254 H. Shen, X. Kong, P. Zhang, X. Song, H. Wang and Y. Zhang, *J. Alloys Compd.*, 2021, **853**, 157357.

255 S. Beke, *Thin Solid Films*, 2011, **519**, 1761–1771.

256 J. S. Daubert, N. P. Lewis, H. N. Gotsch, J. Z. Mundy, D. N. Monroe, E. C. Dickey, M. D. Losego and G. N. Parsons, *Chem. Mater.*, 2015, **27**, 6524–6534.

257 Q. Qu, Y. Zhu, X. Gao and Y. Wu, *Adv. Energy Mater.*, 2012, **2**, 950–955.

258 D. D. Mohite, S. S. Chavan, S. Dubal and P. Karandikar, *AIP Adv.*, 2023, **13**, 120703.

259 K. Liang, X. Tang and W. Hu, *J. Mater. Chem.*, 2012, **22**, 11062–11067.

260 J. Zhu, L. Cao, Y. Wu, Y. Gong, Z. Liu, H. E. Hoster, Y. Zhang, S. Zhang, S. Yang and Q. Yan, *Nano Lett.*, 2013, **13**, 5408–5413.

261 E. Uchaker, Y. Zheng, S. Li, S. Candelaria, S. Hu and G. Cao, *J. Mater. Chem. A*, 2014, **2**, 18208–18214.

262 C. W. W. Chun and C.-H. Chung, *ChemSusChem*, 2015, **8**, 2399–2406.

263 J. Zheng, Y. Zhang, T. Hu, T. Lv and C. Meng, *Cryst. Growth Des.*, 2018, **18**, 5365–5376.

264 M.-H. Bai, T.-Y. Liu, F. Luan, Y. Li and X.-X. Liu, *J. Mater. Chem. A*, 2014, **2**, 10882–10888.

265 P. Asen and S. Shahrokhian, *Int. J. Hydrogen Energy*, 2017, **42**, 21073–21085.

266 W. Bi, Y. Wu, C. Liu, J. Wang, Y. Du, G. Gao, G. Wu and G. Cao, *ACS Appl. Energy Mater.*, 2018, **2**, 668–677.

267 H. Rahman and D. Kaur, *ACS Appl. Nano Mater.*, 2026, **9**, 3395–3407.

268 M. Karuppaiah, J. K. Lee and G. Ravi, *ACS Appl. Electron. Mater.*, 2024, **6**, 1504–1513.

269 B. Üstün, H. Aydın, S. N. Koç and Ü. Kurtan, *DRM*, 2023, **136**, 110048.

270 J. Riaz, J. Cao, Y. Zhang, A. Bibi and X. Zhou, *Nanoscale Adv.*, 2024, **6**, 5145–5157.

271 N. S. Lopa, M. K. Akbari, D. Wu, F. Verpoort and S. Zhuiykov, *Energy Fuels*, 2023, **37**, 3142–3151.

272 A. Ali, F. Rehman, S. Ahmed, G. Dastgeer, S. Oh, I. Hussain, J. Park, W. Jiang, T. L. Tamang and S. J. Oh, *J. Energy Storage*, 2025, **116**, 116033.

273 T. Zahra, B. Alotaibi, A. W. Alrowaily, H. A. Alyousef, A. G. Al-Sehemi and S. Aman, *J. Mater. Sci.: Mater. Electron.*, 2024, **35**, 1086.

274 S. Q. Zheng, S. S. Lim, C. Y. Foo, C. Y. Haw, W. S. Chiu, C. H. Chia and P. S. Khiew, *J. Energy Storage*, 2023, **63**, 106980.

275 K. Chinnaiah, K. Kannan, R. Krishnamoorthi, N. Palko and K. Gurushankar, *J. Phys. Chem. Solids*, 2024, **184**, 111730.

276 S. Muduli, S. K. Pati, T. K. Pani and S. K. Martha, *J. Energy Storage*, 2023, **66**, 107339.

277 M. Shariq, A. BaQais, T. M. Althagafi, O. Madkhali, A. A. Alholaisi, S. Hussain and Y. Javed, *Eur. Phys. J. Plus*, 2023, **138**, 389.

278 X. Yang, Y. Cui, Y. Qi, L. Fu, A. Rezayan, C. C. Xu, J. Wang, D. Sui and Y. Zhang, *J. Alloys Compd.*, 2023, **958**, 170513.

279 S. Kalia, D. Choudhary, M. Shrivastav, R. Bala, R. K. Singh, M. S. Khan and R. Dhiman, *Electrochim. Acta*, 2024, **491**, 144337.

280 A. F. Alem, A. K. Worku, D. W. Ayele, T. A. Wubieneh, A. Abebaw Teshager, B. T. Admasu, M. A. Teshager, A. A. Asege, M. D. Ambaw and M. A. Zeleke, *Heliyon*, 2023, **9**, e13286.

281 C. R. Babu, A. Avani, T. Xavier, M. Tomy, S. Shaji and E. Anila, *J. Energy Storage*, 2024, **80**, 110382.

282 M. Ashan, B. Alotaibi, A. W. Alrowaily, H. A. Alyousef, N. Al-Harbi, A. Dahshan, K. Ahmad and A. Henaish, *J. Alloys Compd.*, 2024, **994**, 174760.

283 Y. Zhang, P. Ding, W. Wu, H. Kimura, Y. Shen, D. Wu, X. Xie, C. Hou, X. Sun and X. Yang, *Appl. Surf. Sci.*, 2023, **609**, 155188.

284 P. Lu, M. Manikandan, P. Yang, Y. He, F. Yang, S. Dang, Y. Shi, W. Lou, R. Liu and S. Wu, *J. Mater. Sci.: Mater. Electron.*, 2023, **34**, 826.

285 M. Rafeeq, S. Ahmad, A. Sami, K. Z. Khan, Z. Haidar, F. Ahmed, G. Yasmeen, S. Ahmed and A. A. A. Bahajjaj, *Electrochim. Acta*, 2025, 145963.

286 S. S. Pujari, R. G. Bobade, R. C. Ambare and B. J. Lokh, *ES Energy Environ.*, 2024, **27**, 1324.

287 S. A. Kadam, Y.-R. Ma, Y.-R. Chen, Y. H. Navale, A. S. Salunkhe, V. B. Patil, S. D. Ralegankar and P. D. More, *J. Electron. Mater.*, 2023, **52**, 500–513.

288 G. Mummoorthi, S. Arjunan, M. Selvaraj, S. L. Rokhum, N. Mani, S. Periyasamy and R. Rajendran, *Surf. Interfaces*, 2023, **41**, 103166.

289 S. Rudra, S. Das, P. K. Maji, A. K. Nayak, Y. Negishi, M. Pradhan and U. Nandi, *ACS Appl. Nano Mater.*, 2023, **6**, 1648–1659.

290 R. Rohith, A. T. Prasannakumar, V. Manju, R. R. Mohan and S. J. Varma, *Chem. Eng. J.*, 2023, **467**, 143499.

291 S. A. Mane, D. Ulisso, A. A. Kashale, S. D. Dhas, A. V. Moholkar and A. V. Ghule, *J. Mater. Sci.: Mater. Electron.*, 2023, **34**, 719.

292 M. Bulla, V. Kumar, R. Devi, S. Kumar, S. Sindhu, R. Dahiya, A. Jatrana, A. K. Mishra and R. B. Singh, *J. Inorg. Organomet. Polym. Mater.*, 2025, 1–15.

293 Y. Kumar, S. Chopra, A. Gupta, Y. Kumar, S. Uke and S. Mardikar, *Mater. Sci. Energy Technol.*, 2020, **3**, 566–574.

294 P. Elumalai, J. Charles and L. J. Kennedy, *Ionics*, 2024, **30**, 7397–7420.

295 M. G. Joysi, S. Senthil, J. S. Jennifer, S. Muthupandi, W. Galeb, D. AnnieCanisius, M. J. R. Ruban, D. Varghese and M. V. A. Raj, *Results Chem.*, 2024, **10**, 101682.

296 M. Abdullah, P. John, K. Jabbour, M. I. Ahmad, S. Khan, M. S. Waheed, M. D. Albaqami, M. Sheikh, M. F. Ehsan and M. N. Ashiq, *J. Energy Storage*, 2024, **78**, 110034.

297 A. Bagde, D. Malavekar, A. Lokhande, S. Khot and C. Lokhande, *J. Alloys Compd.*, 2024, **980**, 173591.

298 B. Fugare, G. Chavan and B. Lokhande, *J. Mater. Sci.: Mater. Electron.*, 2024, **35**, 1460.

299 B. K. Manna, P. Panda, R. Mishra and S. Barman, *Energy Fuels*, 2023, **37**, 5613–5622.

300 R. Rani, M. Sharma, B. Mohan, A. Kumar, R. Chandra and V. K. Malik, *Energy Technol.*, 2024, **12**, 2301511.

301 H. Rashid Khan and A. Latif Ahmad, *J. Ind. Eng. Chem.*, 2025, **141**, 46–66.

302 A. Alharbi, *RSC Adv.*, 2025, **15**, 34551–34582.

303 J. Bhattacharjee and S. Roy, *J. Photochem. Photobiol.*, 2025, **25**, 100257.

304 S. Luanwuthi, P. Iamprasertkun, T. Akkharaamnuay, C. Kunyawut, A. Phukhrongthung and C. Puchongkawarin, *ACS Sustainable Chem. Eng.*, 2024, **12**, 14446–14458.

305 N. Singh, V. Singh, N. Bisht, P. Negi, A. Dhyani, R. K. Sharma and B. S. Tewari, *J. Energy Storage*, 2025, **121**, 116498.

306 N. Parvin, D. Merum, M. Kang, S. W. Joo, J. H. Jung and T. K. Mandal, *J. Mater. Chem. A*, 2025, **13**, 24320–24386.

307 H. Hegazy, S. S. Sana, T. Ramachandran, Y. A. Kumar, D. K. Kulurumotlakatla, H. S. Abd-Rabboh and S. C. Kim, *J. Energy Storage*, 2023, **74**, 109405.

308 Y. A. Kumar, G. R. Reddy, T. Ramachandran, D. K. Kulurumotlakatla, H. S. Abd-Rabboh, A. A. A. Hafez, S. S. Rao and S. W. Joo, *J. Energy Storage*, 2024, **80**, 110303.

309 K. V. C. Mouli, R. M. N. Kalla, T. Ramachandran, Y. A. Kumar, M. Moniruzzaman and J. Lee, *Int. J. Hydrogen Energy*, 2024, **90**, 1–24.